X-ray emission
from star-forming galaxies

Stefano Mineo

SIGILL: UNIVERSITAT: LUDOVIC: MAXIM:

München 2011

X-ray emission from star-forming galaxies

Stefano Mineo

Dissertation
an der Fakultät für Physik
der Ludwig–Maximilians–Universität
München

vorgelegt von
Stefano Mineo
aus Ragusa, Italien

München, den 22. 07. 2011

Erstgutachter: Prof. Dr. Rashid Sunyaev
Zweitgutachter: Prof. Dr. Viatcheslav Mukhanov
Tag der mündlichen Prüfung: 01. 09. 2011

Contents

List of Figures

List of Tables

Summary

In this dissertation we study the properties of high-mass X-ray binaries (HMXBs) and hot inter-stellar medium in star-forming galaxies and their relation with the star formation rate (SFR), based on the data from *Chandra*, Spitzer, GALEX and 2MASS public archives. We constructed a large sample of galaxies for which we collected homogeneous sets of multiwavelength measurements in X-ray, ultraviolet (UV), far-infrared (FIR) and near-infrared (NIR) bands. The sample includes 45 star-forming galaxies in total, divided in two sub-samples: the *primary sample*, consisting of 29 nearby galaxies, having distance < 40 Mpc, so that *Chandra* can resolve their X-ray point-like source population; the *high-SFR sample*, including 16 more distant galaxies that allowed us to extend the dynamical range of SFRs by $\sim$ two orders of magnitude.

In this sample we detected 1057 compact X-ray sources, of which ~ 300 are expected to be background active galactic nuclei (AGN). The majority of remaining ~ 700 sources are young systems associated with star-formation in the host galaxy. Based on their high X-ray luminosities and analogy with the X-ray populations in the Milky Way and few other very nearby galaxies, we conclude that they are high-mass X-ray binaries, powered by accretion of matter from a massive donor star onto a compact object - a black hole or a neutron star. Such a large number of sources allowed us to perform the most detailed study of the population of HMXBs and its dependence on various properties of the host galaxy, as well as to obtain a very accurate calibration of the X-ray luminosity-SFR relation.

The study of the population of HMXBs is based on their X-ray luminosity functions (XLF). To this end, we took a special care to minimize the contamination by LMXBs, background AGN and to control the incompleteness of the *Chandra* source lists. The shape of the HMXB luminosity function is similar in different galaxies with the power law indexes having $rms = 0.25$ with respect to the average value of ≈ 1.6. The XLF normalizations, on the contrary, show significantly larger dispersion with the $rms = 0.34$ dex around the $A \propto$ SFR law. Combining the data of all galaxies, which include ~ 700 X-ray sources, we produced the average XLF of high-mass X-ray binaries in nearby star-forming galaxies. Its statistical accuracy exceeds by far that achieved in any of the previous studies of the HMXB luminosity function. The HMXB XLF has a single power law shape in a broad luminosity range of $\log L_{\rm X} \sim 35 - 40$ and shows a moderately significant evidence for the high luminosity break or cut-off at $\log L_{\rm X} \approx 40$. We did not find any statistically significant features at the Eddington luminosity limits of neutron stars or a $10\, M_{\odot}$ black hole.

With the knowledge of the relation between the number of high-mass X-ray binaries

and star formation rate of the host galaxy, we estimated that the fraction of compact objects that went through an X-ray active phase at least once in their lifetime, powered by accretion of matter from a massive donor star in a binary system is $f_X \sim 0.2$. This constrains the mass distribution of the secondary in massive binaries. For an independent mass distribution of the secondary, the power law index must be flatter than 0.3. In particular, an independent mass distribution of a Kroupa or Salpeter type is strongly excluded. Assuming that the masses of components in a binary are not independent, our results are consistent with the flat mass ratio distribution. For comparison, we obtained a similar estimate for the fraction of compact objects that become X-ray sources powered by accretion from a low-mass donor star in an LMXB. Based on the scaling-laws by Gilfanov (2004), the fraction of compact objects, X-ray active in LMXBs, is small, $f_X \sim 10^{-6}$, demonstrating that LMXBs are extremely rare objects. This result is in line with the conclusions of the binary population studies.

The collective luminosity of high-mass X-ray binaries is a good tracer of the recent star formation activity in the host galaxy:

$$L^{\mathrm{XRB}}_{0.5-8\,\mathrm{keV}}(\mathrm{erg\,s^{-1}}) = 2.5 \times 10^{39}\,\mathrm{SFR}\,(M_\odot\,\mathrm{yr}^{-1}) \tag{1}$$

The *rms* of points around this relation is 0.4 dex. The observed dispersion is unlikely to be caused by any of the obvious contaminating factors such as CXB or LMXB sources and is likely to have a physical origin.

In addition to the emission from XRB population, the X-ray emission from star-forming galaxies includes a hot diffuse gas component with a mean characteristic temperature of $\sim 2 - 3 \times 10^6\,K$. We show that its X-ray luminosity correlates with the star formation rate of the host galaxy. Finally we demonstrate that the total X-ray luminosity of a galaxy scales with the star formation rate:

$$L^{\mathrm{tot}}_{0.5-8\,\mathrm{keV}}(\mathrm{erg\,s^{-1}}) = 4.5 \times 10^{39}\,\mathrm{SFR}\,(M_\odot\,\mathrm{yr}^{-1}) \tag{2}$$

with a dispersion $\sigma = 0.32$ dex. We obtained consistent scale factors for nearby galaxies from the resolved sample and galaxies from the high-SFR sample. Among the latter (eight out of 16) are *Chandra Deep Field* North galaxies, located at the red-shifts of $z \approx 0.2 - 1.3$. This proves that the total X-ray luminosity of a galaxy is a powerful tool to measure the star formation rate in distant galaxies.

Zusammenfassung

In dieser Dissertation präsentiere ich eine Untersuchung der Eigenschaften von (i) Röntgendoppelsternsystemen mit massereichen Sekundärsternen (engl.: high-mass X-ray binaries; HMXBs) und (ii) des heißen interstellaren Mediums (ISM) in Sternentstehungsgalaxien, sowie eine Studie über die Beziehung dieser Eigenschaften zur Sternentstehungsrate (engl.: star formation rate; SFR) der jeweiligen Galaxie. Dabei machte ich Gebrauch sowohl von Daten der Weltraumteleskope *Chandra*, Spitzer und GALEX als auch von den öffentlichen Archiven des Two Micron All Sky Survey (2MASS) und erstellte eine umfangreiche Stichprobe von Galaxien für die ich homogene Datensätze von Beobachtungen in den Wellenlängenbereichen Röntgen, Ultraviolett (UV), fernes Infrarot (FIR) und nahes Infrarot (NIR) zusammengetragen habe. Diese Stichprobe enthält insgesamt 45 Sternentstehungsgalaxien und wurde in zwei Untergruppen eingeteilt: die *primäre Stichprobe*, welche 29 nahe Galaxien mit Entfernungen < 40 Mpc enthält deren Röntgenquellenpopulation von *Chandra* aufgelöst werden kann, und die *high-SFR Stichprobe*, die 16 Galaxien in größerer Entfernung umfasst und es damit ermöglichte den dynamischen Bereich der SFR um circa zwei Größenklassen zu erweitern.

In der Gesamtstichprobe wurden ungefähr 1000 kompakte Röntgenquellen detektiert, von denen ~ 300 aktive Galaxienkerne (engl.: active galactic nuclei; AGN) im Hintergrund sein dürften. Bei der Mehrzahl der restlichen ~ 700 Quellen handelt es sich um junge Systeme die mit Sternentstehung in ihrer Muttergalaxie assoziiert sind. Auf Grundlage der großen Röntgenleuchtkraft dieser Quellen und ihrer Ähnlichkeit zur Population der Röntgenquellen in der Milchstraße und einigen anderen, nahen Galaxien schlussfolgerte ich, dass es sich bei diesen Systemen um HMXBs handelt, deren Energieausstoß durch Akkretion von Materie eines massereichen Begleitsterns auf ein kompaktes Objekt (Schwarzes Loch oder Neutronenstern) angetrieben wird. Die große Anzahl dieser Quellen erlaubte es mir, die bis dato ausführlichste Untersuchung der HMXB-Population und ihrer Abhängigkeit von diversen Eigenschaften der Muttergalaxie durchzuführen, sowie eine sehr präzise Kalibration der Beziehung zwischen Röntgenleuchtkraft und SFR zu gewinnen.

Meine Untersuchung der Population der HMXBs beruhte auf der Verteilung ihrer Leuchtkräfte im Röntgenbereich. Zu diesem Zweck galt meine besondere Sorgfalt einer Minimierung der Kontamination dieser Stichprobe mit Röntgendoppelsternsystemen mit massearmen Sekundärsternen (engl.: low-mass X-ray binaries; LMXBs) und Hintergrund-AGN, sowie der genauen Kenntnis der Unvollständigkeit der *Chandra*-Objektlisten. Die Profile der HMXB-Leuchtkraftfunktion für unterschiedliche Galaxien sind ähnlich und fol-

gen einem Potenzgesetz mit einem durchschnittlichen Exponenten von ~ 1.6 bei einer Standardabweichung von 0.25. Im Gegensatz dazu zeigen die Normierungen der Röntgenleuchtkraft-funktion (engl.: X-ray luminosity function; XLF) eine wesentlich größere Streuung (Standardabweichung von 0.34) um die Relation $A \propto \mathrm{SFR}$ herum. Durch die Kombination der Daten von allen Galaxien (insgesamt ~ 700 Röntgenquellen) konnte ich eine durchschnittliche XLF für HMXBs in nahen Sternentstehungsgalaxien erstellen, deren statistische Genauigkeit die bisheriger Studien bei weitem übertrifft. Die HMXB-XLF folgt einem einzigen Potenzgesetz über einen großen Helligkeitsbereich ($\log L_x \sim 35 - 40$) und zeigt einen mäßig signifikanten Abbruch bei $\log L_x \sim 40$, aber keine statistisch signifikanten Merkmale bei den Eddington-Leuchtkräften von Neutronensternen oder einem Schwarzen Loch mit 10 Sonnenmassen.

Mit dem Wissen um die Beziehung zwischen der Anzahl der HMXBs und der SFR der Muttergalaxie konnte ich den Anteil der kompakten Objekte, welche in ihrer Existenz mindestens einmal eine Phase der Röntgenaktivität zeigen (verursacht durch Akkretion von Materie eines massereichen Begleitsterns in einem Doppelsternsystem) zu $f_x \sim 0.2$ abschätzen. Dadurch wird die Massenverteilung der Begleitsterne in massereichen Doppelsternsystemen dahingehend eingeschränkt, dass eine unabhängige Verteilung einen Exponenten < 0.3 verlangt. Speziell wird damit eine unabhängige Massenverteilung nach Kroupa oder Salpeter deutlich ausgeschlossen. Unter der Annahme, dass die Massen der Komponenten eines Doppelsternsystems nicht voneinander unabhängig sind, sind meine Ergebnisse in Übereinstimmung mit einer flachen Verteilung der Massenverhältnisse. Ein ähnliches Ergebnis erhielt ich für den Anteil von kompakten Objekten welche durch Akkretion der Materie eines massearmen Begleitstern zu Röntgenquellen werden (LMXBs). Auf Grundlage der Skalierungsgesetze von Gilfanov (2004) wird erwartet, dass nur ein sehr geringer Anteil von kompakten Objekten in aktiven LMXBs zu finden ist ($f_x \sim 10^{-6}$). Dies zeigt, dass LMXBs extrem seltene Objekte sind und ist in Übereinstimmung mit Ergebnissen aus Doppelstern-Populationsstudien.

Die Gesamthelligkeit aller HMXBs in einer Galaxie ist ein gutes Maß für die kürzliche Sternentstehungsaktivität in dieser Galaxie:

$$L^{\mathrm{XRB}}_{0.5-8\,\mathrm{keV}}(\mathrm{erg\,s^{-1}}) = 2.5 \times 10^{39}\,\mathrm{SFR}\,(M_\odot\,\mathrm{yr}^{-1}) \tag{3}$$

Die Standardabweichung für diese Beziehung ist 0.4 dex. Die beobachtete Streuung wird dabei voraussichtlich nicht durch eine (nahe liegende) Kontamination mit LMXBs oder dem kosmischen Röntgenhintergrund hervorgerufen, sondern hat wahrscheinlich eine physikalische Ursache.

Zusätzlich zu der Strahlung der Röntgendoppelsterne beinhaltet die Röntgenemission von Sternentstehungsgalaxien eine weitere Komponente, hervorgerufen durch heißes, diffuses Gas mit einer charakteristischen Durchschnittstemperatur von $\sim 2 - 3 \times 10^6$ K. In dieser Arbeit zeige ich, dass die Röntgenleuchtkraft dieses Gases mit der SFR der Muttergalaxie korreliert ist. Schließlich demonstriere ich in meiner Dissertation dass die gesamten Röntgenleuchtkraft einer Galaxie mit ihrer SFR skaliert:

$$L^{\mathrm{tot}}_{0.5-8\,\mathrm{keV}}(\mathrm{erg\,s^{-1}}) = 4.5 \times 10^{39}\,\mathrm{SFR}\,(M_\odot\,\mathrm{yr}^{-1}) \tag{4}$$

mit einer Streuung von $\sigma = 0.32$ dex. Die Skalierungsfaktoren für die Primärstichprobe und die high-SFR Stichprobe sind dabei miteinander konsistent. In der high-SFR Stichprobe befinden sich acht (von insgesamt 16) Galaxien aus dem *Chandra Deep Field* North mit Rotverschiebungen von $z \sim 0.2 - 1.3$. Dies zeigt, dass es sich bei der gesamten Röntgenleuchtkraft einer Galaxie um ein leistungsfähiges Werkzeug zur Messung der SFR in entfernten Galaxien handelt.

Chapter 1

Introduction

1.1 X-ray emission from star-forming galaxies

The first studies of the X-ray emission from nearby galaxies were performed with *Einstein Observatory* (Giacconi et al., 1979) and ROSAT (Truemper, 1982). They revealed that the X-ray output from galaxies is mainly due to individual luminous X-ray sources and extended, often complex and relatively bright, diffuse emission. The subsequent X-ray mission, *ASCA* (Tanaka, Inoue, & Holt, 1994), contributed to broaden our knowledge of the X-ray properties of galaxies thanks to a better spectral resolution and a wider spectral band, despite its angular resolution was worse than the previous two missions. The study of the X-ray emission from normal galaxies took a revolutionary leap forward only with the advent of XMM-*Newton* and *Chandra* (Weisskopf et al., 2000). With highly improved spectral and angular resolutions (on the order of sub-arcsecond for *Chandra*) they allowed to separate the individual X-ray sources from the diffuse emission of the hot interstellar medium (ISM), both spatially and spectrally, so that their properties are nowadays being investigated in great details.

In the following sections we unfold the general properties of the main components contributing to the X-ray emission from star-forming galaxies. In particular, in Section 1.1.1 we overview the diverse classes of X-ray discrete sources, in Section 1.1.2 we introduce the X-ray emission from the hot ISM and its morphological properties.

1.1.1 Resolved X-ray sources

X-ray binaries

The X-ray output of a normal gas-poor galaxy is dominated by the collective emission of its X-ray binary (XRB) population (see review by Fabbiano, 2006). X-ray binaries consist of a compact object, either a neutron star (NS) or a black hole (BH) accreting material from a companion normal star. Based on the mass of the of the latter, they are conventionally divided into low-mass, $M_{\rm opt} \lesssim 1 M_{\odot}$, and high-mass, $M_{\rm opt} \gtrsim 5 M_{\odot}$, X-ray binaries (LMXBs and HMXBs respectively).

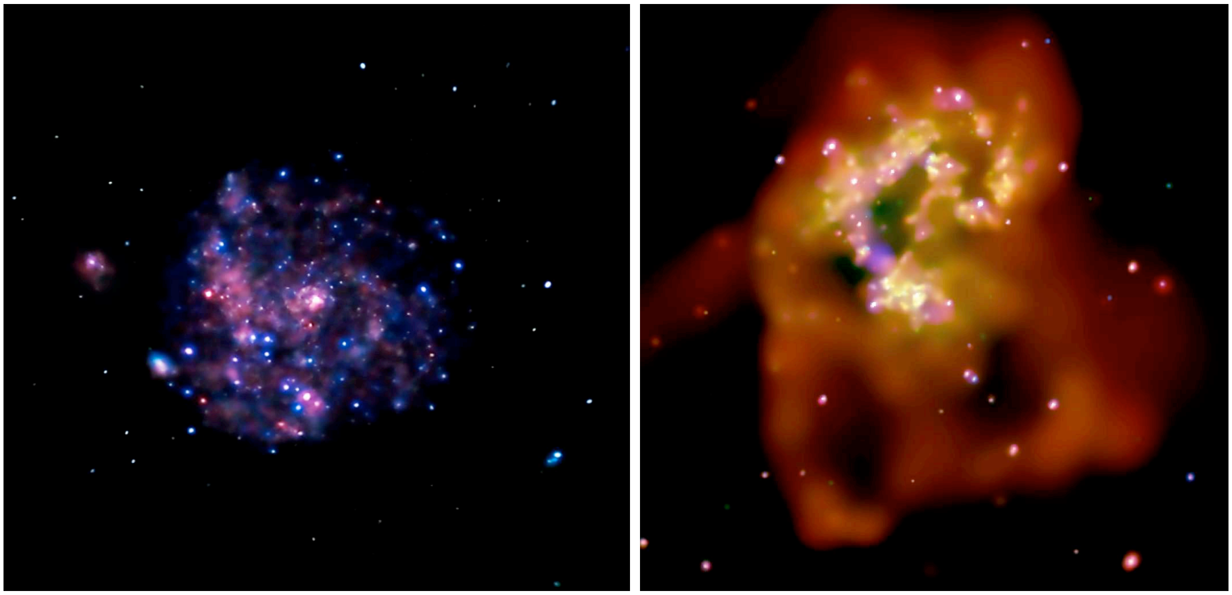

Figure 1.1: An example of X-ray emission from star-forming galaxies. (*Left:*) *Chandra* X-ray images of the spiral galaxy Messier 101. The point-like sources include binary star systems containing black holes and neutron stars, and the supernova remnant. Other sources of X-rays include hot gas in the arms of the galaxy. (*Right:*) *Chandra* X-ray images of a pair of interacting galaxies known as The Antennae. It reveals hot gas outflows into the inter-galactic medium (IGM). Also shown are huge clouds of hot gas and bright point like sources due to the X-ray binary population. The image is color coded so that low, medium and high energy X-rays appear as red, green and blue, respectively. (Credits: NASA/CXC/JHU/K.Kuntz et al. for M101; NASA/CXC/SAO/G. Fabbiano et al. for The Antennae.)

Low-mass X-ray binaries, constituted of companion stars belonging to the old stellar population, are concentrated in the bulges of late-type galaxies and also distributed along the discs. The typical LMXBs lifetime of $\sim 10^9 - 10^{10}$ yr is comparable to the lifetime of the host galaxy. Their population is therefore defined by the cumulative effect of the star formation episodes experienced by the host galaxy, i.e it is proportional to its total stellar mass (Gilfanov, 2004). The accretion of matter in LMXBs occurs if the companion star fills its Roche. The characteristic shape of the X-ray luminosity function (XLF) of LMXBs is parametrized with a model consisting of broken power law with two breaks (Gilfanov, 2004; Kim & Fabbiano, 2004): a first break at $\log(L_{\rm X}) \sim 37.5$ and a second at $\log(L_{\rm X}) \sim 38.5$, near the Eddington limit of an accreting neutron star. The faint end of the XLF appears to be flat (being the slope ~ 1) and becomes steeper at higher luminosities. The XLFs of LMXBs have normalization proportional to the stellar mass of the galaxy and show a characteristic cut-off luminosity at $\log(L_{\rm X}) \sim 39$.

High-mass X-ray binaries are spread over the galactic plane. They are short-lived, as their X-ray active phase is limited by the lifetime of a massive donor star, $\sim 10^7 - 10^8$ yr, which is comparable to the duration of a star formation event (Grimm, Gilfanov, & Sunyaev, 2003). Although the accretion of matter in HMXBs might also occur through Roche lobe overflows, two main cases are also observed: *i*) in case the donor is a main sequence Be star, typically having equatorial winds, the compact object accretes periodically, when it crosses this disc along its wide eccentric orbit around the companion star; that normally causes X-ray outbursts. *ii*) When the donor star is a supergiant experiencing winds, the compact object directly accretes the stellar wind through Bondi-Hoyle accretion. By studying HMXBs in nearby star-forming galaxies, in the Milky Way and in Small Magellanic Cloud (SMC), Grimm, Gilfanov, & Sunyaev (2003) determined the shape of XLF of HMXBs. It consists in a pure power law with slope ~ 1.6, cut off at $\log(L_{\rm X}) \sim 40.5$ and normalization proportional to the SFR of the galaxy.

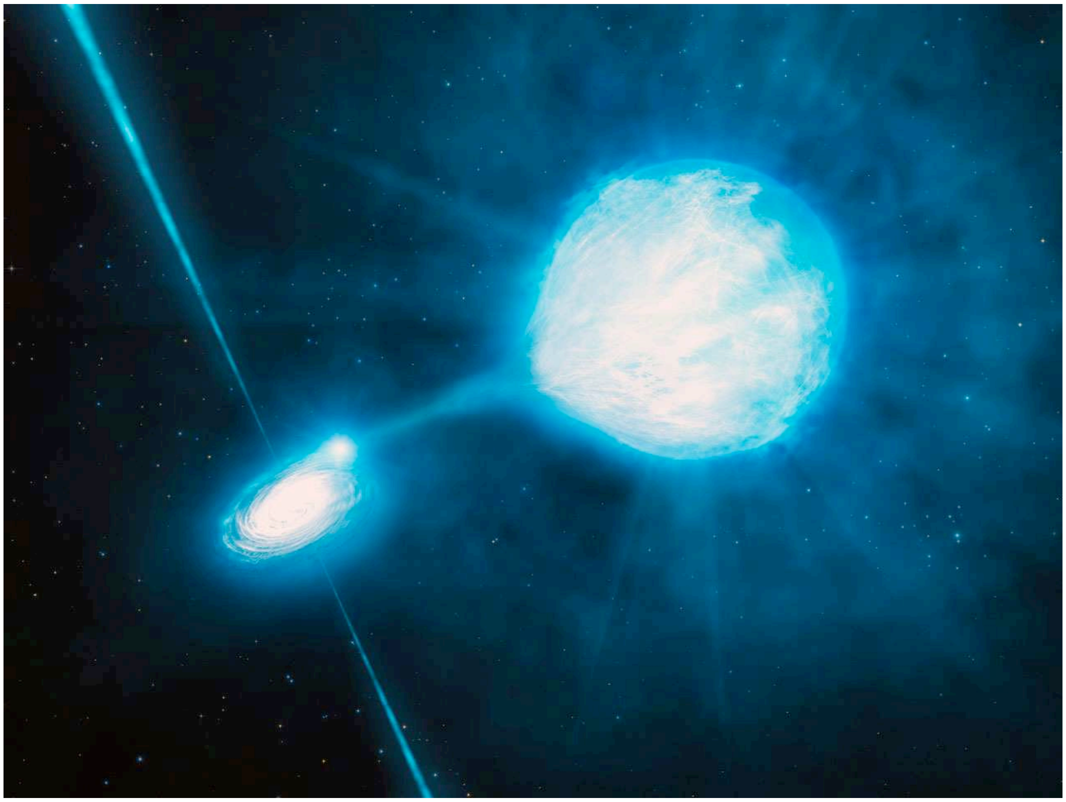

Figure 1.2: Artist's impression of a black hole accreting from a companion star through Roche lobe overflows. Credit: ESO/L.Calçada.

Ultra-luminous X-ray sources

Ultra-luminous X-ray sources (ULXs) are off-nuclear X-ray point sources in nearby galaxies, with a luminosity that exceeds the Eddington limit for a 10 $M_\odot$ black hole $L_{\rm X} \geq 2\times10^{39}$ erg s^{-1}; the maximum observed luminosity for such sources is $\sim 10^{42}$ erg s^{-1} in the galaxy ESO243-49 (Colbert & Mushotzky, 1999; Farrell et al., 2009). These sources have been known to exist since the 1980s (the first ULX was discovered with *Einstein Observatory*). Despite intensive observations and considerable efforts in their interpretation, their nature has remained unknown. They may provide indication for the existence of either intermediate-mass ($10^2 - 10^5 M_\odot$) black holes (IMBHs), if they radiate isotropically at sub-Eddington levels as observed in stellar-mass black holes, or for non-explored accretion regimes. There is a number of theoretical models for ULXs which do not require an IMBH. These include beaming effects on the emission from stellar-mass black holes (King et al., 2001) or truly super-Eddington emission (Begelman, 2002). Based on observations of large samples of both late- and early-type galaxies, several authors have suggested a statistical association of ULXs with young stellar populations (e.g. Swartz et al., 2004). Results by Grimm, Gilfanov, & Sunyaev (2003) and the present work, support this evidence, suggesting that the ULX population might be an extension of the high-mass X-ray binary population that contribute to the luminosity function up to 10^{40} erg s^{-1} but not above.

1.1.2 Unresolved X-ray emission

Some classes of X-ray sources are characterized by relatively low luminosity, with typical X-ray luminosities of $10^{31} - 10^{35}$ erg s^{-1}. With the current X-ray observatories these sources can not be resolved in most external galaxies, thus they are blend in together, contributing to the unresolved X-ray emission. The classes of faint compact X-ray sources include: active binaries (ABs), whose X-ray emission is caused by chromospheric-coronal activity of rapidly rotating stars; cataclysmic variables (CVs), consisting of white dwarfs (WDs) accreting material from a companion star; quiescent low-mass X-ray binaries (qLMXBs) characterized by a sporadic accretion of a neutron star; supernova remnants (SNRs), millisecond pulsars, young stellar objects (YSOs) and young stars. also contribute to the X-ray emission from galaxies at low luminosities.

The unresolved X-ray emission include also a truly diffuse component of hot gas. Its global characteristics in external galaxies are generally consistent with those found in our Galaxy. It has mean temperature of $\sim 2 - 3 \times 10^6\,K$ and its X-ray luminosity was suggested to be proportional to star formation rate of the host galaxy. The morphology of the hot inter-stellar medium is rather complex. Diffuse hot gas is not detected in the interarm regions of spiral galaxies. There is often evidence of significant galactic hot gaseous outflows, i.e. superwinds escaping the galaxy, believed to be driven by the collective energy input from supernovae and winds from young massive stars (e.g. Chevalier & Clegg, 1985; Strickland et al., 2000, 2004; Grimes et al., 2005; Bogdán & Gilfanov, 2008).

1.2 Star-forming galaxies - a multiwavelength view

Spiral and irregular galaxies, i.e. late-type, are gas-rich galaxies with high star formation activity - star-forming galaxies. The disc of spiral galaxies is characterized by the spiral arms, which are regions of enhanced density of gas, dust and stars. These regions are the areas where star formation occurs. The star-forming galaxies with an exceptionally high rate of star formation are named starbursts.

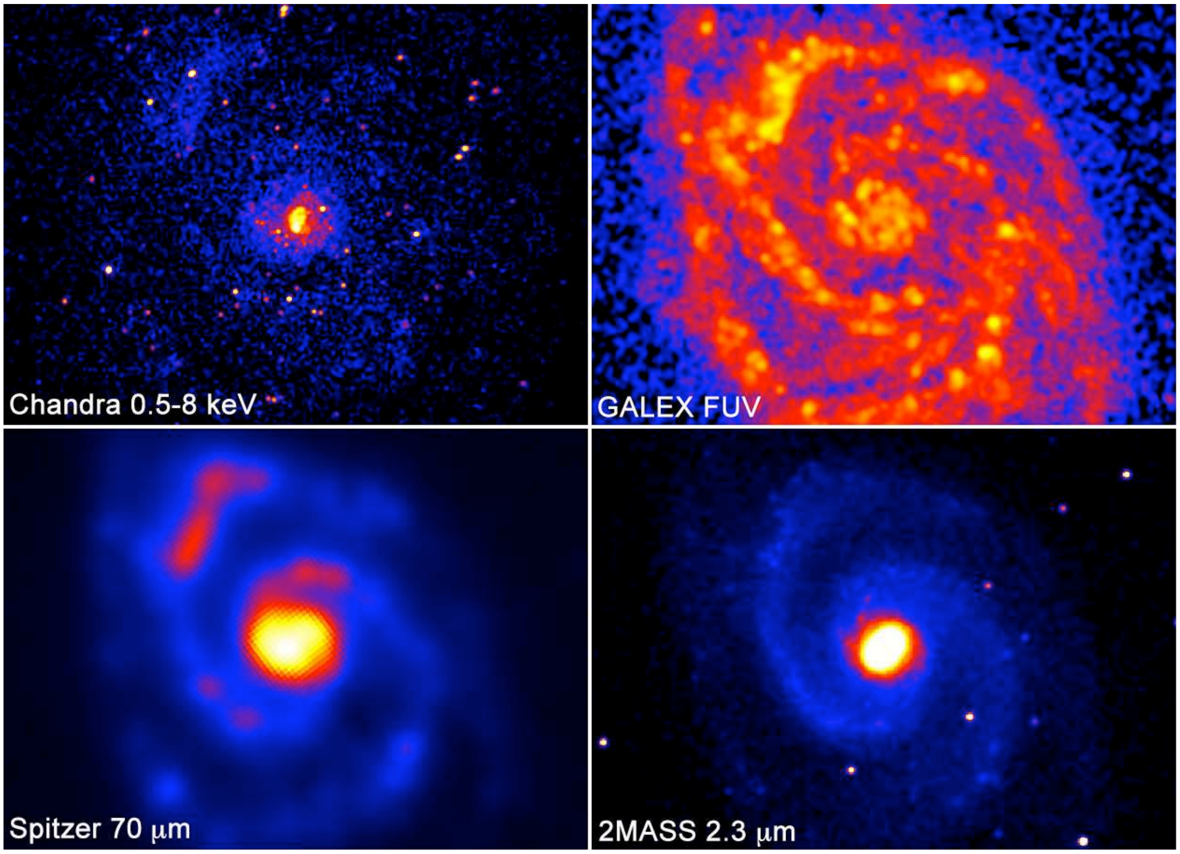

Figure 1.3: A multiwavelength view of the star-forming galaxy M51 A, as it is seen by raw data from four observatories. *Upper left: Chandra* full band (0.5–8 keV) image. It shows the emission from both X-ray binary population and diffuse hot gas. *Upper right:* Far-UV image from GALEX, tracing the emission from the atmospheres of young massive stars and therefore the star formation activity. *Lower left:* 70 μm image from Spitzer, shows the emission from dust. The latter reprocesses the UV emission from young stars into infrared and therefore traces the sites of star formation. *Lower right:* K_S-band image from 2MASS, tracing the old stars in galaxies. They are mostly concentrated in the bulge of the galaxy.

In star-forming galaxies, most of the light from massive young stars is absorbed by dust and re-radiated in infrared (IR) wavelengths. Photons by massive stars are typically emitted in ultraviolet (UV). As a consequence, the overall morphology of the UV and IR emission in star-forming galaxies appears similar. This is evident by looking at the upper right-hand and lower left-hand panels in Fig.1.3, showing GALEX FUV and Spitzer 70μm images respectively. Despite the difference in resolution between the latter two images, there is a clear correspondence between the areas of enhanced far-infrared (FIR) and UV emissions along one of the spiral arms (in the north-west direction of the galaxy). The same galactic area shows an enhancement of the diffuse X-ray emission, visible in the upper left-hand image. Moreover, the morphology of the warm dust component at $70\mu m$ strongly resembles the morphology of the H_α emission, confirming that the infrared emission traces the star formation complexes.

Stars of old age populations are the principal contributors to the near infrared (NIR) luminosity at $2.3\mu m$, the so-called K_S-band. Therefore the NIR emission traces the distribution of old stellar populations along the galaxy. NIR luminosity can be used as a measure of the stellar mass. The lower right-hand panel in Fig.1.3 shows a K_S-band image of M51 A. The NIR light is concentrated in the bulge and its density appear to gradually decrease along the galactic plane.

1.3 X-ray, infrared and ultraviolet observatories

Figure 1.4: An artist's illustration of the Chandra spacecraft. Credit:NASA/CXC/NGST

The work presented in this dissertation has a multiwavelength nature and is based on a homogeneous set of X-ray, infrared and ultraviolet observations from *Chandra*, Spitzer, GALEX and 2MASS archives. The X-ray analysis HMXB populations and diffuse hot gas was performed based on *Chandra* data. Images from Spitzer and GALEX were used for estimating the SFR in the sample galaxies. The stellar mass of the latter was measured based on images from 2MASS archive. In this section we overview the characteristics of the latter three missions and the near-infrared survey, giving particular emphasis to the *Chandra X-ray Observatory*.

1.3.1 Chandra X-ray observatory

The most consistent part of the present study is based on data from *Chandra X-ray Observatory*[1] (Weisskopf et al., 2000) (Fig. 1.4). The satellite was launched on July 23^{rd}, 1999 from the Kennedy Space Center in Cape Canaveral, onboard the Space Shuttle Columbia and it is the most advanced X-ray telescope built to date. It is the third of NASA's four Great Observatories. The strongly eccentric orbit of the spacecraft (~ 140000 km apogee and 10000 km perigee), allows the *Chandra* to actively observe during $\sim 70\%$ of the time, when it is out of the Earths radiation belts. Therefore it is possible to run continuous observations for over 100 ks.

Chandra is designed to observe photons in the $0.3 - 10$ keV energy range and is extensively employed for high-resolution imaging, due to its extraordinary sub-arcsecond angular resolution. The High Resolution Mirror Assembly (HRMA) consists of four pairs of nested Wolter type-I mirrors, the focal length is 10.07 m. The effective area of the HRMA is 800 cm^2 at 0.25 keV, 400 cm^2 at 5 keV, and 100 cm^2 at 8 keV.

Besides the HRMA, four science instruments are onboard the spacecraft. Two instruments placed in the focal plane, designed for imaging: the Advanced CCD Imaging Spectrometer (ACIS) (Garmire et al., 2003) and the High Resolution Camera (HRC) (Murray et al., 2000). Two instruments intercepted the X-rays, dedicated to high-resolution spectroscopy: the High Energy Transmission Grating (HETG) (Canizares et al., 2000) and the Low Energy Transmission Grating (LETG) (Predehl et al., 2000)

The ACIS detector consists of ten CCDs, eight of them are front-illuminated (FI) and two of them are back-illuminated (BI), with a pixel size of ACIS CCDs is 0.492 arcseconds. The BI CCDs have larger effective area at low energies, but their background is higher if compared with the FI CCDs. On the other hand, the FI CCDs have a better spectral resolution but in early stages of the satellite they were damaged by the radiation belts of the Earth, yielding a varying spectral resolution along the CCDs. The set of ACIS CCDs can be arranged in two patterns: either a 2×2 array is used with a 17×17 arcminutes field of view (ACIS-I), or a 1×6 array with 8.5×51 arcminutes field of view (ACIS-S). The HRC is constituted by two microchannel plate detectors having better timing properties than ACIS detectors. HRC has a large 30×30 arcminutes field of view, but essentially no energy resolution and the pixel size is smaller than on ACIS detectors.

The HETG and LETG onboard Chandra were designed to be used with ACIS-S detectors and both have excellent spectral resolution. These grating instruments are primarily use of for the study of bright X-ray point sources. The HETG is constituted by two different gratings, the High Energy Grating and the Medium Energy Grating. They cover the

---

[1] *Chandra* is named in honor of the Indian-American Nobel laureate physicist Subrahmanyan Chandrasekhar, one the most prominent astrophysicists of the 20th century.

spectral range of $1.2 - 15\,\mathring{A}$ and $2.5 - 31\,\mathring{A}$, respectively. The LETG operates in the range of $1.2175\,\mathring{A}$.

1.3.2 Spitzer Space Telescope

The Spitzer Space Telescope (SST) is an infrared space observatory, the fourth mission of the NASA Great Observatories program, launched in 2003. It follows a heliocentric orbit and has a primary mirror of 85 cm in diameter. Three science instruments are onboard the satellite, performing imaging and photometry from 3 to $180\,\mu m$, spectroscopy from 5 to $40\,\mu m$, and spectrophotometry from 5 to $100\,\mu m$. *i*) IRAC (Infrared Array Camera) operates in four wavelengths: $3.6\,\mu m$, $4.5\,\mu m$, $5.8\,\mu m$ and $8\,\mu m$. Each module uses a detector of 256×256. *ii*) IRS (Infrared Spectrograph) is an infrared spectrometer that operates in low resolution at the wavelengths of $5.3 - 14\,\mu m$ and $14 - 40\,\mu m$, and in high resolution at $10 - 19.5\,\mu m$ and $19 - 37\,\mu m$. Each module uses a detector of 128×128 pixel. *iii*) MIPS (Multiband Imaging Photometer for Spitzer), includes three detector arrays in the far infrared: 128×128 pixels at $24\,\mu m$, 32×32 pixels at $70\,\mu m$ and 2×20 pixels at $160\,\mu m$. We only used $24\,\mu m$ and $70\,\mu m$ data from MIPS, to measure the SFR of the sample galaxies.

1.3.3 The Galaxy Evolution Explorer

The Galaxy Evolution Explorer (GALEX) is an orbiting space telescope observing galaxies in two ultraviolet bands: far-ultraviolet (FUV) $1350 - 1750\,\mathring{A}$ and near-ultraviolet (NUV) $1750 - 2800\,\mathring{A}$, with 4.0 and 5.6 arcsecond resolution (FWHM) respectively. It is a NASA Small Explorer Mission launched on April 28^{th} 2003. GALEX has wide-field (1.2 degree) UV telescope with a mirror of 50 cm in diameter and selectable imaging window or grism. It is performing the first ultraviolet imaging and spectroscopic all-sky survey to measure the UV properties of local and distant galaxies. The main science goals include the calibration of the UV-global star formation rate in galaxies to map the history of star formation in the universe over the red shift range zero to two.

1.3.4 The Two Micron Sky Survey

The Two Micron All-Sky Survey (2MASS) is a near-infrared all-sky survey carried out between 1997 and 2001 at two ground-based telescopes, one located in the northern hemisphere and one in and southern hemispheres (Mt. Hopkins Arizona and Cerro Tololo/CTIO Chile, respectively). The whole sky was covered using a photometric system of three infrared wavebands around 2 micrometres: J ($1.25\,\mu m$), H ($1.65\,\mu m$), and $K_{\rm s}$ ($2.17\,\mu m$). 2MASS provides a rich statistical database for large samples of galaxies ($> 1,000,000$) that can also be used as statistical basis to search for rare astrophysical objects (e.g. either cool and very red or heavily obscured at optical wavelengths). The goals of this survey included a view of the entire length of the Milky Way nearly free of the obscuring effects of interstellar dust.

1.4 Outline of the thesis

In Chapter 2 we present the selection criteria and the resulting sample of galaxies. Chapter 3 includes several technical sections. We describe the X-ray data analysis methods. We study the spatial distribution of compact sources in our sample galaxies in order to minimize the contamination by LMXBs, cosmic X-ray background (CXB) and active galactic nuclei (AGN). We unfold the analysis of far-infrared, near-infrared and ultraviolet data and present the star formation rate estimators that we use in the present work. In Chapter 4, we study luminosity distributions of HMXBs in individual galaxies and their average XLF and investigate the behavior of the collective luminosity of HMXBs and its dependence on the star-formation rate. In Chapter 5, we discuss the astrophysical implications of the obtained results on HMXB population and various aspects of their application. In Chapter 6, we discuss the luminosity of the hot interstellar medium and its dependence on the star-formation rate and derive the star formation rate calibration for the total X-ray luminosity. In Chapter 7 we summarize our findings.

Chapter 2

The sample

2.1 Primary sample of resolved galaxies

We started to build the sample of star-forming galaxies from the entire "Normal Galaxies" section of the *Chandra* Data Archive. It includes over 300 galaxies of all morphological types. We based our selection on the following four criteria.

i) Hubble type: we selected only late-type galaxies, i.e. those having numerical index of stage along the Hubble sequence $T > 0$. According to this definition, $S0$ galaxies were excluded since the origin of their far-infrared and ultraviolet emission is not associated with recent star formation.

ii) Specific SFR: as star-forming galaxies contain also LMXBs, unrelated to the recent star-formation activity, the contribution of the latter will contaminate the $L_{\rm X}$−SFR relation. Although separation of the high- and low- mass XRBs in external galaxies is virtually impossible, the LMXBs contribution can be controlled in a statistical way. To this end we use the fact that their population is proportional to the stellar mass $M_\star$ of the host galaxy (Gilfanov, 2004), whereas HMXBs scale with SFR (Grimm, Gilfanov, & Sunyaev, 2003), therefore the specific SFR (SFR/$M_\star$) can serve as a measure of their relative contributions to the X-ray luminosity of the galaxy. We estimated the stellar mass of the galaxies as it is described in Gilfanov (2004), using the $K_{\rm S}$-band ($2.16\,\mu$m) magnitudes from The Two Micron All Sky Survey (2MASS). For the purpose of the sample selection we used IRAS data to estimated SFRs. Based on the fluxes at $60\,\mu$m and $100\,\mu$m taken from IRAS catalogues, we first computed the $42.5 - 122.5\,\mu$m flux (FIR) following Helou, Soifer, & Rowan-Robinson (1985). Adopting a standard correction factor of 1.7 we converted the latter into a $8 - 1000\,\mu$m flux and computed SFR using the calibration of Bell (2003) (eq. 4). Taking into account the shapes of luminosity distributions for high- and low-mass X-ray binaries and typical point sources detection sensitivities of Chandra data, we estimated that a threshold of SFR/$M_\star > 1 \times 10^{-10}$ yr^{-1} would be a reasonable compromise, sufficient for our purpose.

iii) Number of compact sources: in order to perform the spatial analysis of the detected sources (see Sect. 3.3), we required that galaxies in our sample have 10 or more compact

Galaxy	D (Mpc)	Hubble type	i^a (deg)	SFR^b ($M_\odot$ yr^{-1})	$M_\star{}^c$ (10^{10} $M_\odot$)	SFR/$M_\star$ (10^{-10} yr^{-1})	$\log L_{\rm lim}{}^d$ (erg s^{-1})	$N_{\rm XRB}{}^e$	$\log L_{\rm XRB}{}^f$ (erg s^{-1})	$N_{\rm CXB}{}^g$	$\log L_{\rm CXB}{}^h$ (erg s^{-1})
NGC 0278	11.4	SAB(rs)b	0	4.1	7.2×10^{-2}	56.9	37.22	10	39.34	1.6	38.38
NGC 0520	27.8	Pec	69	11.6	4.7	2.4	38.18	11	40.40	2.3	39.39
NGC 1313	4.1	SB(s)d	38	0.44	0.1	4.2	36.82	8	39.69	2.4	37.92
NGC 1427A	15.9	IB(s)m	55	0.21	7.3×10^{-3}	28.7	37.72	6	39.72	1.0	38.59
NGC 1569	1.9	IB	64	7.8×10^{-2}	2.8×10^{-2}	2.8	35.71	10	37.93	0.78	36.52
NGC 1672	16.8	SB(s)b	37	12.0	4.6	2.6	37.74	25	40.38	7.1	39.45
NGC 2139	26.7	SAB(rs)cd	53	3.8	0.91	4.2	38.14	15	40.47	1.8	39.26
NGC 2403	3.1	SAB(s)cd	62	0.52	0.27	1.9	36.16	42	39.37	17.7	38.31
NGC 3034 (M82)	3.9	I0	66	10.5	2.4	4.3	36.86	54	39.86	6.5	38.37
NGC 3079	18.2	SB(s)c	88	6.0	4.0	1.5	37.98	12	39.69	0.61	38.55
NGC 3310	19.8	SAB(r)bc pec	25	7.1	0.98	7.2	37.84	23	40.78	2.1	39.03
NGC 3556	8.7	SB(s)cd	81	2.2	1.1	2.0	37.09	30	39.60	5.0	38.68
NGC 3631	24.3	SA(s)c	36	4.6	2.6	1.8	37.92	29	40.60	8.6	39.77
NGC 4038/39	13.8	-	-	5.4	3.1	1.7	36.92	83	40.23	12.4	39.15
NGC 4194	39.1	IBm pec	49	16.8	2.1	8.0	38.64	4	40.45	0.5	39.12
NGC 4214	2.5	IAB(s)m	37	0.17	3.3×10^{-2}	5.2	36.19	14	38.33	5.1	37.71
NGC 4490	7.8	SB(s)d pec	65	1.8	0.39	4.7	37.10	32	40.05	2.8	38.17
NGC 4625	8.2	SAB(rs)m pec	23	0.09	7.0×10^{-2}	1.3	37.01	4	37.98	0.57	37.67
NGC 4631	7.6	SB(s)d	85	4.0	1.4	2.9	37.09	21	39.65	6.8	38.77
NGC 5194 (M51A)	7.6	SA(s)bc pec	64	3.7	1.3	2.8	37.05	69	39.93	26.4	39.33
NGC 5253	4.1	Im pec	77	0.38	5.9×10^{-2}	6.5	36.07	17	38.52	5.0	37.82
NGC 5457 (M101)	6.7	SAB(rs)cd	0	1.5	0.99	1.5	36.36	96	39.47	38.2	39.05
NGC 5474	6.8	SA(s)cd pec	37	0.18	9.1×10^{-2}	2.0	37.04	10	38.90	2.5	38.27
NGC 5775	26.7	Sb(f)	84	5.3	6.3	0.85	38.01	25	40.53	2.5	39.33
NGC 7090	7.6	SBc	90	0.29	0.22	1.3	37.23	11	39.10	1.5	38.19
NGC 7541	34.9	SB(rs)bc pec	75	14.7	4.9	3.0	38.41	13	40.25	0.81	39.16
NGC 7793	4.0	SA(s)d	50	0.29	0.15	2.0	36.55	9	38.23	3.2	37.88
UGC 05720	24.9	Im pec	28	1.8	0.37	4.9	38.36	4	39.68	0.18	38.37
CARTWHEEL	122.8	S pec (Ring)	-	17.6	8.8	2.0	39.20	11	41.23	0.68	40.01

Table 2.1: Primary sample: galaxies resolved by *Chandra*.

---

[a] Inclination angles taken from Tully (1988).

[b] Star formation rate from *Spitzer* and GALEX data (see Sect. 3.7).

[c] Stellar mass from 2MASS data (see Sect. 3.6).

[d] Sensitivity limit in decimal logarithmic units, defined as the luminosity level corresponding to a value of the incompleteness function $K(L) = 0.6$.

[e] Number of XRBs with luminosity above the sensitivity limit, detected within the galactic region where the HMXBs dominate the compact X-ray source population (Sect. 3.3).

[f] Base-10 logarithm of the total X-ray luminosity of galaxies in the $0.5 - 8$ keV band, estimated by using eq. (4.8).

[g] Predicted number CXB sources within the selected region (see Sect. 3.3), with luminosity above the sensitivity limit.

[h] Predicted contribution of CXB sources to the total X-ray luminosity of galaxies.

sources within the isophotal diameter $D25$. In case multiple observations were available in the *Chandra* archive for a given galaxy, we combined them in order to improve the sensitivity limit, $L_{\rm lim}$. We used only those observations in which the galaxy is observed sufficiently close to the aim- point, with sufficiently long exposure-time ($t_{\rm exp} \geq 15$ ks).

iv) Distance: for the galaxies passed through the above criteria, a number of redshift independent distances, determined with different methods, were collected from NED[1]. Following the results of Jacoby et al. (1992), we chose the most accurate among them. For our primary sample we chose a distance threshold of 40 Mpc, in order to spatially resolve the X-ray compact sources with *Chandra*. This also allows us to identify and separate the central AGN from the rest of detected point sources.

v) Sensitivity The galaxy list produced in the result of this selection had sensitivities in the range of $\log(L_X) \sim 35.7 - 38.6$ with the median value of $\log(L_X) \sim 37.1$. As we perform an accurate incompleteness correction, no further filtering based on the point source detection sensitivity was performed.

For the purpose of binary population studies, this rigorously defined sample was complemented by two more galaxies. In order to improve statistics of the high luminosity end of the XLF we added the Cartwheel galaxy. It has the largest SFR value among our resolved galaxies and although is more distant (D$\sim$ 123 Mpc), the brightest sources, with $\log(L_X) \gtrsim 39$, do not suffer from significant sources confusion in Chandra data. To expand the low luminosity end we used the ASCA data of SMC observations (Yokogawa et al., 2003). The SMC data were used only for the XLF construction.

The so defined primary sample is presented in Table 2.1. It includes 29 galaxies, with SFR values ranging from ~ 0.1 to ~ 20 $M_\odot$ yr^{-1}.

2.2 High-SFR sample.

In order to explore the $L_{\rm X} - {\rm SFR}$ relation in the high SFR regime, we relaxed the distance constraint and constructed a secondary sample from the galaxies that passed the first and second criteria, and are characterized by high star-formation rates, $SFR \gtrsim 15$ $M_\odot$/yr. In total, we found 8 galaxies with SFR ranging from 15 to 290 $M_\odot$ yr^{-1} (all, natuirally, located outside $D > 40$ Mpc).

These galaxies were treated as spatially unresolved in our analysis (see Sect. 4.2.1 for details and caveats). Five of them are classified as ultra-luminous infrared galaxies (ULIRGs) and two as luminous infrared galaxies (LIRGs). The remaining object (NGC 4676 or The Mice), is a merging system. Although they were contained in the normal galaxies section of the Chandra archive, based on quantitative indications found in literature (Farrah et al., 2003; Nardini et al., 2009; Yuan, Kewley, & Sanders, 2010), we verified that the contribution of AGN to the bolometric luminosity in these galaxies is $< 30\%$, to ensure that the IR-based SFR measurement is not compromised by the latter. For the two LIRG galaxies (IRAS 13362+4831 and IRAS 00344-3349) we found only a qualitative indication of the AGN contribution.

---

[1] NASA/IPAC Extragalactic Database

Finally, we also included 8 normal galaxies from the Chandra Deep Field North (HDFN) (Brandt et al., 2001). Their selection is described in Gilfanov, Grimm, & Sunyaev (2004); their K-corrected X-ray and radio luminosities were taken from the same source. Thus, our high-SFR sample included 16 galaxies, listed in Table 2.2 and 2.3.

2.3 A remark regarding the roles of primary and secondary samples

It is important to realize the different roles and the difference in the way the two samples are treated. The main goal of this paper is to study population of high-mass X-ray binaries, their luminosity distribution and dependence of their number and collective luminosity on the star-formation rate and other properties of the host galaxy. This is achieved with the help of resolved galaxies of our primary sample. Their analysis is presently limited to the emission from compact sources, the contribution of various unresolved emission components is not considered. To properly resolve the populations of compact sources, we considered only galaxies located within the distance of $D < 40$ Mpc. This limited the volume and, correspondingly the range of SFRs probed by the primary sample. Indeed, the highest SFR in our resolved galaxies does not exceed $\sim 15-20\ M_{\odot}$/yr.

In order to probe the high-SFR regime, we complemented our primary sample with more distant galaxies. This allowed us to extend the dynamical range of SFRs by $\sim$ two orders of magnitude. On the other hand, due to larger distances to these galaxies, their compact source populations can not be studied at the same level of detail, because of insufficient point source detection sensitivity and source confusion, even in the most nearby of them. Therefore we treated them as unresolved (even though the angular extent of some of them was as large as $\sim 25-50$ arcsec) and only measured their total X-ray emission. Obviously, X-ray luminosities of these galaxies can not be directly compared with our primary sample, as they include the contribution of diffuse emission, which may be significant in star-burst galaxies. However these galaxies help to present the broader picture and to constrain the properties of bright HMXBs and ULXs in the high SFR regime and at intermediate redshifts, based on the behavior of their collective emission, using the ideas described in Gilfanov, Grimm, & Sunyaev (2004). The quantitative analysis of the full $L_{\mathrm{X}} - SFR$ relation for the two samples, including diffuse X-ray component, will be presented in the forthcoming publication.

Galaxy	D^a (Mpc)	Luminosity Class	SFR ($M_\odot$ yr^{-1})	M$_\star$ ($10^{10} M_\odot$)	SFR/$M_\star$ (10^{-10} yr^{-1})	$\log L_{\rm X}$ (erg s^{-1})	$\alpha_{\rm bol}{}^b$ (%)	Ref.^{c}
IRAS 17208-0014	183.0	ULIRG	289.9	10.3	28.1	41.40	< 0.4	(1)
IRAS 20551-4250	179.1	ULIRG	139.4	7.5	18.6	41.63	28^{+5}_{-4}	(1)
IRAS 23128-5919	184.2	ULIRG	139.6	7.0	19.9	41.88	$3.9^{+1.1}_{-0.8}$	(1)
IRAS 10565+2448	182.6	ULIRG	156.8	9.9	15.8	41.42	< 0.1	(2)
IRAS 13362+4831	120.9	LIRG	54.8	17.3	3.2	41.81	high	(3)
IRAS 09320+6134	164.3	ULIRG	137.1	13.1	10.5	41.39	16 ± 3	(1)
IRAS 00344-3349	84.0	LIRG	20.1	1.5	13.7	41.23	no	(3)
NGC 4676	98.2	-	15.8	6.6	2.4	40.92	-	-

Table 2.2: High-SFR sample: unresolved galaxies.

---

[a] distance from Sanders et al. (2003).

[b] AGN contribution to the bolometric luminosity (in per cent).

[c] References for AGN contribution to the bolometric luminosity:
(1) Nardini et al. (2009), (2)Farrah et al. (2003), (3)Yuan, Kewley, & Sanders (2010).

Galaxy	Redshift	$F_{0.5-8\mathrm{keV}}$ (10^{-15} erg s^{-1} cm^{-2})	$L_{0.5-8\mathrm{keV}}$ (10^{40} erg/s)	$F_{1.4\mathrm{GHz}}$ (μJy)	$L_{1.4\mathrm{GHz}}$ (10^{30} erg/s)	SFR ($M_\odot$ yr^{-1})
123634.5+621213	0.456	0.43	31.43	233.00	1.63	90.56
123634.5+621241	1.219	0.31	163.86	230.00	15.94	885.56
123649.7+621313	0.475	0.15	10.09	49.20	0.37	20.56
123651.1+621030	0.410	0.30	14.61	95.00	0.52	28.89
123653.4+621139	1.275	0.22	128.03	65.70	5.18	287.78
123708.3+621055	0.423	0.18	9.39	45.10	0.23	12.78
123716.3+621512	0.232	0.18	2.55	187.00	0.27	15.0
0084857.7+445608	0.622	1.46	177.76	320.00	4.50	250.0

Table 2.3: High-SFR sample: galaxies from the *Hubble Deep Field* North and Lynx Field. Note. See Grimm, Gilfanov, & Sunyaev (2003) for a complete description of the sample and assessment for the central AGN emission.

Chapter 3

Data analysis and SFR estimation

3.1 X-ray data preparation

We analyzed in total 64 *Chandra* observations, 63 ACIS-S and one ACIS-I, listed in Table 3.1. The data preparation was done following the standard CIAO[1] threads (CIAO version 3.4; CALDB version 3.4.1) and limiting the energy range to 0.5−8.0 keV. We performed the point source detection in each observation using CIAO `wavdetect`. The scale parameter was changed from the default value. We used the $\sqrt{2}$-series from 1.0 to 8.0 to have a wide enough range of source sizes to account for the variation in PSF from the inner to the outer parts of an observation. In order to avoid false detections, the value of the parameter `sighthresh` was kept rather low. We set it as the inverse of the total number of pixel in the image. The typical values being in the range $\sim 10^{-7} - 10^{-8}$. We used `maxiter` = 10, `iterstop` = 0.00001 and `bkgsigthresh` = 0.0001. We set the parameter `eenergy` = 0.8 (the encircled fraction of source energy used for source parameter estimation).

Readout streaks caused by a bright point source were seen in two cases: observation 378 (M82) and 315 (Antennae). To avoid that such a problem could affect source detection, we corrected the events using `acisreadcorr`.

Multiple observations were present for $\sim 30\%$ of the sample galaxies; they were combined in order to improve the sensitivity and, in case of large objects, to cover the galactic area. We first used CIAO `reproject_events` to reproject all the observations into the sky coordinates of the longest observation of a given galaxy. The images were then merged using `merge_all` script and the `wavdetect` task was applied again to the combined image. An exposure map weighted according to a specific model for the incident spectrum was computed for each observation. We assumed the energy distribution to be an absorbed powerlaw with $\Gamma = 2.0$, the column density being $n_H = 3 \times 10^{21}$ cm^{-2}. The same spectrum was assumed to convert counts into erg.

---

[1] http://cxc.harvard.edu/ciao3.4/index.html

3.2 Point source counts and luminosities

For X-ray photometry of compact sources we used the approach and scripts from Voss & Gilfanov (2007). The count rate for each detected point source was calculated inside a circular region centered on the source central coordinates given by `wavdetect` output. In order to determine the radius of the circle, for each observation we extracted the point spread function (PSF) using CIAO `mkpsf` task. In case of multiple observations the PSFs were combined using the values of the exposure maps as weights. We mapped the PSFs into the World Coordinate System (WCS) reference frame of the relative point source image using `reproject_image` task. The radius of the circle was determined individually for each source so that the encircled PSF energy was 85%. For the background region we used a circle with radius 3 times the radius of the source region. The corrected source counts and errors were then found by the following equations (Voss & Gilfanov, 2007):

$$S = \frac{C(b-d)d^{-1} - Q}{\alpha b d^{-1} - \beta} \tag{3.1}$$

$$\sigma_S^2 = \frac{\sigma_C^2 (b-d)^2 d^{-2} + \sigma_Q^2}{(\alpha b d^{-1} - \beta)^2} \tag{3.2}$$

where S is the number of net counts from the source, C is the number of counts inside the source region and Q is the number of counts in the background region, α is the integral of the PSF over the source region, β is the integral of the PSF over the source and background regions, b is the area of the source and background regions and d is the area of the source region. The latter two quantities were derived by integrating the exposure maps rather than computing the geometric areas.

The problem of point source crowding may compromise the total X-ray luminosity estimation of galaxies. We identified in each galaxy all the compact sources having background regions overlapping neighboring sources. For the galaxies affected by crowding problem, we performed a second iteration of the circular photometry procedure defining the radius of each source so that it included 90% of encircled PSF. These regions were then excluded from both the individual image and exposure map of one of the overlapping point sources in order to subtract the source counts and correct the source area respectively. We finally used the corrected image and exposure map to perform the photometry procedure defining the radius of the circle for each source so that the encircled PSF energy was 85% and obtained the corrected C, Q, b and d for applying eqs. 3.1 and 3.2.

The X-ray luminosities of X-ray binaries in galaxies from our primary sample were computed as a sum of luminosities of compact sources, corrected for the incompleteness and CXB contribution and transformed to a common luminosity limit, as described in Section 4.3.

The galaxies from the secondary high-SFR sample were treated as unresolved objects and their luminosity was measured as the background-subtracted luminosity inside the $D25$ ellipse. The counts-to-ergs conversion in this case was determined based on the modeling of their X-ray spectra. For most of the spectra the best-fit was obtained with a two component model: a thermal plasma plus a power-law corrected for the Galactic absorption. In two cases (IRAS 20551-4250 and IRAS 23128-5919) a good fit was obtained with a three-component model, according to Franceschini et al. (2003): a thermal component and a "leaky -absorber" continuum, including an absorbed plus a non-absorbed power law spectrum of the same photon index. To measure the X-ray luminosity of unresolved galaxies and the contribution of diffuse gas in resolved galaxies, we created source and background spectra and the associated ARF and RMF files using `specextract` script, which is suitable for extended sources. Spectra were then modeled using XSPEC v. 12.3.1x.

The luminosities of HDFN galaxy sample were measured in $0.5 - 8\,\mathrm{keV}$ band, using their count rates, best fit slopes from Brandt et al. (2001) and redshifts from Cohen et al. (2000).

Readout streaks caused by a bright point source were seen in two cases: observation 378 (M82) and 315 (Antennae). To avoid that such a problem could affect source detection, we corrected the events using `acisreadcorr`.

An exposure map weighted according to a specific model for the incident spectrum was computed for each observation. We assumed the energy distribution to be an absorbed powerlaw with $\Gamma = 2.0$, the column density being $n_H = 3 \times 10^{21}$ cm^{-2}. The same spectrum was assumed to convert counts into erg.

3.3 Spatial analysis

Whereas irregular galaxies host young stars, the stellar population of spirals is spread in a broad range of ages. The old populations of bulges are totally dominated by LMXBs, similar to the ones of elliptical galaxies. An active nucleus can be also present. The disk instead hosts X-ray binaries of different ages. As galaxies are mostly transparent to X-rays above 2 keV, background X-ray sources are also detected in each galactic area. Although reliable separation of different classes of sources in external galaxies based on their X-ray properties is virtually impossible, contributions of LMXBs and background AGN can be controlled and subtracted in the statistical manner. In order to identify regions of galaxies where the HMXBs dominate the compact X-ray source population, we analyzed the spatial distribution of the detected compact sources in resolved galaxies of the primary sample. An example of regions selected based on this method is shown in Fig. 3.2.

3.3.1 Contribution of the central AGN

The AGN contribution can be simply discriminated in resolved galaxies ($D < 40$ Mpc). Three nearby galaxies were found to have a type-2 active nucleus: NGC 1672, NGC 3079, M51A (Véron-Cetty & Véron, 2006). Whereas the central sources of M51A, NGC 3079 were identified and simply excluded from the analysis, no central X-ray source was detected in NGC 1672. In this galaxy Jenkins et al. (2011) found evidence for a low-luminosity active galactic nucleus (LLAGN), with $2 - 10$ keV luminosity of 4×10^{38} erg s^{-1}. The non-detection might be due to different `wavdetect` settings in the present work and in

Galaxy	Obs-ID	Galaxy	Obs-ID
NGC 0278	2055	NGC 4631	797
	2056	NGC 5194 (M51A)	3932
NGC 0520	2924		1622
NGC 1313	2950	NGC 5253	7153
NGC 1427A	3949		7154
NGC 1569	782		2032
NGC 1672	5932	NGC 5457 (M101)	934
NGC 2139	8196		4732
NGC 2403	4630		5309
	4628		5322
	4629		6114
	2014		4736
NGC 3034 (M82)	378		4731
	2933		5340
NGC 3079	2038		5300
NGC 3310	2939	NGC 5474	9546
NGC 3556	2025	NGC 5775	2940
NGC 3631	3951	NGC 7090	7252
NGC 4038/39	315		7060
	3040	NGC 7541	7070
	3041	NGC 7793	3954
	3042	IRAS 17208-0014	2035
	3043	IRAS 20551-4250	2036
	3044	IRAS 23128-5919	2037
	3718	IRAS 10565+2448	3952
NGC 4194	7071	IRAS 13362+4831	2044
NGC 4214	5197	IRAS 09320+6134	2033
	4743	IRAS 00344-3349	8175
	2030	NGC 4676	2043
NGC 4490	4726	CARTWHEEL	2019
	4725	UGC 05720	9519
	1579		
NGC 4625	9549		

Table 3.1: *Chandra* observations analyzed.

Jenkins et al. (2011), as we used a higher detection significance threshold. The detection of such a source is also difficult due to the fact that the source is surrounded by an X-ray-bright circumnuclear star-forming ring with point sources and hot gas. The X-ray source at the center of NGC 4039 was also excluded from the analysis. The nature of this source is indeed controversial. Brandl et al. (2009) ruled out the presence of an AGN at the center of NGC 4039, based on the lack of [Ne V] emission and the low [O iv]/[Ne ii] ratio. On the other hand, using *Chandra* data, Desroches & Ho (2009) found that the best-fitting X-ray spectrum of the central source in NGC 4039 is indicative of a very high state LMXB instead of a true AGN. They also pointed out that, although their spectral fits are insufficient to distinguish a LMXB from an AGN, the source is unlikely to be an HMXB due to the fact that it is located in a nuclear star cluster.

For galaxies of the high-SFR sample, the AGN contribution in the X-ray band was constrained directly from the *Chandra* images. Galaxies from the "unresolved" sample of Table 2.2 are in fact partly resolved by *Chandra*, the smallest one having angular size of $D25 \sim 24$ arcsec. This is enough to verify, that none of them has a dominating central point source. The upper limit of 30% on the AGN contribution to the IR luminosity (see Sect. 2) ensures that the IR based SFR determination is not compromised by the AGN. The HDFN and Lynx field galaxies were selected by Grimm, Gilfanov, & Sunyaev (2003) based on the identifications from Richards et al. (1998)

3.3.2 Contribution of LMXBs

Although only star-forming galaxies with $\mathrm{SFR}/M_\star \geq 1 \times 10^{-10}$ yr^{-1} have been selected, the contribution of LMXBs to the total X-ray luminosity can be further minimized. For galaxies having an inclination angle $i \lesssim 65$ deg the bulge region was located by inspecting the optical and near-infrared images and taking into account the information available in literature. The X-ray point sources detected in such regions were then excluded from the analysis. We excluded the same regions from the analysis of infrared and ultraviolet data (Sect. 3.6).

3.3.3 Contribution of CXB sources

In the central regions of galaxies the surface density of XRBs is sufficiently high that the contribution of background AGNs can be neglected. In the outer parts the surface density of compact sources becomes comparable to the average density of CXB sources and the latter may become and important source of contamination. In order to minimize this contamination we used the following procedure.

For each resolved galaxy we defined an elliptical region according to the isophotal diameter ($D25$), isophotal diameter ratio ($R25$) and the position angle of the major axis (PA), taken from the RC3 catalog (de Vaucouleurs et al., 1991). We computed the incompleteness function $K(L)$ of the part of the *Chandra* image within this region, following the method and code from Voss & Gilfanov (2006). We defined the completeness luminosity L_{comp} as the luminosity at which $K(L) = 0.8$ (i.e no more than 20% of point sources

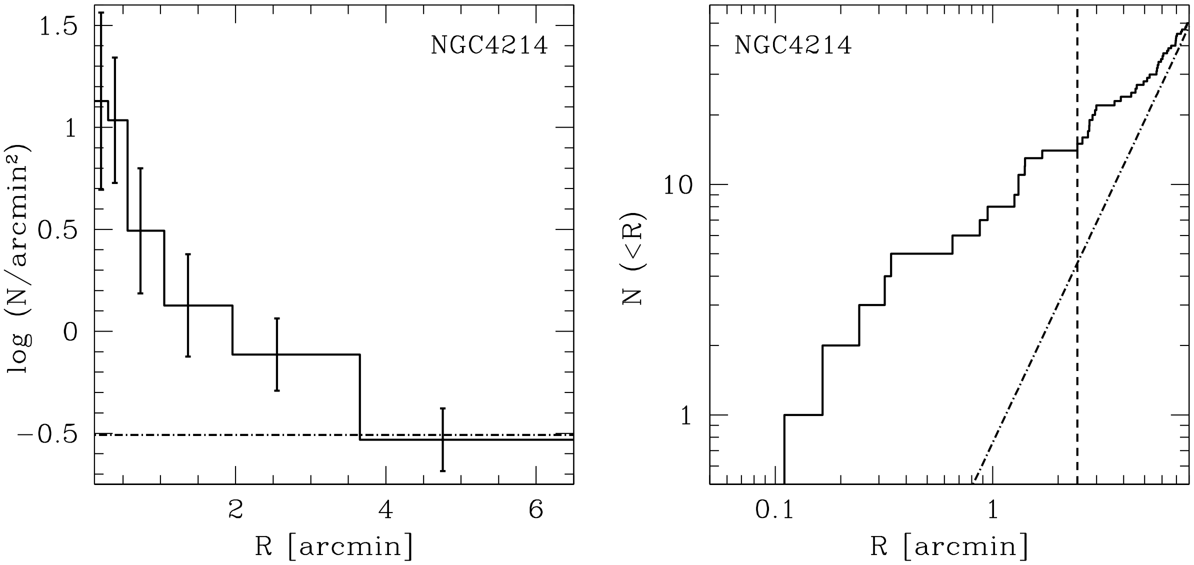

Figure 3.1: An example of the spatial analysis performed in resolved galaxies. *Left:* surface density of the detected point sources (solid histogram) plotted together with the predicted CXB level from Georgakakis et al. (2008) (dotted-dashed line). *Right:* cumulative radial profile of detected point sources (solid line) and the CXB growth curve (dotted-dashed line). The vertical dashed line indicates the radius where the cumulative number of CXB sources equals 1/3 of the total number of detected compact sources. It is the radius $R_{\rm X}$ of the elliptical region we choose to analyze.

are missing). For point sources detected with luminosity above the completeness limit, we constructed cumulative and differential radial profiles (see Fig. 3.1 for an example) accounting for the elliptical shape of the region. The latter were compared with the CXB level predicted above the same luminosity threshold. We used the full band $\log N - \log S$ of Georgakakis et al. (2008) and converted it to the $0.5-8\,\mathrm{keV}$ band used for the detection. We checked its consistency with the observed density of point sources using differential profiles (left panel in Fig.3.1). The radius $R_{\rm X}$ of the (elliptical) galactic region that will be used for the analysis was defined based on the cumulative profile as the radius within which the contribution of CXB sources equals 30% of the total number of detected compact sources. The so determined radii $R_{\rm X}$ approximately follow the relation:

$$R_{\rm X}(\mathrm{arcmin}) = R\left(\frac{N_{\rm CXB}}{N_{\rm tot}} \approx 30\%\right) = 1.2 \times \left(\frac{D25}{2}\right)^{0.6} \tag{3.3}$$

In four galaxies (NGC 1427A, NGC 4194, NGC 4625 and UGC 05720) we detected a rather small number (4−6) of point sources that did not allow us to perform spatial analysis. For these galaxies we analyzed the $D25$ ellipse regions, as their CXB contamination was found to be in the $5\% - 16\%$ range.

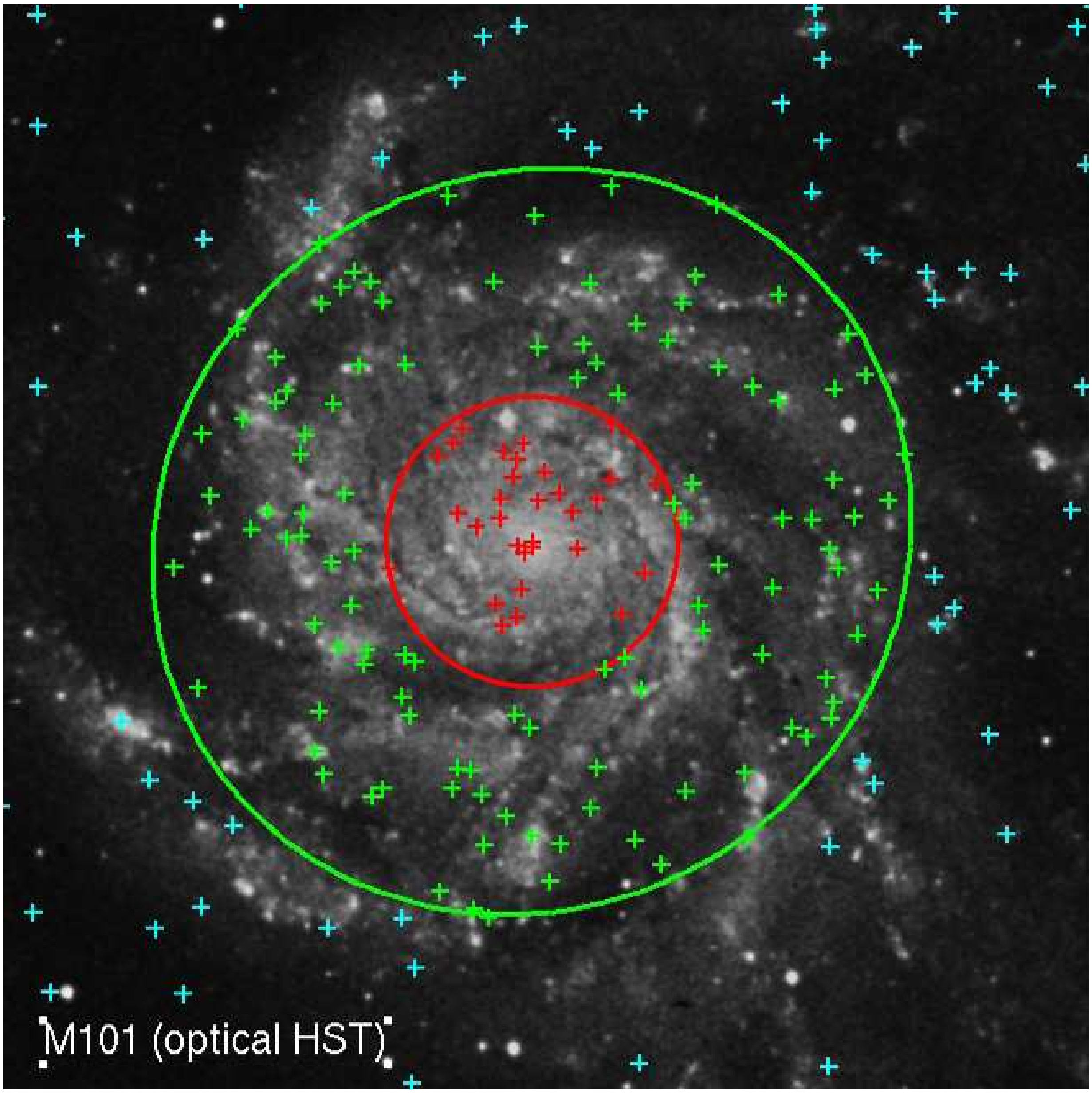

Figure 3.2: Optical (HST) image of M101. The crosses indicate the position of detected X-ray point sources. Those in red were detected within the bulge of the galaxy, the latter region is also marked in red color, and were excluded from the analysis because dominated by LMXB population. The size of the bulge region for this particular galaxy was chosen based on results from Gilfanov (2004). The green crosses indicates the point sources that have been detected in the inner galactic region dominated by HMXB population, that is marked in green as well and it was selected as described in Sect.3.3. The outer region is dominated by CXB sources and the relative detected X-ray point sources are marked in cyan.

3.4 Isolating the hot ISM

The X-ray diffuse emission can be polluted by a number of contaminating factors, such as compact X-ray sources, their "spill-over" counts and unresolved high-mass X-ray binaries. The contribution of al these quantities needs to be subtracted. An additional source of contamination must be accurately accounted for in studying the unresolved X-ray emission - the instrumental and cosmic X-ray background. In the following sections we describe how we isolate the hot inter-stellar medium in the sample galaxies, to study its X-ray properties.

3.4.1 Compact X-ray sources and their residual counts

In order to determine the optimal size of the source region that would minimize the contamination from compact X-ray sources and their spillover counts to the diffuse X-ray emission, we performed a study on three spiral galaxies chosen as representative of our sample: a face-on galaxy with strong diffuse emission (NGC 3310), a face-on galaxy with weak diffuse emission (NGC 3631) and a edge-on galaxy (NGC 5775). We used the wavelet-based source detection algorithm `wavdetect` (see Sect.3.1 for the parameter settings) to search for point like sources in the soft ($0.5 - 2.0$ keV), hard ($2.0 - 8.0$ keV) and total ($0.5 - 8.0$ keV) energy bands. We defined the point source regions as circles centered on the source central coordinates by `wavdetect` output. The radius of each circle was determined individually for each source based on the point spread function (PSF) in the given detector area, following the method described in Mineo, Gilfanov, & Sunyaev (2011), so that the encircled PSF energy was 90%. Hereafter, we refer to this radius as $R_{90\%\,\mathrm{PSF}}$.

Based on the source lists obtained in each energy band, we created a set of source regions having radii ranging from $0.5 \cdot R_{90\%\,\mathrm{PSF}}$ to $2.5 \cdot R_{90\%\,\mathrm{PSF}}$ with a step of 0.1. A correspondent set of diffuse emission images was created for each galaxy, in each energy band, adopting the following method. Using the CIAO task `dmfilth`, we removed the source regions from the image and filled in the holes left by the source removal with pixel values interpolated from surrounding background regions (POISSON method). In order to avoid biases in the interpolation, we ensured that the chosen background annuli did not contain neighboring point source counts. For each background region listed in the input file, we subtracted all the overlapping neighboring point source regions and merged them into a single source removal region.

Using the CIAO task `dmextract` we estimated the count rates in all the sets of images of diffuse emission in each energy band, for each galaxy, within the $D25$ ellipse. In Fig .3.3 we plot the count rates against the values of the radius of removed point source region. The count rate appears to follow a roughly similar trend in the three galaxies analyzed: *i*) a drop off for point source radii $\leq R_{90\%\,\mathrm{PSF}}$, *ii*) a shallower trend for $R_{90\%\,\mathrm{PSF}} < R < 1.5 \cdot R_{90\%\,\mathrm{PSF}}$ and *iii*) a plateau for $R > 1.5 \cdot R_{90\%\,\mathrm{PSF}}$ (which is a monotonic decrease in case of NGC 3310 because of its diffuse emission opulence). Assuming that the monotonic decrease observed NGC 3310 would flatten for point source sizes larger than $2.5 \cdot R_{90\%\,\mathrm{PSF}}$, an increase of the radius of removed point sources above $1.5 \cdot R_{90\%\,\mathrm{PSF}}$ would affect the diffuse emission count rate by less than 10%. Hence the removal of point source regions with $R = 1.5 \cdot R_{90\%\,\mathrm{PSF}}$

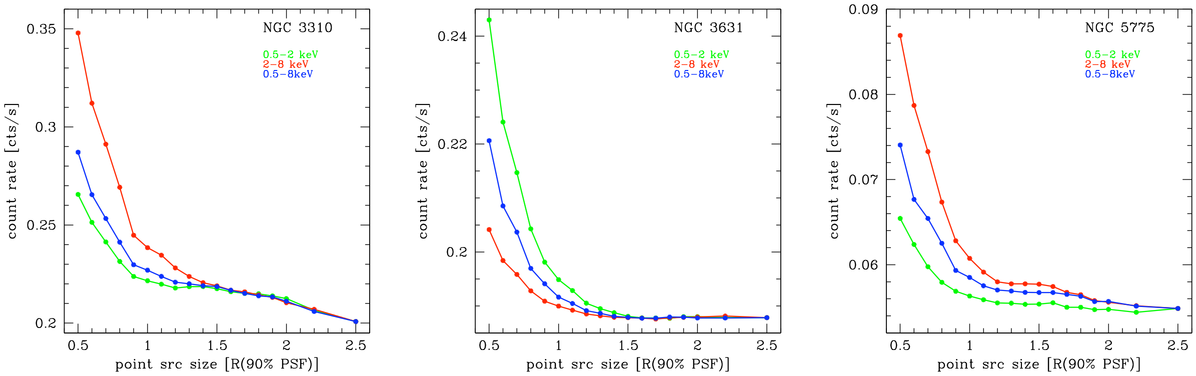

Figure 3.3: Count rate of diffuse emission images after the source removal versus the values of the radius of the removed point source regions in units of $R_{90\%\,\mathrm{PSF}}$ (see Sect. 3.4.1 for details) for the three spiral galaxies chosen as representative of our sample: NGC 3310, NGC 3631 and NGC 5775. The count rate appears to follow a roughly similar trend in the three galaxies analyzed: *i)* a drop off for point source radii $\leq R_{90\%\,\mathrm{PSF}}$, *ii)* a shallower trend for $R_{90\%\,\mathrm{PSF}} < R < 1.5 \cdot R_{90\%\,\mathrm{PSF}}$ and *iii)* a plateau for $R > 1.5 \cdot R_{90\%\,\mathrm{PSF}}$ (which is a monotonic decrease in case of NGC 3310 because of its diffuse emission opulence). That would suggest that an increase of the radius of removed point source circular regions above $1.5 \cdot R_{90\%\,\mathrm{PSF}}$ affects the diffuse emission count rate by less than 10%.

seems to be appropriate to minimize the contamination of diffuse emission by point source counts without compromising the statistics for the diffuse emission itself. The adopted radius for point source removal in all the galaxies of our sample was thus chosen to be $R = 1.5 \cdot\ R_{90\%\,\mathrm{PSF}}$.

3.4.2 Instrumental and cosmic X-ray background

After the removal of discrete point sources we analyzed the X-ray surface brightness profiles in order to account for the instrumental and cosmic X-ray background. We first constructed exposure-corrected radial profiles, with no background subtraction, in the soft ($0.5 - 2.0$ keV) and hard ($2.0 - 8.0$ keV) energy bands. The surface brightness extraction regions were chosen to be concentrical elliptical annuli, centered in the center of the given galaxy, with shape parameters according to the isophotal diameter ratio ($R25$) and the position angle of the major axis (PA) (de Vaucouleurs et al., 1991), extending over the whole *Chandra* detector hosting the galaxy. Based on the characteristics of individual surface brightness profiles, we defined the regions from which to extract the background spectrum as to include all the *Chandra* chip where the galaxy was observed, masking the ellipses corresponding to $D25$, $1.5 \cdot D25$ or $2 \cdot D25$, depending on the particular emission profile of each galaxy.

Once the background regions were defined, we constructed exposure-corrected background-subtracted surface brightness profiles in order to portray the amplitude of statistical errors in the along the *Chandra* detector. We observed that, while the soft X-

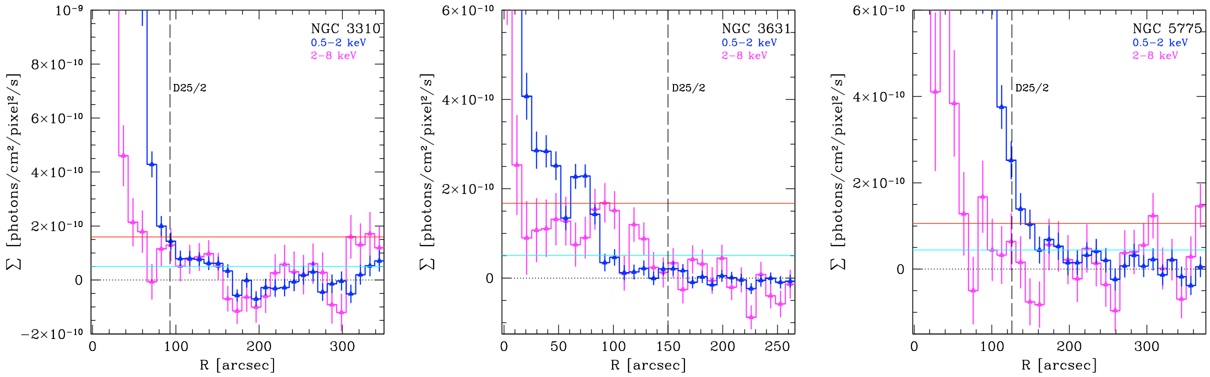

Figure 3.4: An example of exposure-corrected background-subtracted surface brightness profiles in the soft (blue) hard (magenta) bands. The soft X-ray profiles are generally flatter than the hard X-ray profiles at large radii. However, statistically significant brightness fluctuations are seen in both energy bands, in the parts of the image where we believe there is no signal from the galaxy. As they appear to be equally strong in the positive and negative direction, the fluctuations might be no real but resulting from some systematic effects on the image. Their amplitude characterizes the amplitude of statistical errors in the image and suggests that the signal below ∼ 10% of the background level should not be trusted. The red line represents 10% of the background level for hard band, while the cyan blue line represents 10% of the background level for soft band.

ray profiles are generally flatter than the hard X-ray profiles at large radii, statistically significant brightness fluctuations are seen in both energy bands, in the parts of the image where we believe there is no signal from the galaxy. These fluctuations might be no real, as they are equally strong in the positive and negative direction. This suggests that they would result from some systematic effects on the image. Their amplitude characterizes the amplitude of statistical errors in the image and suggests that the signal below ∼ 10% of the background level should not be trusted (see Fig. 3.4).

3.4.3 Spillover counts from ULXs

Although the adjustment of the source region size allowed us to minimize the contamination of diffuse emission by spillover counts from point sources, residual counts from extremely bright compact sources still pollute significantly the unresolved X-ray emission. In two galaxies, NGC 1313 and NGC 5474, the presence of an excess of X-ray counts from compact sources was highlighted against the typically smooth trend of the galactic surface brightness profile, after having removed the point sources. The contamination was recognized to be due to ULXs hosted by these galaxies and it was accounted for using the following method. The *Chandra* PSF in the position of the X-ray compact sources was first extracted using the `mkpsf` task. The surface brightness profiles of both the observed point source and the PSF at its position were constructed and re-normalized in order to be compared (see Fig.

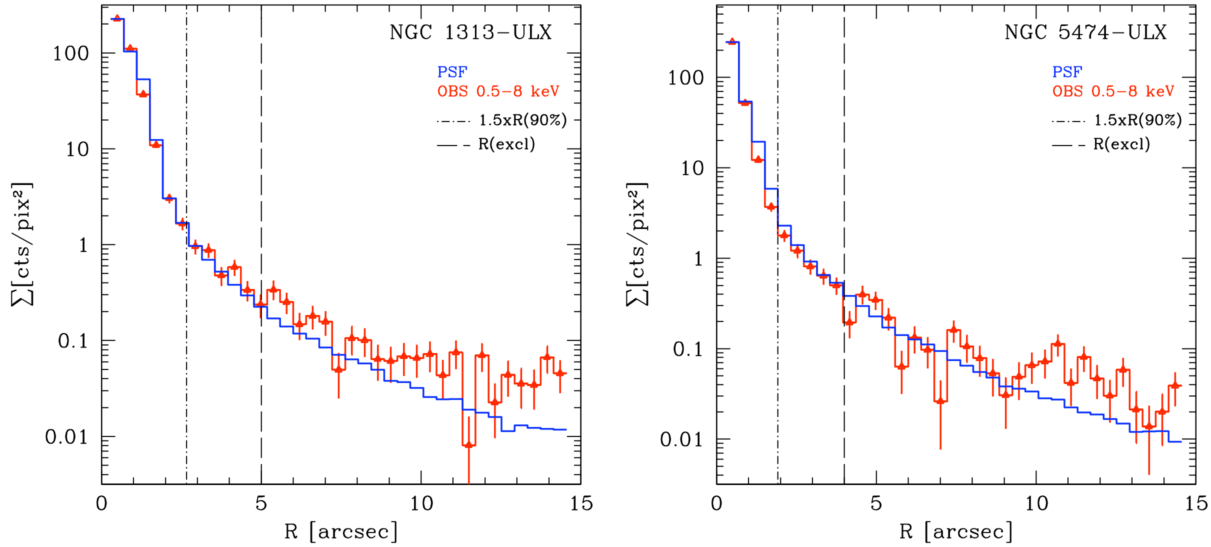

Figure 3.5: Full band (0.5 − 8 keV) surface brightness of the individual ULXs (red) detected in NGC 1313 (*left*) and NGC 5474 (*right*), compared with the PSF of *Chandra* ACIS-S detector at their respective positions (blue). The dotted-dashed line represents the radius of the point source corresponding to $1.5 \cdot R_{90\%\,\mathrm{PSF}}$, whose exclusion was not enough to avoid contamination of the diffuse emission by ULX counts. The dashed line is the radius of the point source which was actually excluded, based on the analysis of the surface brightness profiles described in Sect. 3.4.3.

3.5). As it is clear form Fig. 3.5, the observed and PSF radial profiles show agreement up to $\sim 5-10$ arcsec. Therefore, excluding a circle with radius $R = 1.5 \cdot R_{90\%\,\mathrm{PSF}}$ for these two compact sources was inappropriate. In these cases, we have removed a circle with radius of $\sim 4-5$ arcsec from the image, which allowed us to keep the contamination from the point source spillover counts lower than 10%, without affecting the statistics of the diffuse emission. Then we re-construct the galaxy surface brightness profile again, which showed the typically smooth trend of a galactic profile.

3.4.4 Unresolved high-mass X-ray binaries

The contribution of unresolved HMXBs to the X-ray diffuse emission spectrum of each galaxy was removed statistically, based on the combined spectrum of the faintest point sources and on the average X-ray luminosity function of HMXB.

We combined the spectra of all the compact sources with $\log L_X < 37.5$ detected in the galaxies from our subsample. The latter luminosity limit was chosen based on the quality of the resulting spectrum. The spectrum of each detected point source was extracted from a circular region centered on the source central coordinates given by `wavdetect` output, having radius equal to $R_{90\%\,\mathrm{PSF}}$. For the background region we used a circle

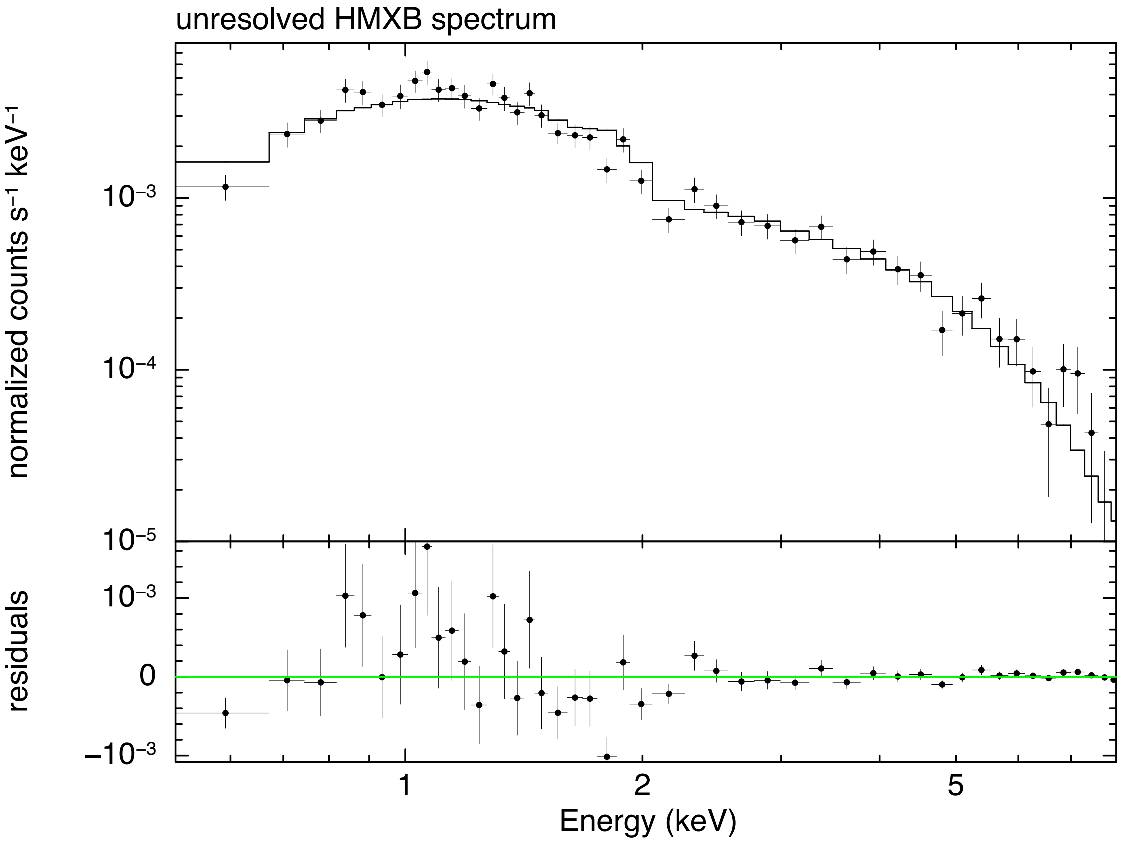

Figure 3.6: The average spectrum of unresolved HMXBs. It was obtained by combining the spectrum of multiple faint point sources (see Sect. 3.4.4 for details). The best-fitting model is an absorbed power law with $N_{\rm H} = 2.2 \cdot 10^{21}$ cm^{-2} and photon index $\Gamma = 1.7$. For each galaxy the model was normalized in order to give the expected $0.5 - 8$ keV band luminosity of unresolved HMXBs.

with radius 3 times the radius of the source region from which we subtracted all the overlapping neighboring point source regions. Average spectra of multiple point sources from each galaxy were extracted and weighted ARFs and RMFs were obtained, using the tasks `dmextract`, `mkwarf` and `mkrmf`. These spectra were then combined into one using the task `combine_spectra`.

The resulting spectrum, shown in Fig. 3.6, was characterized by having low numbers of counts per channel and a insignificant contribution of background spectrum, therefore we used Cash statistics for the fitting procedure. We modeled the combined spectrum of faint X-ray compact sources with an absorbed power law model (`phabs*powerlaw`). We noted the evidence for a ”soft-excess”, which may be related with the contribution of populations of soft sources as SNRs. The latter are in fact amply observed in the spiral arms of late-type galaxies. However, the deviations from the absorbed power law model are $< 20 - 30\%$, which is sufficient for our purpose. So, we took as best-fitting model the simple absorbed power law and obtained as best-fitting parameters a hydrogen column density of $N_{\mathrm{H}} = 2.2 \cdot 10^{21}$ cm^{-2} and power law photon index $\Gamma = 1.7$ (C-statistic = 537.14 with 509 degrees of freedom). For each galaxy the model was normalized in order to give the expected $0.5-8$ keV band luminosity of unresolved HMXBs. The latter was calculated by integrating the average X-ray luminosity function for HMXBs, eq. (4.5), between 10^{34} erg/s and the sensitivity limit L_{lim}, determining its normalization so that the predicted and observed number of point sources with luminosity $L_{\mathrm{X}} > L_{\mathrm{lim}}$ coincide.

The contribution of unresolved HMXBs to the spectrum of the diffuse X-ray emission was accounted for by including the latter model as a component of the spectral model used in all of our fits, which is described in Sect. 3.5.

3.5 X-ray spectral analysis of the diffuse emission

After having excluded the point source regions as it is described in Sect. 3.4.1, we extracted the X-ray spectra of the diffuse emission for each galaxy from the elliptical region defined in Sect. 3.3.3, using the CIAO script `specextract`. We grouped the spectra in order to have minimum 15 counts per channel to apply the χ^2 fitting. The background spectra were extracted according to the description in with Sect. 3.4.2. As all the galaxies studied were observed within one chip of the *Chandra* detector, the so defined background regions account for both the instrumental and cosmic X-ray background.

As our goal is to compare the global properties of our sample galaxies in a consistent manner, we have used the same spectral model in all of our fits. The spectrum of diffuse emission was modeled with a thermal component (`mekal`) and a power law that accounts for the hard X-ray tail which was observed in some of the galaxies. To this model we applied a double photoelectric absorption component (`phabs*phabs`), of which one was fixed to the Galactic value and the second was left as free parameter for estimating the intrinsic hydrogen column density.

In order to account for the contribution of unresolved high-mass X-ray binaries we added to the latter model a second absorbed power law component (`phabs*powerlaw`), whose parameters were set as described in Sect.3.4.4.

The overall model used to fit all the spectra of diffuse X-ray emission can be summarized as follows:

$$[(\mathtt{phabs}_{\mathtt{Gal}})*(\mathtt{phabs}_{\mathtt{intr}})*(\mathtt{mekal+pow})]_{\mathtt{diff}}+(\mathtt{phabs*pow})^{\mathtt{unres}}_{\mathtt{HMXB}}$$

This model provided a reasonable fit to all the diffuse spectra. In all cases a thermal component with average plasma temperature of ~ 0.24 keV was required. Three spectra (NGC 1569, NGC 3079 and NGC 3310) required a second thermal component at ~ 0.68 keV, whise statistical significance was confirmed by performing the F-test. These spectral characteristics are typical of the diffuse emission from normal and starburst galaxies and consistent with measurements published by other authors for several galaxies of the sample (e.g. Grimes et al., 2005; Strickland et al., 2004). For 7 galaxies (NGC 2139, NGC 3556, NGC 3631, N GC 4625, NGC 5474, UGC 05720) the power law slope was poorly constrained. In these cases we fixed the slope to the average value of 2.91, resulting from the rest of the sample. Same procedure was applied in three cases (NGC 4625, NGC 5474, UGC 05720) due to a bad constraint plasma temperature for the `mekal` component, whose average value is 0.24 keV. The X-ray spectra of diffuse emission are shown in Fig.3.7 for the sample galaxies, along with the 15% of background contribution (red) and the predicted contribution of unresolved HMXBs (green).

The diffuse emission spectra of some galaxies show the evidence for a "hard-tail" component. This feature has been pointed out by several authors and mostly explained as attributable to an unresolved population of relatively hard discrete sources (e.g. Owen & Warwick, 2009). Although reasonable, this hypothesis is not always supported by observational evidence. In a few galaxies of our sample (e.g. NGC 1569, NGC 3310, NGC 4194) the hard-tail is clearly not attributable to the unresolved population of HMXBs (see the relative spectra in Fig. 3.7). Using the scaling-law from Gilfanov (2004), based on the stellar mass galaxies, we estimated that neither the contribution of unresolved LMXBs can explain the observed hard tail. On the other hand, in the spectrum of other galaxies (e.g. NGC 3631, NGC 4625 , UGC 05720) hard tail is not even observed, either because really inexistent or contaminated by the background emission. Although this interesting problem would deserve further investigation, the latter is beyond the scope of the present work and will be fully addressed in a forthcoming publication.

3.6 Multiwavelength analysis

For SFR estimations we used data from Spitzer and GALEX archives, the stellar mass was estimated from 2MASS images. For the galaxies from the resolved sample we computed SFR and mass inside the analysis regions defined in the previous section. For the galaxies of high-SFR sample we did the measurements in the D25 regions.

3.6.1 Far-infrared

We analyzed MIPS 70 μm and 24 μm Large Field images. In particular, we used the "post Basic Calibrated Data" products provided by the Spitzer Space Telescope Data archive[2]. These are images calibrated in MJy/sr, suitable for photometric measurements. We did not analyze MIPS 160 μm images because for most of the galaxies in our sample only "Small Field" images were available. This operating mode often covers only a fraction of galaxy. For three galaxies (NGC 7541, NGC 2139 and NGC 3631) neither MIPS 70 μm nor 24 μm data were available. For NGC 3034 (M 82) Spitzer data are affected by saturation effects that limit our ability to extract reliable global flux densities. In these cases we used published *IRAS* data (Sanders et al., 2003) to compute the IR luminosity.

After having subtracted the background counts, the total net counts were converted from units of MJy/sr into Jy using the following conversion factors, which take into account

---

[2] http://irsa.ipac.caltech.edu/applications/Spitzer/Spitzer/

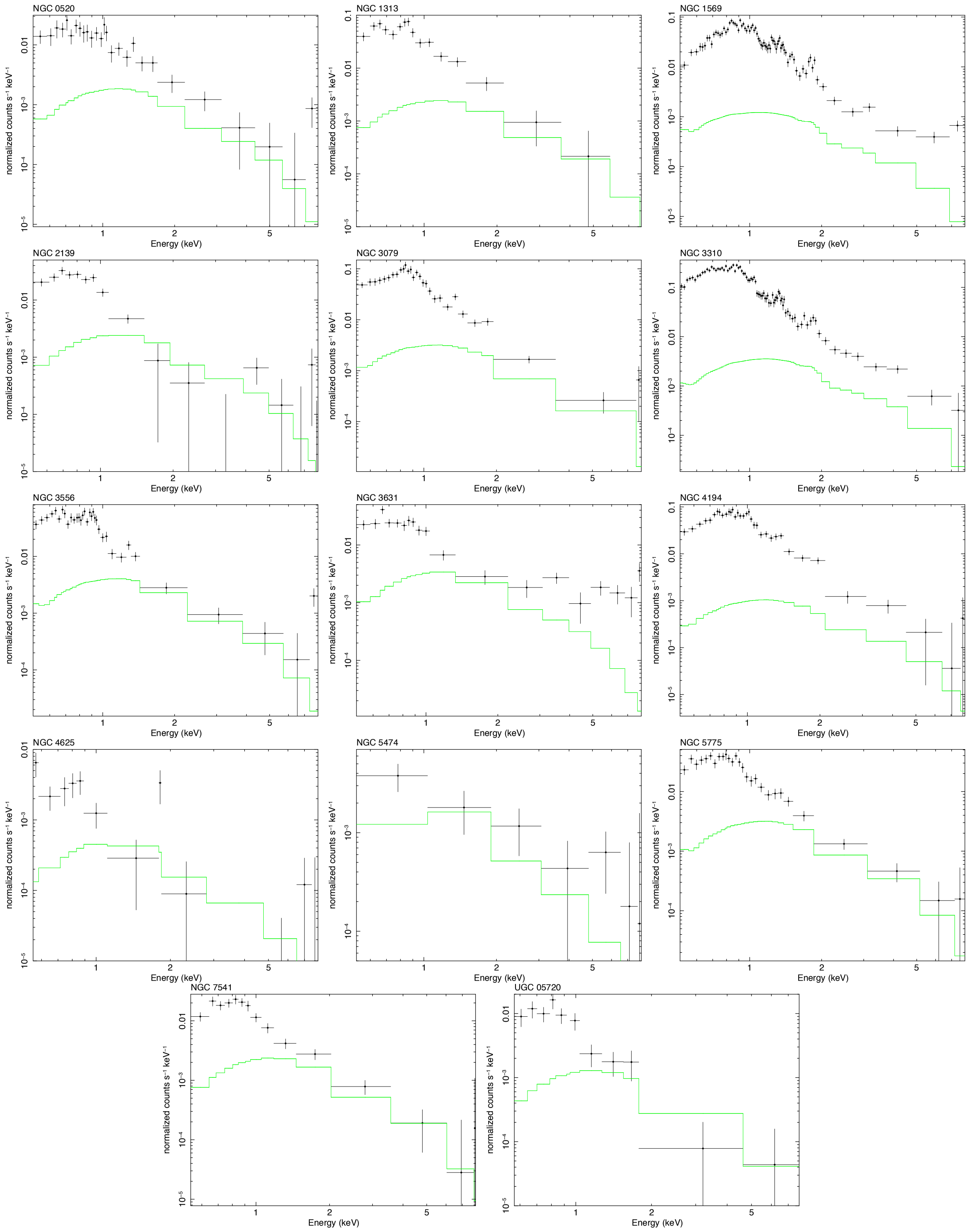

Figure 3.7: The observed spectra of diffuse X-ray emission (black) for the sample galaxies; 15% of background contribution (red) and predicted contribution of unresolved HMXBs (green).

the pixel size of MIPS 70 μm and 24 μm detectors:

$$C_{70\,\mu\mathrm{m}} = 3.76 \times 10^{-4}; \quad C_{24\,\mu\mathrm{m}} = 1.41 \times 10^{-4} \tag{3.4}$$

The monochromatic fluxes (Jy) at 24 μm and 70 μm were then converted into spectral luminosities (erg/s/Hz). The total IR luminosity ($8 - 1000\,\mu$m) was estimated using the relations from Bavouzet et al. (2008), which give L_{IR} in units of solar luminosity $L_\odot = 3.839 \times 10^{33}$ erg/s.:

$$L_{\mathrm{IR}}(L_\odot) = 7.90 \times (\nu L_\nu)^{0.94}_{70\,\mu\mathrm{m,rest}} \tag{3.5}$$

$$L_{\mathrm{IR}}(L_\odot) = 6856 \times (\nu L_\nu)^{0.71}_{24\,\mu\mathrm{m,rest}} \tag{3.6}$$

We preferentially used equation (3.5), as it has a ~ 3 times smaller dispersion than eq. (3.6) (see Bavouzet et al., 2008, for details).

3.6.2 Near-infrared

The near-infrared analysis was performed using the K_S (2.16 μm) images and mosaics of 2MASS All-Sky Extended Source Catalog[3] (XSC) and Large Galaxy Atlas[4] (LGA). We converted the source counts measured on images into calibrated magnitudes using the zero point magnitude KMAGZP given in the image header:

$$m_\mathrm{K}(\mathrm{mag}) = \mathrm{KMAGZP} - 2.5\log(S) \tag{3.7}$$

where S is the integrated, background-subtracted flux in data-number units (”DN”) measured within the selected galactic region. After having obtained K_S magnitudes, we estimated the K_S-band luminosity and, following Gilfanov (2004), the stellar mass.

3.6.3 Ultraviolet

We based the ultraviolet analysis on GALEX NUV and FUV background-subtracted intensity maps publicly available in the archive of GR4/GR5 Data Release[5]. These are images calibrated in units of counts per pixel per second, corrected for the relative response, with the background removed. We converted the net counts to flux using the conversion factors[6] between GALEX count rate (ct/s) and flux (erg/cm^2/s/$\AA$):

$$C_\mathrm{FUV} = 1.40 \times 10^{-15}; \quad C_\mathrm{NUV} = 2.06 \times 10^{-16} \tag{3.8}$$

The fluxes were then converted into monochromatic luminosities (erg/s/$\AA$) at 1529 $\AA$ (FUV) and 2312 $\AA$ (NUV). For three galaxies of our sample (NGC 0278, NGC 4194 and NGC 7541) neither NUV nor FUV data were available. Their treatment is discussed later.

---

[3] http://irsa.ipac.caltech.edu/applications/2MASS/PubGalPS/

[4] http://irsa.ipac.caltech.edu/applications/2MASS/LGA/

[5] http://galex.stsci.edu/GR4/?page=mastform

[6] http://galexgi.gsfc.nasa.gov/docs/galex/FAQ/counts_background.html

3.7 Star formation rate

We used a complex SFR proxy that takes into account both the UV light escaping the galaxy and the IR emission of the dust heated by young stars (Bell, 2003; Hirashita, Buat, & Inoue, 2003; Iglesias-Páramo et al., 2004, 2006). It has the advantage of being free of the model dependence for the attenuation correction of the UV emission. It contains also a correction factor, η, accounting for the fraction of the IR emission due to old stellar population in normal star-forming galaxies:

$$\mathrm{SFR_{tot}} = \mathrm{SFR}^0_{\mathrm{NUV}} + (1-\eta)\mathrm{SFR_{IR}} \tag{3.9}$$

where $\mathrm{SFR}^0_{\mathrm{NUV}}$ and $\mathrm{SFR_{IR}}$ are obtained assuming a Salpeter IMF from 0.1 to 100 $M_\odot$:

$$\mathrm{SFR_{IR}}(M_\odot\,\mathrm{yr}^{-1}) = 4.6\times10^{-44} L_{\mathrm{IR}}(\mathrm{erg\,s^{-1}}) \tag{3.10}$$

$$\mathrm{SFR}^0_{\mathrm{NUV}}(M_\odot\,\mathrm{yr}^{-1}) = 1.2\times10^{-43} L_{\mathrm{NUV,obs}}(\mathrm{erg\,s^{-1}}) \tag{3.11}$$

$L_{\mathrm{NUV,obs}}$ is the observed NUV (2312 $\mathring{A}$) luminosity, i.e. uncorrected for dust attenuation, and L_{IR} is the $8-1000\,\mu$m luminosity. Eqs. (3.10) and (3.11) by Iglesias-Páramo et al. (2006) are consistent with those of Kennicutt (1998) within 3% and 10% respectively. The second term in eq. (3.9) is very similar to the calibration of Bell (2003) (their eq. (5)). The quantity η is the cirrus correction, i.e. the fraction of IR luminosity due to old stellar population. It depends on the type of the galaxy but accurate values for individual galaxies are difficult to determine, therefore average values are usually used. We use results of Hirashita, Buat, & Inoue (2003):

$$\eta \approx \begin{cases} 0.4 & \text{for normal disk galaxies} \\ 0 & \text{for starbursts} \end{cases} \tag{3.12}$$

To be consistent with Hirashita, Buat, & Inoue (2003), we used the atlas of Kinney et al. (1993) to classify the objects of our sample as starbursts or normal star-forming galaxies and use the appropriate value of η in computing the SFR. This definition is similar, but not identical to the one used by Bell (2003) ($\eta \sim 0.32$ for galaxies having $L_{\mathrm{IR}} > 10^{11} L_\odot$ and $\eta \sim 0.09$ for galaxies having $L_{\mathrm{IR}} \leq 10^{11} L_\odot$).

For each of the three galaxies with no UV data available (see Sect. 3.6.3), we determined the average value of the $L_{\mathrm{NUV,obs}}/L_{\mathrm{IR}}$ ratio for galaxies of similar Hubble type and inclination. We obtained values in the range $0.08-0.4$. This ratio was used to estimate $L_{\mathrm{NUV,obs}}$ from L_{IR} and then eq.(3.9) was applied.

The SFRs for HDFN galaxies were computed based on their 1.4 GHz luminosities and calibration of Bell (2003):

$$\mathrm{SFR}(M_\odot\,\mathrm{yr}^{-1}) = 5.55\times10^{-29} L_{1.4\,\mathrm{GHz}}(\mathrm{erg\,s^{-1}}) \tag{3.13}$$

In Fig. 3.8 we present the two samples of star-forming galaxies in the $\mathrm{SFR}-M_\star$ plane.

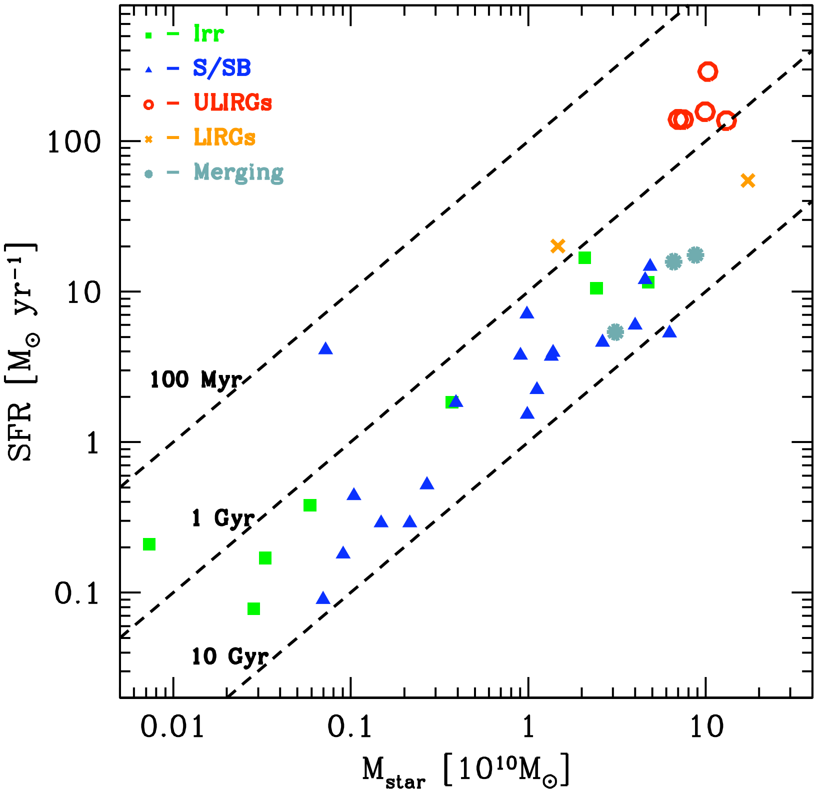

Figure 3.8: The SFR – $M_\star$ plane. Different types of galaxies are plotted with different symbols. The dashed lines correspond to constant stellar-mass-to-SFR ratio.

Chapter 4

High-mass X-ray binaries

4.1 Introduction

The recent star formation rate of a galaxy is primarily measured from the light emitted by massive stars: given their short lifetimes, their collective luminosity is, to the first approximation, proportional to the rate at which they are currently being formed. The scale factors relating luminosities at different wavelengths and SFR are usually derived from stellar population synthesis models (see review by Kennicutt, 1998). Most of the conventional SFR indicators are known to be subject to various uncertainties, one of which is caused by the interstellar extinction.

An alternative method of SFR determination is based on the X-ray emission of a galaxy (Sunyaev, Tinsley, & Meier, 1978; Grimm, Gilfanov, & Sunyaev, 2003; Ranalli, Comastri, & Setti, 2003). Indeed, X-ray output of a normal gas-poor galaxy is dominated by the collective emission of its X-ray binary (XRB) population (see review by Fabbiano, 2006). As the evolutionary time scale of high-mass X-ray binaries does not exceed $\sim$ few $\times 10^7$ yrs, their X-ray emission is nearly prompt (Shtykovskiy & Gilfanov, 2007). That makes them a potentially good tracer of the recent star formation activity in the host galaxy. However, in distant galaxies, emission from HMXBs can not be separated from that of low-mass X-ray binaries (LMXBs) having much longer evolutionary time scales and therefore unrelated to recent star-formation or from the contribution of the supermassive black hole. For this reason the X-ray based method is suitable for young normal galaxies with sufficiently large value of the specific, per unit stellar mass, SFR, the X-ray output of which is dominated by HMXBs. Due to large penetrating power of X-rays, the X-ray based method is much less affected by absorption than conventional indicators. This makes it an important tool for cross-calibration of different SFR proxies and for star-formation diagnostics in galaxies, especially in the distant ones.

Although the theoretical idea was formulated in the 70-ies (Sunyaev, Tinsley, & Meier, 1978) and the first supporting evidence was obtained in 90-ies (David, Jones, & Forman, 1992), the full observational justification and calibration of the method required outstanding angular resolution and could be achieved only with advent of Chandra. During the decade following its launch several authors have discussed the X-ray emission of compact sources and its relation to the SFR of the host galaxy (Grimm, Gilfanov, & Sunyaev, 2003; Ranalli, Comastri, & Setti, 2003; Persic & Rephaeli, 2007). All these works have established a general agreement regarding the correlation of the X-ray luminosity with SFR, however there was some discrepancy between the scale factors derived by different authors. In addition, a notable dispersion in the relation was observed. One of the limiting factors of previous studies was the heterogeneous nature of the X-ray and SFR data. With the large numbers of galaxies now available in *Chandra*, Spitzer and GALEX public data archives it has become possible to construct large samples of galaxies for which homogeneous sets of multiwavelength measurements are available. This motivated us to revisit the problem of the $L_{\mathrm{X}} - \mathrm{SFR}$ relation in order to obtain its more accurate calibration and understand the origin of the dispersion seen in previous studies.

Study of the populations of HMXBs and its dependence on the metallicity and other properties of the host galaxy is of considerable interest on its own. The specific luminosity and numbers of sources as well as their luminosity distribution can be used for verification and calibration of the binary evolution and population synthesis models. Grimm, Gilfanov, & Sunyaev (2003) showed that in a wide range of SFR, the luminosity distribution of HMXBs in a galaxy can be approximately described by a universal luminosity function, which is a power law with slope of ~ 1.6, whose normalization is proportional to the SFR. They searched for features in the averaged XLF of nearby galaxies, corresponding to the Eddington luminosities of neutron stars and black holes, but did not find any. Among other reasons, of a more physical nature, they also considered the possibility of various systematic effects (e.g. distance uncertainties) which could smear and dilute the expected features. A larger sample of galaxies with well controlled systematic uncertainties may allow a substantial progress in this direction.

4.2 The luminosity function

The Fig. 4.1 shows cumulative luminosity distributions for all galaxies from the primary sample, normalized to their respective SFRs. It is apparent that although shapes of the distributions are similar, there is a considerable dispersion in their normalizations. Their amplitude and significance will be discussed later in this section.

4.2.1 Average XLF of HMXBs

We construct the average luminosity function combining the data for all resolved galaxies. It includes over 700 compact sources. An intuitive and straightforward method would be to bin the sources into e.g. logarithmically spaced bins and normalized the result by the sum of the SFR of all galaxies contributing to the given luminosity bins. The latter step is required to account for the fact that different galaxies have different point source detection sensitivity. However, because of the considerable dispersion in the normalizations (Fig.4.1), the so computed luminosity function may have a number of artificial steps and features at

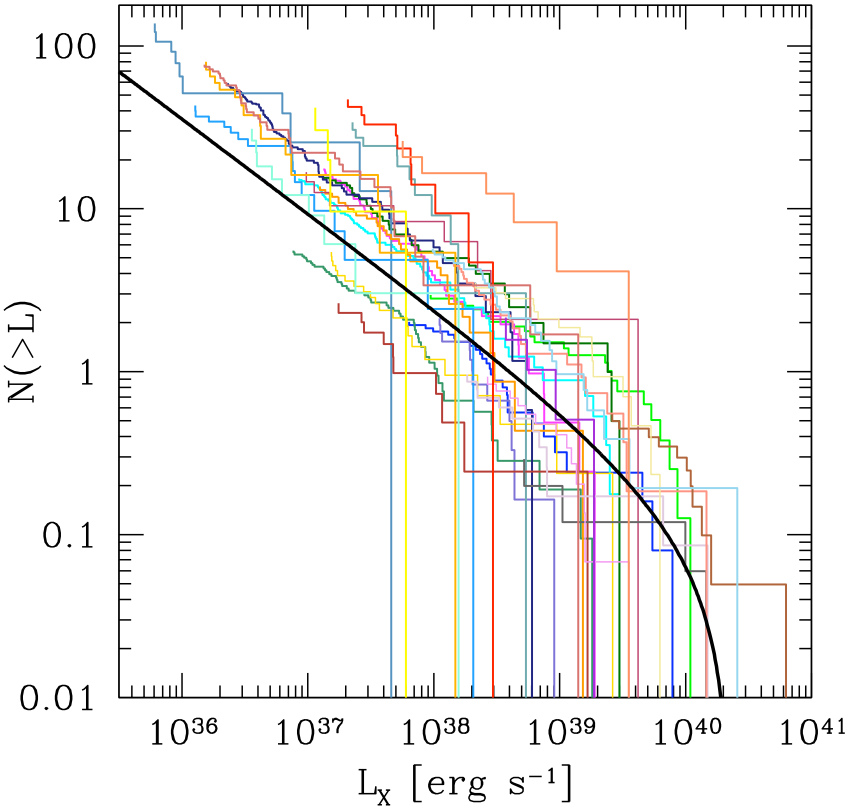

Figure 4.1: Cumulative X-ray luminosity functions of the galaxies from primary sample, normalized by their respective SFRs. The solid line is the cumulative XLF per unit SFR, given by integration of the equation (4.5).

the luminosities, corresponding to the luminosity limits of particular galaxies. In order to deal with this problem we used the following method.

Considering that there is much larger dispersion in normalization than in the shape of the XLF in individual galaxies, we write for the luminosity distribution in the k-th galaxy:

$$\left(\frac{dN}{dL}\right)_k = \xi_k \, \mathrm{SFR}_k \, f(L) \tag{4.1}$$

where SFR_k is star-formation rate in the k-th galaxy, ξ_k – the XLF normalization and the function $f(L)$ describes the XLF shape, assumed to be same in all galaxies, which we would like to determine. The number of sources in the j-th luminosity bin, $\Delta N(L_j)$, is:

$$\Delta N(L_j) = \sum_k \Delta N_k(L_j) = f(L_j)\,\Delta L_j \sum_k \mathrm{SFR}_k \xi_k \tag{4.2}$$

where $\Delta N_k(L_j)$ is the CXB-subtracted number of compact sources in the k-th galaxy in the j-th luminosity bin and summation is performed over all galaxies of the sample. The $f(L)$ can be determined as:

$$f(L_j) = \frac{1}{\Delta L_j} \frac{\sum_k \Delta N_k}{\sum_k \mathrm{SFR}_k \, \xi_k} \tag{4.3}$$

For a power law luminosity function $f(L) = L^{-\gamma}$ the ξ_k are calculated as:

$$\xi_k = \frac{1-\gamma}{\mathrm{SFR}_k} \frac{N_k(>L_{\mathrm{th},k}) - N_{\mathrm{CXB}}(>F_{\mathrm{th},k})}{(L_{\mathrm{th},k}^{-\gamma+1} - L_{\mathrm{cut}}^{-\gamma+1})} \tag{4.4}$$

where $L_{\mathrm{th},k}$ is the sensitivity limit for the k-th galaxy, $N_k(>L_{\mathrm{th},k})$ is the number of sources detected above this sensitivity limit, $N_{\mathrm{CXB}}(>F_{th,k})$ is the predicted number of resolved CXB sources above the corresponding flux limit $F_{th,k} = L_{th,k}/4\pi D_k^2$, L_{cut} is the high luminosity cut-off of the XLF. As it is obvious from eq.(4.3) and (4.4), the so computed $f(L)$ is independent from SFR_k.

To compute ξ_k we used a two-step iterative procedure. At the first step we assumed $\gamma = 1.6$, $L_{\mathrm{cut}} = 2.1 \cdot 10^{40}$ erg/s (Grimm, Gilfanov, & Sunyaev, 2003) and computed the XLF using eqs.(4.3) and (4.4). The $L_{\mathrm{th},k}$ was set to 1.5 times the completeness limit for each galaxy. The obtained luminosity function was fit with a broken power law

$$\frac{\mathrm{d}N}{\mathrm{d}L_{38}} = \xi\,\mathrm{SFR} \times \begin{cases} L_{38}^{-\gamma_1}, & L_{38} < L_b \\ \\ L_b^{\gamma_2-\gamma_1}\, L_{38}^{-\gamma_2}, & L_b \le L_{38} \le L_{\mathrm{cut}} \end{cases} \tag{4.5}$$

where $L_{38} = L_{\mathrm{X}}/10^{38}$erg/s, L_b is the break luminosity, SFR is in units of $M_\odot\,\mathrm{yr}^{-1}$ and ξ is the average normalization. The fit was done on unbinned data using maximum-likelihood (ML) method, the predicted contribution of resolved CXB sources was included in the model as described below. Using this model and its best-fit parameters we calculated more

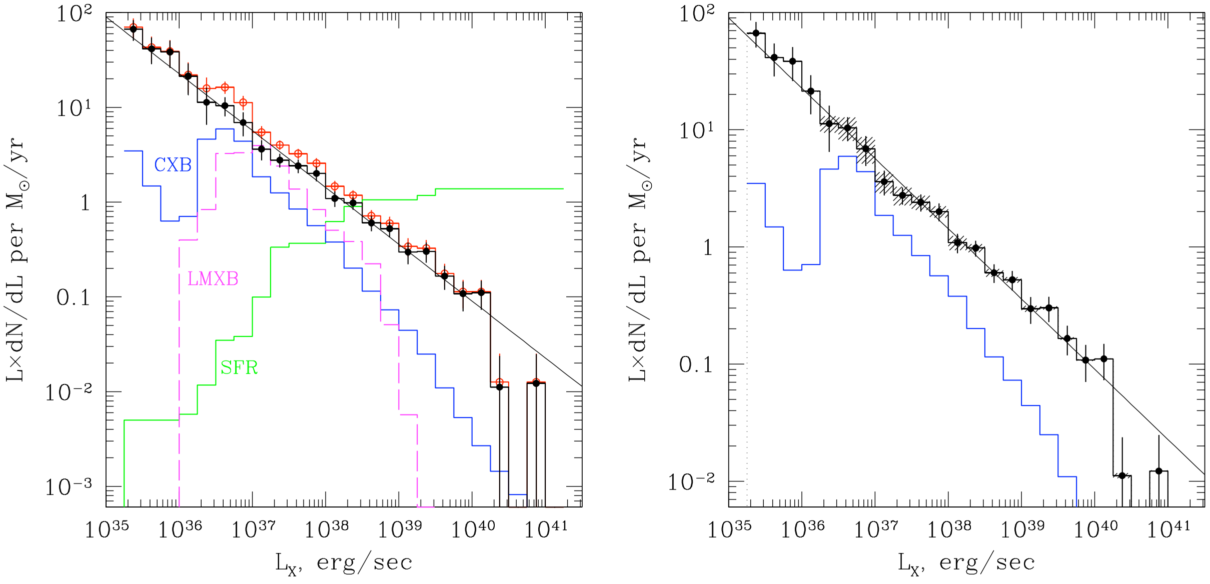

Figure 4.2: The luminosity functions obtained by combining data of all the galaxies of the primary sample, normalized by SFR. *Left:* The top histogram with error bars (open circles, red) shows the luminosity distribution of all compact sources. The two histograms peaked near $\log(L_X) \sim 37$ are predicted contributions of resolved CXB (blue) and LMXB (magenta, dashed) sources. The latter was computed using the average scaling relations for nearby early type galaxies from Gilfanov (2004), irrespective of their age. Apparently, it grossly overestimates the LMXB numbers, therefore no attempt to subtracts their contribution was made. The histogram marked with solid circles (black) shows the luminosity distribution of compact sources with the CXB contribution subtracted. It is our best approximation to the average HMXB XLF in nearby galaxies. The histogram marked "SFR" (green) shows the total SFR of all galaxies contributing to a given luminosity bin in the XLF. *Right:* The CXB subtracted luminosity distribution from the left panel. The shaded area indicates the range of uncertainties corresponding to 40% uncertainty in the CXB normalization. The solid line on both panels shows a power law with parameters according to eq.(4.5).

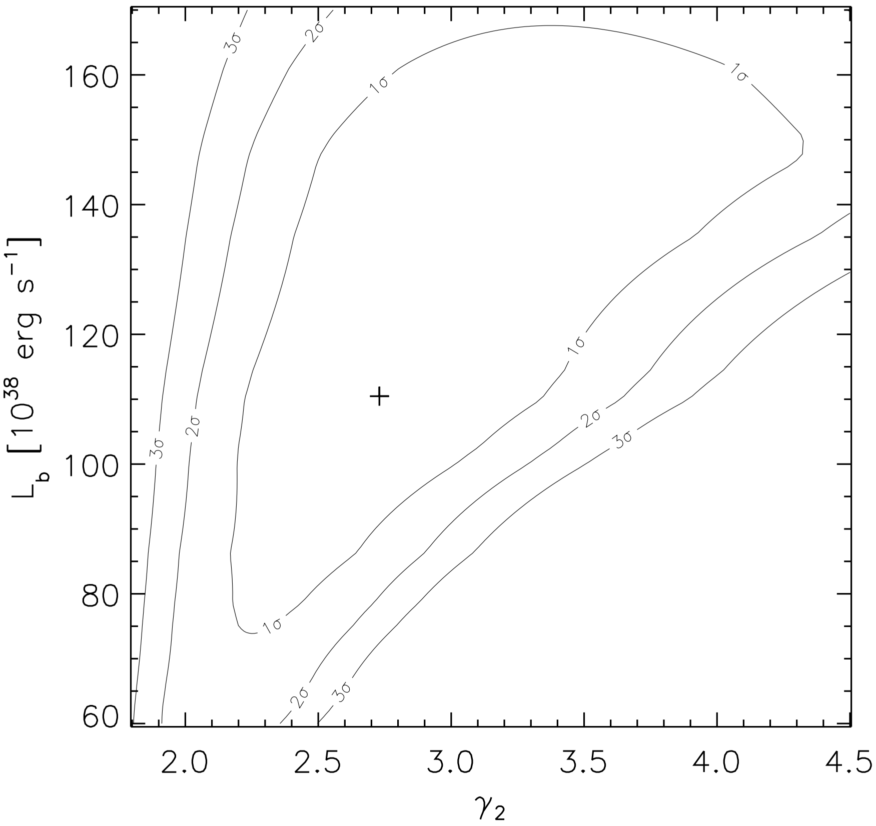

Figure 4.3: The error contours for the XLF break parameters: break luminosity L_b and the power law index after the break γ_2. The cross indicates the best fit values.

accurate values of ξ_k and repeated the procedure. We obtained the following best-fit values for the XLF parameters: $\gamma_1 = 1.58 \pm 0.02$, $\gamma_2 = 2.73^{+1.58}_{-0.54}$, $L_b = 110^{+57}_{-34}$, $\xi = 1.49 \pm 0.07$. The value of the high-luminosity cut-off was fixed at $L_{\rm cut} = 5 \times 10^3$, the result being virtually independent on this choice. The final luminosity distribution is shown in Fig. 4.2. The obtained XLF and its parameters are remarkably similar to the one determined by Grimm, Gilfanov, & Sunyaev (2003). Correspondingly, the second step of this procedure does not has any noticeable effect.

The statistical uncertainty of the slope γ_1 of the average XLF, quoted above is rather small, thanks to the large number of sources involved in its determination. The rms of individual slopes around their average value is much bigger, and is investigated in the section 4.2.4

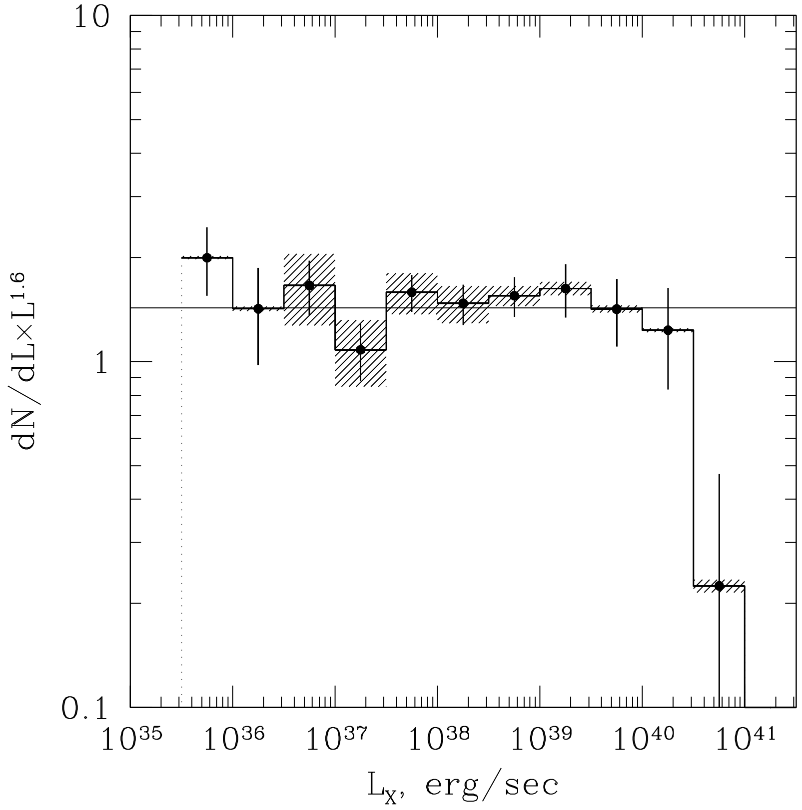

Figure 4.4: The CXB subtracted XLF of compact sources, multiplied by $L^{1.6}$. The shaded are has same meaning as in Fig.4.2.

4.2.2 High-luminosity break

The best fit XLF model has a break at $L_X \approx 1.1 \times 10^{40}$ erg/s. To access its significance we compare observed number of bright sources with the predictions of the single slope power law model. The best fit parameters of the latter are: $\gamma = 1.60 \pm 0.02$, $\xi = 1.49 \pm 0.07$. This model predicts ≈ 21.1 sources above $L_X = 10^{40}$ erg/s, whereas we detected 11 sources. The discrepancy between the data and the model is $\approx 2.5\sigma$, without account for the arbitrariness in the choice of the threshold luminosity, i.e. is marginally significant.

The error contours for the break luminosity and the XLF slope after the break are shown in Fig. 4.3, demonstrating that the break parameters are not very well constrained, which is not surprising given its low statistical significance.

4.2.3 Contribution of LMXBs and CXB sources

Expected contributions of resolved CXB and LMXB sources to the XLF are shown in Fig. 4.2. They were computed summing up individual predictions for all galaxies contributing sources to the given luminosity bin and then renormalizing the total in the same way as the XLF itself. For LMXBs we used the average scaling relation for nearby early type galaxies from Gilfanov (2004), for CXB sources we used the $\log N - \log S$ determined by Georgakakis et al. (2008).

Both predictions bear uncertainties which may affect the resulting HMXB XLF. In the case of the CXB contribution, the uncertainties are caused by angular fluctuations of the density of background AGN and are likely to be reduced as a result of averaging over a rather large number of galaxies involved in the calculation of XLF. However, their final amplitude is difficult to estimate, we therefore illustrate their possible effect by showing the range of XLF variations corresponding to 40% variations in the CXB normalization (shaded area in the right-hand panel in Fig.4.2). As clear from the Fig.4.2, the CXB contribution is significant and its uncertainties are relatively important in the $\log(L) \sim 36{-}38.5$ luminosity range. It is also clear from the figure that the CXB contribution is predicted with a reasonable accuracy – the amplitude of the feature in the total XLF at $\log(L) \sim 36 - 37$ is consistent with the expected CXB contribution.

Estimation of the LMXB contribution is less straightforward. There is an evidence that the LMXB population may have a rather strong age dependence, being smaller for younger galaxies (Bogdán & Gilfanov, 2010). As the scaling relation of Gilfanov (2004) was computed for a sample of nearby early type galaxies irrespective of their age, it may be not directly applicable to galaxies with significant ongoing star-formation. Indeed, the calculation based on results of Gilfanov (2004) apparently over-predicts LMXB contribution, probably by the factor of a few – its subtraction from the XLF would result in negative values (Fig.4.2). For this reason we decided to subtract only the contribution of CXB sources, until detailed information on scaling relations for LMXBs in late type galaxies becomes available. The part of the XLF affected by this uncertainty is in the $\log(L_{\rm X}) \sim 36.5 - 38.5$ luminosity range.

We note that the bright end of the XLF is virtually free of both contaminating components – the vast majority of sources brighter than $\sim 10^{39}$ erg/s in our sample are high mass X-ray binaries.

4.2.4 XLFs of individual galaxies

We fit XLFs of individual galaxies with a single slope power law with a high luminosity cut-off

$$\frac{dN}{dL_{38}} = A \times L_{38}^{-\gamma}, \qquad L \leq L_{\rm cut} = 10^{41}\ \text{erg/s} \tag{4.6}$$

The cut-off luminosity was fixed at the value, exceeding the luminosity of the brightest source in the sample. Only galaxies having more than 5 sources above the detection threshold were analyzed, the detection threshold being defined as 1.5 times the 80% completeness limit of a given galaxy. The CXB contribution, computed according to Georgakakis et al. (2008), was included as a fixed component of the model. The fit was done with the unbinned data, using the Maximum Likelihood method.

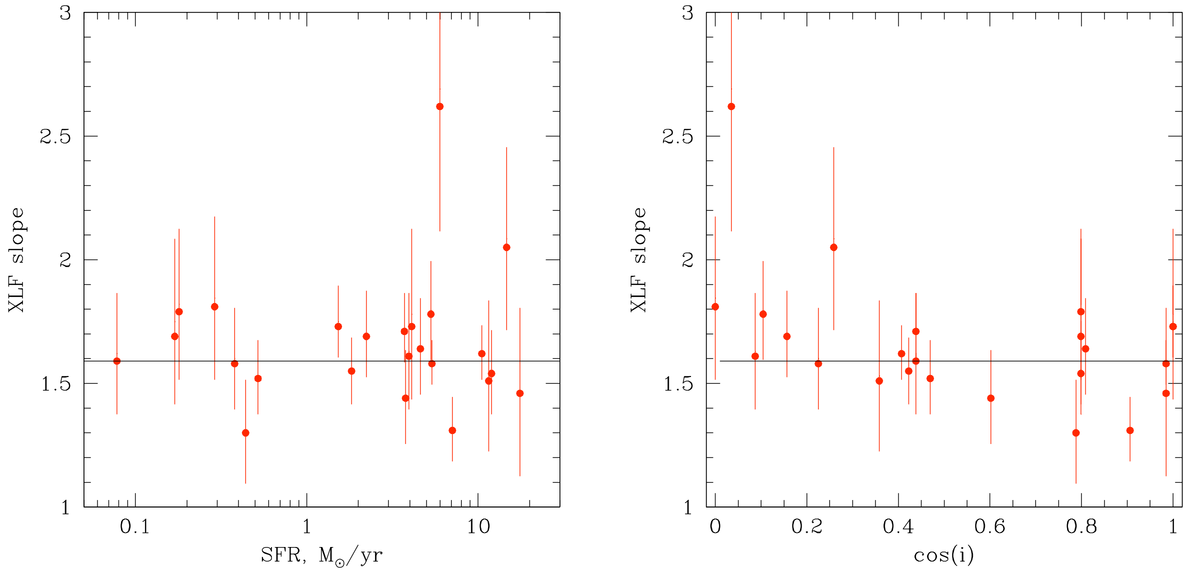

Figure 4.5: XLF slopes for individual galaxies plotted against the SFR *left* and inclination *right* of the galaxy. The horizontal solid line shows the mean value of $\langle\gamma\rangle \approx 1.6$.

The best-fit values of slope are shown in Fig.4.5. The average (computed using χ^2 method) is $\langle\gamma\rangle = 1.59$ with $rms = 0.25$. The $\chi^2 = 16.8$ for 24 degrees of freedom indicates that the data is consistent with the γ being same in all galaxies. The two galaxies deviating from the mean by $\sim 2\sigma$ are NGC3079 ($\gamma = 2.62^{+0.64}_{-0.50}$) and NGC3310 ($\gamma = 1.30^{+0.22}_{-0.20}$).

There is some evidence that the XLF slope depends on the inclination of the galaxy (right panel in Fig.4.5), but it is not statistically significant. The $\chi^2 = 14.2$ for a linear model $\gamma = \gamma_0 + k \times \cos(i)$ with the best fit parameters of $\gamma_0 = 1.71 \pm 0.09$ and $k = -0.22 \pm 0.14$. According to the F-ratio test such a reduction of χ^2 corresponds to a $\approx 2\sigma$ fluctuation. We note however, that the character of the correlation (steeper XLF slopes for more edge-on galaxies) is in accord with the theoretical expectation. Indeed, as the brighter sources (black holes in the soft spectral state) tend to have softer spectra, they are more subject to absorption which is stronger in more edge-on galaxies. This makes the bright end of the XLF to be suppressed in more edge-on galaxies, i.e. their XLFs are expected to be steeper, as observed. No other physically meaningful correlations were seen in the data.

Dependence of the XLF normalization A on the SFR is shown in Fig.4.8. The χ^2 fit to the logarithm of the normalization in the form $\log A = a + \beta \log \mathrm{SFR}$ yields $\beta = 0.73 \pm 0.05$ with very large value of the $\chi^2 = 99.2$ for 23 d.o.f and the $rms = 0.32$ dex. Forcing a linear relation $A = \xi \times \mathrm{SFR}$ we obtained $\xi = 1.88$ with significantly larger $\chi^2 = 130.4$ for 24 d.o.f., but with $rms = 0.34$ dex, just marginally worse than obtained in the non-linear fit. Both best-fit models are shown in Fig.4.8.

The relation between A and SFR can be expressed in terms of the relation between the number of sources above a certain luminosity limit and the star-formation rate:

$$N_{\rm XRB}(L > 10^{38}{\rm erg\,s^{-1}}) = 3.1 \times {\rm SFR}\,(M_\odot\,{\rm yr}^{-1}) \tag{4.7}$$

For our sample of galaxies this relation predicts the number of sources with the accuracy of $rms = 0.34$ dex i.e. within a factor of ~ 2 (rms).

The $\beta \neq 1$ obtained above implies a possible non-linear slope of the relation between XLF normalization (i.e. the number of sources) and SFR. However, neither linear nor non-linear model describes the data adequately ($\chi^2/d.o.f. \sim 4-5$), suggesting that additional parameter(s) play a significant role in this relation. Therefore it is not clear how much weight should be given to the non-linear best fit slope of the $N_{\rm X} - {\rm SFR}$ relation obtained above. It may, for example, be a result of application of an inadequate or incomplete model to a particular selection of galaxies. Alternatively, it may point at a genuine non-linear relation between the number of sources and SFR. A clue may be provided by accurate characterization of the factors which can potentially affect the number of HMXBs in star-forming galaxies, such as metallicity and/or recent star-formation history. With the presently available data, it does not seems to be possible to discriminate between these two possibilities. We note that Grimm, Gilfanov, & Sunyaev (2003), based on a much smaller sample of galaxies, obtained a linear $N_{\rm X} - {\rm SFR}$ relation. Finally, in interpreting the $N_{\rm X} - {\rm SFR}$ and $L_{\rm X} - {\rm SFR}$ relations one should keep in mind that for the XLF slope of ≈ 1.6 the number of sources is defined by faint sources, near the detection limit whereas their total luminosity – by the (sometimes just a few) brightest sources.

4.3 Collective luminosity of HMXBs

The collective X-ray luminosities of X-ray binaries in galaxies from our primary sample were computed as the sum of luminosities of point sources detected above the corresponding sensitivity limit $L_{\rm lim}$. The latter was defined as the luminosity level corresponding to a value of the incompleteness function $K(L) = 0.6$, in the regions selected as described in Sect. 3.3. As *Chandra* observations of different galaxies achieved different sensitivity, these luminosities need to be transformed to the same threshold, which was chosen at $L_{\rm X} = 10^{36}$ erg/s, i.e. the luminosities presented below are an estimate of the combined luminosity of X-ray binaries brighter that this threshold. The luminosity of "missing" unresolved sources was computed by integrating the luminosity function which differential slope was fixed at the average value of $\gamma = 1.58$, determined in section 4.2. The normalization was determined for each galaxy individually, from the number of sources detected above its sensitivity limit, corrected for incompleteness and subtracting the CXB contribution as described in section 4.2. Finally the luminosities were corrected for the contribution of the background AGN to the resolved sources:

$$L^{\rm XRB}_{0.5-8} = \int_{10^{36}}^{L_{\rm lim}} L\frac{{\rm d}N}{{\rm d}L}{\rm d}L + \sum_{L_i \geq L_{\rm lim}} \frac{L_i}{K(L_i)} - 4\pi D^2 F_{\rm CXB} \tag{4.8}$$

where $F_{\rm CXB}$ is the predicted total flux of CXB sources brighter than the flux limit corresponding to $L_{\rm lim}$ computed from the $\log N - \log S$ of Georgakakis et al. (2008) and D is the distance to the galaxy. The CXB contribution did not exceed $\sim 35-40\%$ of the total luminosity of galaxies, in accord with the procedure used to define the analysis regions (Section 3.3.3). For the reasons described in Section 4.2.3, we did not attempt to subtract the contribution of LMXBs.

The obtained $L_{\rm XRB}-{\rm SFR}$ relation is shown in the left-hand panel of Fig. 4.6. We also show in this plot the data for unresolved galaxies from the high-SFR sample. The latter, however were not used for the fits because of the contribution of unresolved emisison, as discussed in section 2.3. A least-squares fit to the data with the relation $\log L_{\rm X} = \log K + \beta \log {\rm SFR}$ yielded a value of slope consistent with unity: $\beta = 1.01 \pm 0.11$. We therefore fixed the slope at the unity and repeated the fit to obtain the best-fitting linear relation:

$$L^{\rm XRB}_{0.5-8\,{\rm keV}}({\rm erg\,s^{-1}}) = 2.5 \times 10^{39}\,{\rm SFR}\,(M_\odot\,{\rm yr^{-1}}) \tag{4.9}$$

The dispersion around this relation is $\sigma = 0.44$ dex.

To facilitate comparison with previous results, we also studied the $L_{\rm X} - L_{\rm IR}$ relation (right-hand panel of Fig. 4.6). The linear fit of this relation gives the following result:

$$L^{\rm XRB}_{0.5-8\,{\rm keV}}({\rm erg\,s^{-1}}) = 1.75 \times 10^{-4}\,L_{\rm IR}\,({\rm erg\,s^{-1}}) \tag{4.10}$$

where $L_{\rm IR}$ is the total $(8-1000\,\mu{\rm m})$ infrared luminosity. The dispersion around the best-fit is $\sigma = 0.54$ dex, i.e. notably worse than for the $L_{\rm X} - {\rm SFR}$ relation with SFR based on combined UV+IR data.

4.3.1 Unresolved galaxies

As it is obvious from Fig.4.6, unresolved galaxies are distributed along the extension of the $L_{\rm X} - {\rm SFR}$ relation for resolved galaxies, albeit somewhat higher. Quantitatively, a linear fit to the $L_{\rm X} - {\rm SFR}$ relation using unresolved galaxies only yielded the scale factor of $\approx 3.7 \times 10^{39}$ erg/s/(M$_\odot$/yr), i.e. by a factor of ~ 1.5 higher than in eq.(4.9). This result is to be expected because the luminosities of unresolved galaxies, by definition, include the unresolved emission component, which is excluded in the case of the galaxies from our main sample. Although the detailed study of unresolved emission will be fully addressed Chapter 6 we made a preliminary estimate of its amplitude in several galaxies from the primary sample, uniformly distributed along the SFR axis. We found that unresolved emission contributes $\sim 20-60\%$ to the total X-ray luminosity of these galaxies. This is consistent with the higher normalization in the scaling relation for unresolved galaxies, obtained above.

4.3.2 Comparison with previous studies

To do the comparison, we converted the results of the earlier studies to the 0.5–8 keV band assuming an absorbed power law with $\Gamma = 2.0$ and $n_H = 3 \times 10^{21}$ cm^{-2}.

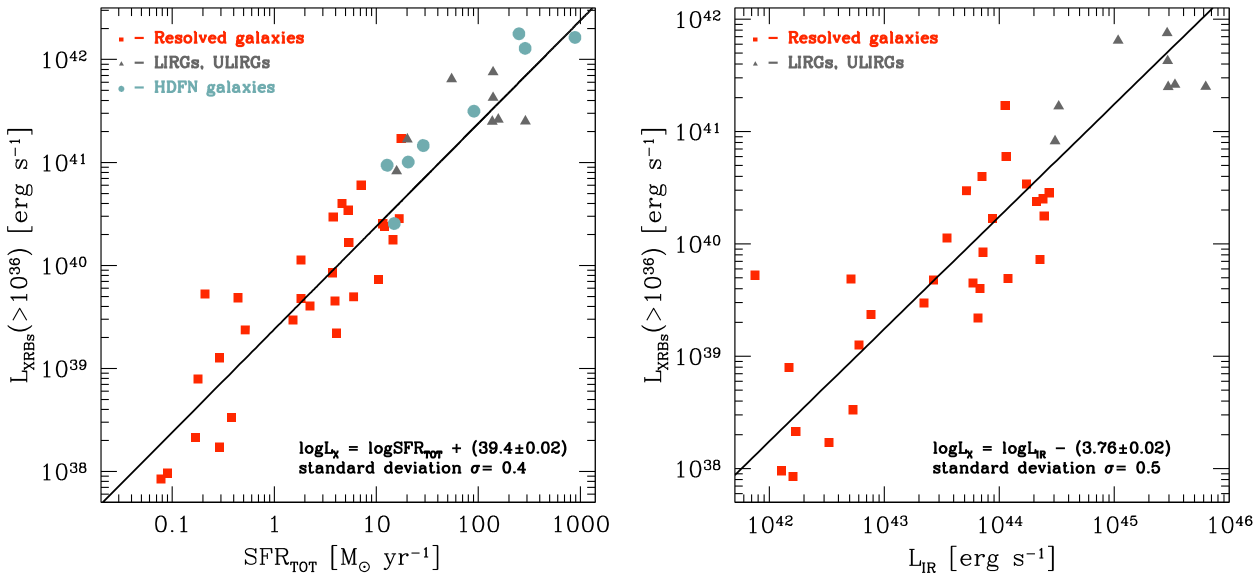

Figure 4.6: The $L_{\mathrm{X}} - \mathrm{SFR}$ (*left*) and $L_{\mathrm{X}} - L_{\mathrm{IR}}$ (*right*) relations. In both panels the squares are galaxies from the resolved sample, the triangles and filled circles are galaxies from the unresolved high-SFR sample. The solid lines show the best-fitting scaling relations, obtained using only resolved galaxies and given by eqs. (4.9) and (4.10) respectively.

The first systematic studies of the $L_{\mathrm{X}} - \mathrm{SFR}$ scaling relations based on the data of modern X-ray satellites were performed by Ranalli, Comastri, & Setti (2003) and Grimm, Gilfanov, & Sunyaev (2003). Ranalli, Comastri, & Setti (2003) obtained tight correlation between X-ray, radio and FIR luminosities for a sample of nearby galaxies using X-ray data from ASCA and BeppoSAX satellites. Using their eqs (8) and (12), converting X-ray luminosities from 0.5–10.0 to 0.5–8.0 keV band (a factor of 1.11) and FIR ($42.5 - 122.5\,\mu$m) luminosity to total IR ($8 - 1000\,\mu$m) band using a conversion factor of 1.7, we obtain the relation $L_{0.5-8\,\mathrm{keV}} \approx 2.4 \cdot 10^{-4} \times L_{\mathrm{IR}}$. The scale factor in this relation is by ≈ 1.36 larger than in eq.(4.10), which is consistent with the fact that Ranalli, Comastri, & Setti (2003) analyzed the total luminosities of galaxies, including unresolved emission. We conclude that their $L_X - L_{IR}$ relation is consistent with the one derived in this paper.

To derive $L_X - SFR$ relation we use their eqs.(14) and (15) and obtain $L_{0.5-8\,\mathrm{keV}} \approx 8.6 \cdot 10^{39} \times \mathrm{SFR}(>5M_\odot)$ where $\mathrm{SFR}(>5M_\odot)$ is the formation rate of massive stars. For Salpeter IMF $\mathrm{SFR}(0.1 - 100M_\odot) = 5.5 \cdot \mathrm{SFR}(>5M_\odot)$, we thus obtain $L_{0.5-8\,\mathrm{keV}} \approx 1.6 \cdot 10^{39} \times \mathrm{SFR}(0.1 - 100M_\odot)$. This is close but not identical to the relation derived in the present paper, eq.(4.9), especially considering that it applies to the total X-ray luminosity of the galaxy, not only bright X-ray binaries. As the underlying scaling relations between X-ray and IR luminosities are fully consistent with our results, the factor of $\sim 2 - 2.5$ discrepancy in the $L_{\mathrm{X}} - \mathrm{SFR}$ relation must be due the different method of the

SFR estimation used in the two studies.

Grimm, Gilfanov, & Sunyaev (2003) used *Chandra* observations of nearby (i.e. spatially resolved) star-forming galaxies and derived a relation between luminosity of compact sources and SFR. Using their eq.(21) and converting the luminosity to 0.5–8 keV band (conversion factor of 1.28) we obtain: $L_{0.5-8\,\mathrm{keV}} \approx 8.5 \cdot 10^{39} \times \mathrm{SFR}(M > 5M_\odot)$, i.e. identical to that obtained by Ranalli, Comastri, & Setti (2003). Shtykovskiy & Gilfanov (2005) recomputed the scale in this relation with account for the updated calibration of IR and radio SFR indicators (Bell, 2003). Using their scale factor we derive $L_{0.5-8\,\mathrm{keV}} \approx 2.8 \cdot 10^{39} \times \mathrm{SFR}(0.1 - 100M_\odot)$, in good agreement with eq.(4.9).

As a historical note we mention that the SFR values determined from the IR-based calibration used by Ranalli, Comastri, & Setti (2003) and Grimm, Gilfanov, & Sunyaev (2003) were incorrectly attributed by the authors to the formation rate of massive stars. This was a result of some confusion that existed in the SFR determination-realted literature at the time of those publications and, in particular, by inconsistent definitions of radio- and IR-based SFR proxies. This error could potentially result in a factor of ~ 5.5 overestimate of the scale in the $L_\mathrm{X} - \mathrm{SFR}$ relation. However, it was compensated by the usage of FIR instead of total IR luminosity in the Kennicutt (1998) relation and the scale factors somewhat different from the presently accepted values. As a result, the final $L_\mathrm{X} - \mathrm{SFR}$ relations derived by these authors are in a reasonable agreement with the scaling relations obtained in this paper.

Among more recent publications on this subject, we compare with the results of Persic & Rephaeli (2007), who investigated the relation between the collective hard X-ray luminosity of young point sources and the SFR derived from infrared luminosity. Using their eq.(9) and converting the 2–10 keV luminosity to the 0.5–8 keV band (a factor of 1.28) we obtain: $L_{0.5-8\,\mathrm{keV}} \approx 0.96 \cdot 10^{39} \times \mathrm{SFR}(0.1 - 100M_\odot)$. This scale factor is significantly, by a factor of $\sim 2 - 2.5$ lower than derived in all other studies, including this one. The reason for this discrepancy is, in our opinion, in an overestimated contribution of the old population to the X-ray emission of star-forming galaxies.

4.3.3 Effects of statistics of small numbers in the $L_\mathrm{X} - \mathrm{SFR}$ relation

For the power law luminosity function with a slope of 1.6, the $L_\mathrm{X} - \mathrm{SFR}$ relation is expected to be non-linear in its low-SFR part, due to the effects of statistics of small numbers (Gilfanov, Grimm, & Sunyaev 2004a, 2004b). These effects are important when considering the collective luminosity of a population of discrete sources and are a consequence of an asymmetric probability distribution for the sum of luminosities of compact sources in the limit of their small number. In the case of HMXBs in star-forming galaxies, they make the $L_\mathrm{X} - \mathrm{SFR}$ relation to appear non-linear in the low SFR limit. This effect is purely statistical in its nature, in the sense that it affects the most likely value of the luminosity of a randomly chosen galaxy, whereas the relation between average luminosity of many galaxies and SFR is linear in the entire range of star-formation rates. This is achieved due to extended tail of the probability distribution $p(L_{tot})$ towards large L_{tot}. In the sample of galaxies from Gilfanov, Grimm, & Sunyaev (2004a, 2004b) such a non-linear dependence was clearly observed at SFR $\lesssim 5\ M_\odot$/yr.

Despite nearly identical XLF of compact sources obtained in this paper, the $L_{\rm X} - {\rm SFR}$ relation appears to be linear in the entire SFR regime. In an attempt to find the reason of such behavior, we investigated the distribution of the luminosity of the brightest source in a galaxy and found that for a fraction of low-SFR galaxies it is higher than predicted based on the average XLF (the predicted value computed according to formulae from Gilfanov, Grimm, & Sunyaev (2004)). As XLF slopes of low-SFR galaxies are consistent with the rest of the sample (Fig.4.5) and the contribution of background AGN is negligible in the bright end of the XLF, we conclude that this may be a consequence of the bias, introduced by selection of galaxies – targets for Chandra observations. For example, the proposers may have predominantly selected galaxies which were known to have enhanced level of X-ray emission, e.g. based on the ROSAT all-sky survey. This issue will be investigated in more detail in a follow-up publication.

4.3.4 Dispersion in the $L_{\rm XRB} - {\rm SFR}$ relation

Despite of the special effort to produce a sample with a homogeneous set of multi-wavelength measurements and to minimize contamination by CXB sources and LMXBs, the resulting $L_{\rm XRB} - {\rm SFR}$ relation bears a rather large dispersion of ~ 0.4 dex rms. In order to investigate the origin of this dispersion we searched for correlation of the $L_{\rm XRB}/{\rm SFR}$ ratio with different quantities characterizing importance of various potential contaminating factors (a first attempt of this study was done by Mineo, Gilfanov, & Sunyaev, 2011). These included the sensitivity limit of *Chandra* data $L_{\rm lim}$, contribution of CXB and LMXB sources characterized by the ratio of the solid angle of the studied region and enclosed stellar mass to the SFR, dust attenuation characterized by the $L_{\rm IR}/L_{\rm UV}$ ratio and inclination of the galaxy i. The results are shown in Fig. 4.7.

We analyzed these data using the Spearman's rank correlation test and found no statistically significant correlations. The results of these tests are presented below with r_S being the correlation coefficient and P being the probability under the null hypothesis that the variables are unrelated. We found no correlation with the point source detection sensitivity ($r_S = 0.32$, $P = 10\%$). Therefore we can exclude that the extrapolation of X-ray luminosity above 10^{36} erg/s is the main reason for the dispersion around the $L_{\rm XRB} - {\rm SFR}$ relation. There is no evidence for strong contamination by CXB sources ($r_S = -0.17, P = 30\%$) or LMXBs ($r_S = 0.05, P = 78\%$). This proofs that the spatial analysis, performed in order to minimize the contribution of CXB and LMXB sources to the compact source population, yielded sensible results. It is further confirmed by repeating the previous test on the data without CXB subtraction: $r_S = -0.11, P = 52\%$. We used the ratio of IR to NUV luminosity $L_{\rm IR}/L_{\rm NUV}$ to characterize the dust attenuation (higher the ratio, higher the absorption) and found virtually no correlation ($r_S = -0.33, P = 10\%$). Neither $L_{\rm X}/{\rm SFR}$ correlates with the inclinations of galaxies ($r_S = 0.12, P = 56\%$). To verify this approach, we analyzed the dependence between $L_{\rm IR}/L_{\rm NUV}$ ratio and inclination of the galaxy and

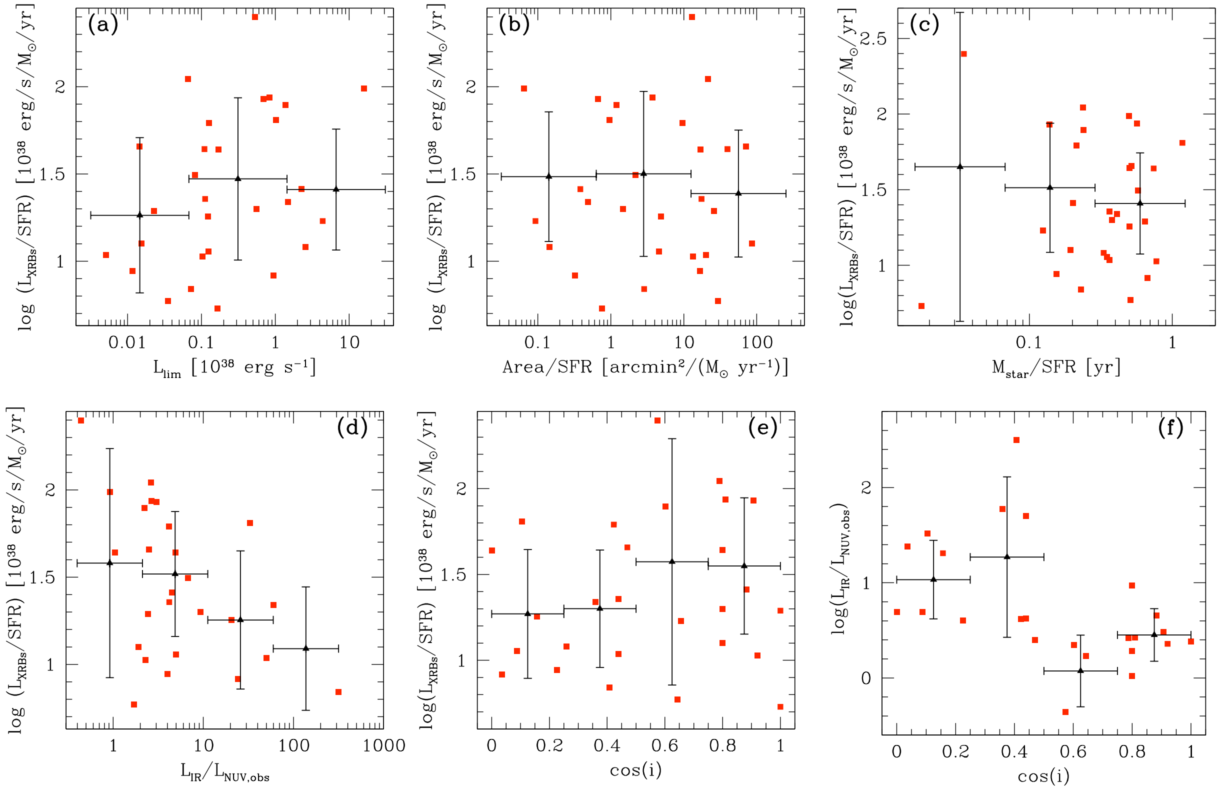

Figure 4.7: Dependence of the log(L_X/SFR) on quantities characterizing different potentially contaminating factors: the point source detection sensitivity of Chandra observations (a), the fractional contribution of CXB sources (b) and LMXBs (c), the dust attenuation characterized by L_{IR}/L_{NUV} ratio (d) and the inclination of the galaxy. The last panel (e) shows the relation between the dust attenuation and inclination. Each point represents a galaxy from the primary sample. The crosses show average values in bins; the bin extent is indicated by the horizontal error bar, the vertical error bar shows the rms of points with respect to the average value. The contribution of CXB sources is subtracted. See Sect 4.3.4 for details.

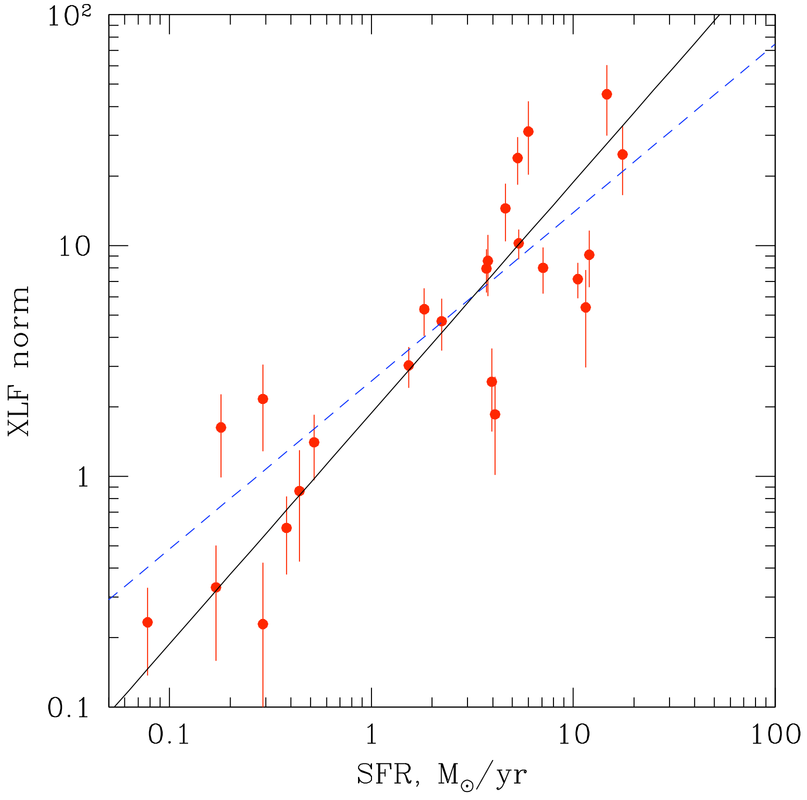

Figure 4.8: The XLF normalization versus SFR. The solid line shows the best-fit linear relation, dashed line - the best fit relation in the form $A = \xi \times \mathrm{SFR}^{\beta}$. See text for details.

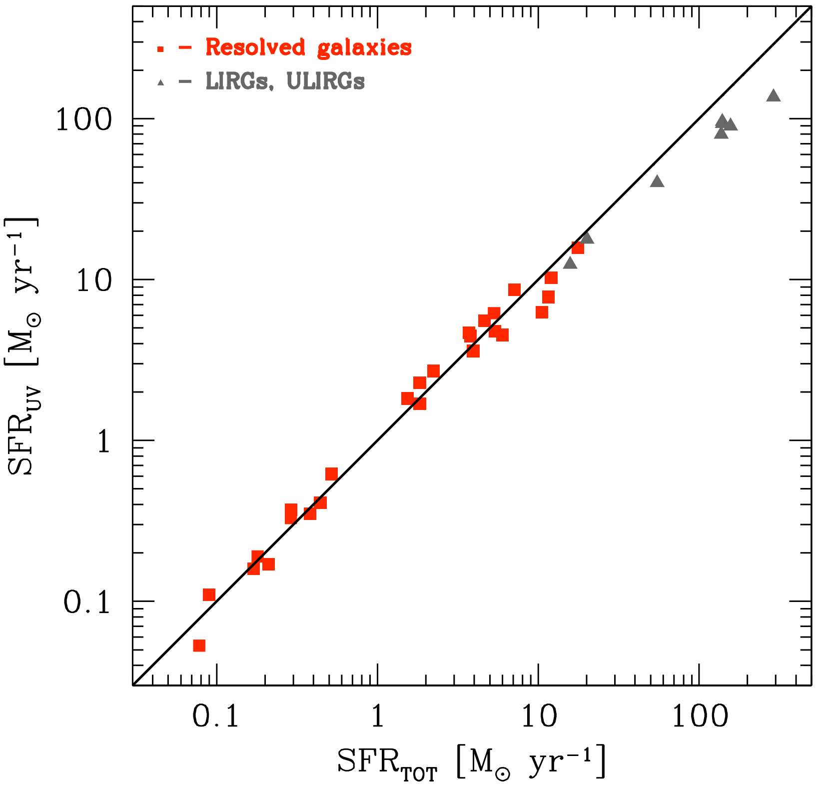

Figure 4.9: Comparison of the SFR estimations obtained by different methods. The x-axis is the SFR used in the paper, computed as described in Section 3.7. The y-axis values are computed from the UV luminosity corrected for the dust attenuation using the method of Buat et al. (2005). The straight line is $y = x$ relations. The dispersion of points around this relation is $rms = 0.12$.

found a strong anticorrelation ($r_S = -0.59, P = 0.2\%$), as expected. We note that in order to suppress the $0.5-8$ keV luminosity by a factor of 10 a large column density of $\sim 5\times10^{23}$ cm^{-2} is needed.

We also tried to probe the amplitude of intrinsic uncertainties of the SFR determination. To this end we computed the UV based SFR estimates corrected for the attenuation effects following the method of Buat et al. (2005), and compared with the SFR values used in this paper (Fig.4.9). We found a good consistency between the SFR estimations obtained by the two methods with $rms = 0.12$ dex, i.e. three times smaller than the rms of the $L_X - SFR$ relation. This suggests that uncertainties of the SFR determination are not the main source of the scatter in the $L_{\rm X}$ – SFR relation.

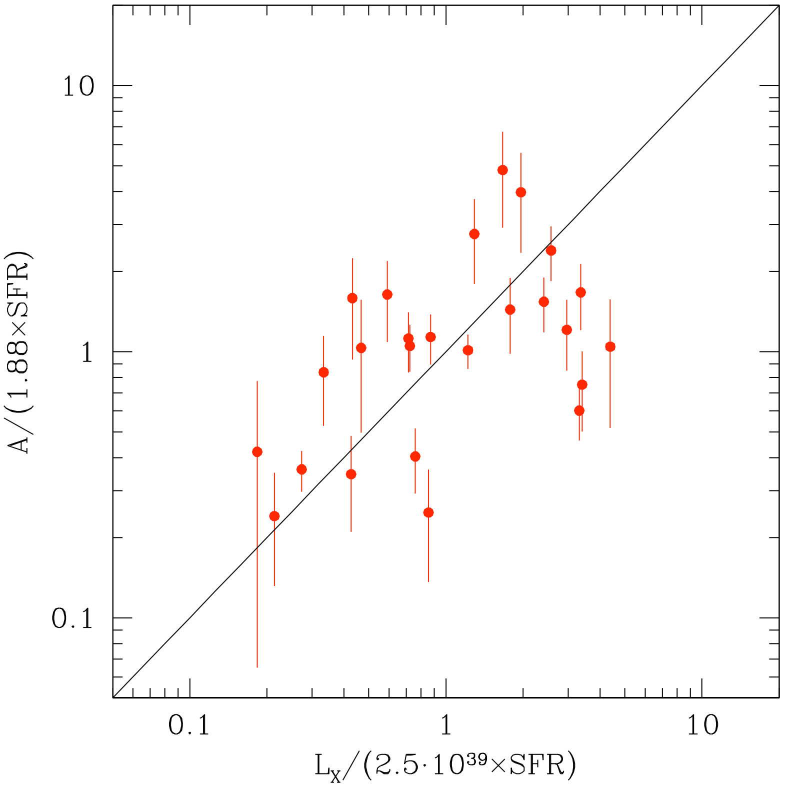

Figure 4.10: The XLF normalization vs. total luminosity of X-ray binaries. Both quantities are normalized to the SFR with the normalization coefficients equal to the best fit values in the corresponding scaling relations. Only galaxies having ≥ 5 sources above their threshold luminosities are shown. This plot illustrates the lack of one-to-one correspondence between the deviations from the average dependence in the number of sources and in the total luminosity.

4.4 Discussion

We have found rather large scatter around the average $L_{\rm X}-{\rm SFR}$ relation $rms \approx 0.4$ dex (Fig.4.6). As discussed in the Section 4.3.4 the scatter is unlikely to be caused by any of the obvious contaminating factors, such as difference in the sensitivity limits of observations of different galaxies, pollution by CXB sources or LMXBs. This proofs that the criteria used for selecting the sample and the method for choosing the regions for the analysis yielded the desired result. On the other hand it suggests that the observed scatter has physical origin.

Although similar scatter is found in the SFR-dependence of the XLF normalization, $rms \approx 0.34$ dex (Fig.4.8), there is no precise one-to-one correspondence between the deviations of these two quantities from their best fit relations, as illustrated by Fig.4.10. At the same time the XLF slopes appear to be consistent, within statistical errors, with all having the same (or close) value (Fig.4.5, 4.11). These two facts do not contradict to each other. Indeed, for a power law with $\gamma = 1.6$ the XLF normalization and, largely, its slope are determined by the more numerous faint sources, whereas the total luminosity is determined by the (often few) brightest sources in the galaxy. Thus, we conclude that the scatter in the $L_{\rm X}-{\rm SFR}$ relation is caused by both variations in the XLF normalization and fluctuations in the number and luminosity of brightest sources in the galaxy (cf. Fig.4.11), the variations of the XLF slopes playing less significant role.

Metallicity is one of the primary quantities that may affect the population of HMXBs, as it exerts an equally great effect on HMXB creation and emission. Star formation at lower metallicity is expected to produce more massive stars as a result of the low cooling rate. This effect would result in a higher number of compact objects in binary systems. This simple theoretical argument is supported by the recently found evidence that the number of ultra-luminous X-ray sources is inversely proportional to the metallicity of their host galaxy (Zampieri & Roberts, 2009; Mapelli et al., 2010). Metallicity has also a rather substantial impact on the strength of stellar winds, thus on the luminosity of individual HMXBs, making it larger for larger amount of metals present in the companion star. Apart from these, rather obvious and general, remarks, no more specific predictions regarding the overall effect of metallicity on the population of HMXBs and their total luminosity are currently available. In attempt to advance this issue observationally, we collected from the literature a rather heterogeneous set of the metallicity measurements for a relatively small subset of galaxies, but could not find any meaningful trends in the data. This, however, should not be considered as an ultimate result, more systematic studies are obviously needed in order to make a reliable conclusion regarding the role of metallicity (work in progress).

Another important factor is the recent star-formation history of the host galaxy. Indeed, as more massive stars have shorter life times, and, on the other hand, have stronger winds one may expect that the very luminous HMXBs are short-lived. This effect may result in the dependence of the X-ray luminosity of the galaxy on the recent star-formation activity, which is not characterized precisely the SFR value determined from the IR and/or UV data, thus introducing scatter in the $L_{\rm X}-{\rm SFR}$ relation.

In addition to the more fundamental reasons discussed above, variability of the brightest X-ray sources may also contribute to the scatter in the $L_{\rm X} - {\rm SFR}$ relation. The X-ray sources with $\log L_{\rm X} \gtrsim 39$ (usually classified as ultra-luminous X-ray sources) likely harbor a black hole and may be subject to the disk instability resulting in transient events characterized by luminosity variations of several orders of magnitude. In addition, spectral state changes may lead to the luminosity changes from the factor of a few upto ∼order of magnitude. Their effect on the total luminosity will be especially important in galaxies with ${\rm SFR} \lesssim 10$ $\mathrm{M_\odot/yr}$, containing only a few such bright sources (Gilfanov, Grimm, & Sunyaev, 2004).

4.5 XLF of high-mass X-ray binaries and ULXs.

Based on a sample of ~ 700 compact sources, we have produced the average luminosity distribution of HMXBs in galaxies (Fig.4.2). This is a significant improvement in the statistical accuracy as compared with the previous result of Grimm, Gilfanov, & Sunyaev (2003). We have also improved in terms of the errors introduced by the distance uncertainties, thanks to the systematic compilation of distances for galaxies which became available in the NED. Thirdly, we made a special effort to minimize and accurately subtract the contribution of background AGN. Although we could not in the same way remove the contribution of LMXBs, because of the strong age dependence of the LMXB–stellar mass scaling relations, the method of construction makes us confident that our sample is relatively free from the LMXB contamination. This is definitely true in the high luminosity end, $\log L_{\rm X} \gtrsim 38.5 - 39$.

Despite all these improvements our average HMXB XLF is entirely consistent with the one obtained by Grimm, Gilfanov, & Sunyaev (2003). Indeed, the values of slope agree to the accuracy of ~ 0.03 and the values of the high luminosity break are consistent within (admittedly rather large) statistical uncertainties.

Similar to Grimm, Gilfanov, & Sunyaev (2003), we did not find any statistically significant features in the XLF near the critical Eddington luminosity of a neutron star or a stellar mass black hole. The XLF follows a single slope power in the entire luminosity range, upto $\log L_{\rm X} \sim 40$, where it breaks. Taken at the face value, the break corresponds to the Eddington luminosity of a $\sim 50 - 100$ $\mathrm{M_\odot}$ black hole. We note that the statistical accuracy of the XLF, grouped into broad, $\Delta \log L \sim 0.5$, luminosity bins, is $\lesssim 13\%$ and $\lesssim 22\%$ in the $\log L_{\rm X} \sim 38 - 39$ and $\log L_{\rm X} \sim 39 - 40$ luminosity ranges (Fig.4.4). This further strengthens the proposition of Grimm, Gilfanov, & Sunyaev (2003) that the bulk of the population of what is called the ultra-luminous X-ray sources (conventionally defined as sources with $\log L_{\rm X} \gtrsim 39$) are a high luminosity end of the population of the ordinary HMXBs and most likely harbor stellar mass black holes rather than exotic intermediate mass objects. The very high luminosity end of the distribution, $\log L_{\rm X} \gtrsim 40$, may, however, be associated with the intermediate mass black holes.

The absence of features in the luminosity function of HMXBs is still puzzling. The inaccuracies in distances to the galaxies in our sample may still contribute to smearing of

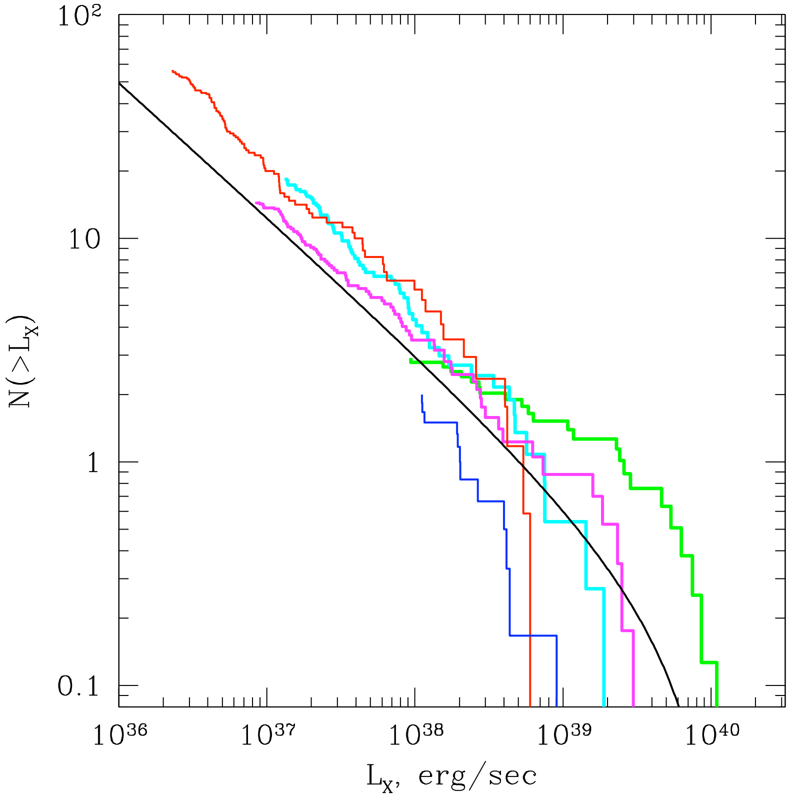

Figure 4.11: Several representative XLFs, normalized to the SFR. In the order of increasing luminosity of the brightest sources: M101, NGC3079, M51, Antennae, NGC3310. The solid line shows a power law with average normalization of $A = 1.88$, slope $\gamma = 1.6$ and a cut-off at $L_{\rm cut} = 10^{40}$ erg/s. The XLFs of NGC3079 and NGC 3310 are, correspondingly, the steepest and the flattest in the sample.

the break at the NS Eddington limit, but their role must be significantly smaller than in the XLF of Grimm, Gilfanov, & Sunyaev (2003).Taken at the face value, this result may suggest that there is no sharp limit on the luminosity of an accreting compact object at the Eddington value, as discussed, for example, by Grimm, Gilfanov, & Sunyaev (2002, 2003). This does not explain, however, why the nearly an order of magnitude difference in the specific frequencies of neutron stars and black holes does not reveal itself in the XLF. Indeed, in the entire luminosity range the XLF slope is consistent with the slope of the distribution of the mass transfer rates in HMXBs, predicted from the standard Salpeter IMF for massive stars (Postnov, 2003).

Answers to these questions could be obtained if one could disentangle the contributions of NS and BH binaries and separate their XLFs. Direct measurements of the mass of the compact object in a large number of binaries in external galaxies is not feasible. Therefore indirect methods will have to be utilized, for example based on the X-ray spectral properties of the binaries. An example of a successful application of one of such methods, based on the X-ray colors, was proposed recently by Farrell et al (in preparation).

Chapter 5

Implications for the theory of binary evolution

5.1 Specific frequency of X-ray bright compact objects in HMXBs

With the knowledge of the relation between the number of HMXBs and SFR, we can estimate the fraction of compact objects that went through an X-ray active phase powered by accretion of matter from a massive donor star in a binary system.

According to eq. (4.5), the number of HMXBs with luminosity higher than 10^{35} erg/s is:

$$N_{\rm HMXB}(>10^{35}{\rm erg\,s^{-1}}) \approx 135 \times {\rm SFR} \tag{5.1}$$

On the other hand, the number of HMXBs at any given time is:

$$N_{\rm HMXB} \sim \dot{N}_{co} \sum_k f_{{\rm X},k}\, \tau_{{\rm X},k} \sim \dot{N}_{co}\, f_{\rm X}\, \bar{\tau}_{\rm X} \tag{5.2}$$

where $\dot{N}_{co} \approx \dot{N}_\star(M > 8\,M_\odot)$ is the birth rate of compact objects (both NS and BH), approximately equal to the birth rate of massive stars $\dot{N}_\star(M > 8\,M_\odot)$. For a Salpeter IMF, we obtain:

$$\dot{N}_*(M > 8\,M_\odot) \approx 7.4 \cdot 10^{-3} \times {\rm SFR} \tag{5.3}$$

The summation in eq.(5.2) is done over different types of HMXBs (wind-fed and Roche lobe overflow systems with a supergiant companion, Be/X binaries etc), $f_{{\rm X},k}$ is the fraction of compact objects (computed with respect to their total number in the galaxy) which become X-ray sources due to accretion in HMXBs of the $k-$type, $\tau_{{\rm X},k}$ is the duration of their X-ray active phase. The $f_{\rm X} = \sum_k f_{{\rm X},k}$ is the total fraction of X-ray bright compact objects and $\bar{\tau}_{\rm X}$ is the average life time of X-ray sources:

$$\bar{\tau}_{\rm X} = \frac{\sum_k f_{{\rm X},k}\tau_{{\rm X},k}}{\sum_k f_{{\rm X},k}} \tag{5.4}$$

From binary evolution calculations, $\tau_{\rm X} \sim 10^4\,$yr for supergiant systems and $\tau_{\rm X} \sim 10^5\,$yr for Be/X binaries. Majority of known high-mass X-ray binaries are Be/X systems, especially in Magellanic Clouds, where only a few supergiant systems are known (Liu, van Paradijs, & van den Heuvel, 2006). The fraction of the latter is larger in the Milky Way, where about 29 out of 114 HMXBs (are suspected to) have supergiant donors. If these proportions are representative for star-forming galaxies in general, the summation in eq.(5.2) and (5.4) is dominated by Be/X systems and appropriate scaling for $\bar{\tau}_{\rm X}$ should be $\sim 10^5$ yrs.

Combining equations 5.1, 5.2 and 5.3, we obtain:

$$f_{\rm X} \sim 0.18 \times \left(\frac{\bar{\tau}_{\rm X}}{0.1\,{\rm Myr}}\right)^{-1} \tag{5.5}$$

This quantity represents the fraction of compact objects that on the time scale of $\sim 10^2$ Myrs after their formation (e.g. Shtykovskiy & Gilfanov, 2007) become X-ray sources with $L_{\rm X} > 10^{35}$ erg/s, powered by accretion from a massive donor star in a high-mass X-ray binary.

It is interesting to note, that if the HMXB XLF continues towards lower luminosities with $\sim$ same or similar slope, it may be possible to constrain $\bar{\tau}_{\rm X}$ based on the specific frequency of X-ray sources in star-forming galaxies. Indeed, if XLF from eq.(4.5) can be extrapolated down to $L_{\rm X} \sim 10^{34}$ erg/s, as suggested by Shtykovskiy & Gilfanov (2005), the coefficient in eq.(5.5) becomes 0.72. As $f_{\rm X}$ can not exceed the binary fraction $f_{bin} \sim 0.5$, the X-ray life-time of Be/X systems is $\bar{\tau}_{\rm X} \lesssim 0.07\,(f_{bin}/0.5)$ Myrs.

5.2 Bright sources – Black hole systems

The derivation of eq.(5.5) assumed that $f_{\rm X}$ and $\bar{\tau}_X$ do not depend on the mass of the compact object which assumption is likely to be incorrect. However, as we used a rather low luminosity limit of 10^{35} erg/s in eq.(5.1), the $N_{\rm HMXB}$ is dominated by faint Be/X binaries, which harbor neutron stars. Therefore the $f_{\rm X}$ derived above characterizes neutron stars and is likely to be insensitive to the contribution of black holes. As contributions of BH and NS systems to the $N_{\rm HMXB}$ in eq.(5.1) can not be separated, we can not estimate $f_{\rm X}$ for BH binaries of all luminosities separately. However, this can be done for bright sources, with luminosity significantly exceeding the Eddington limit for the neutron star. Using 10^{39} erg/s as the luminosity limit, we obtain:

$$N_{\rm HMXB}(>10^{39}{\rm erg\,s^{-1}}) \approx 0.49 \times {\rm SFR} \tag{5.6}$$

As we consider luminous sources, the $\dot{N}_{co}$ in eq.(5.2) is now the birth rate of black holes, which for Salpeter IMF is:

$$\dot{N}_*(M > 25\,M_\odot) \approx 1.4 \cdot 10^{-3} \times {\rm SFR} \tag{5.7}$$

The resulting fraction of stellar-mass BH that became luminous X-ray sources in HMXB is:

$$f_{\rm X}^{bright} \sim 3.5 \cdot 10^{-2} \times \left(\frac{\tau_{\rm HMXB}}{10^4\,{\rm yr}} \right)^{-1} \tag{5.8}$$

In the latter equation we took into account that bright HMXBs shining near the Eddington limit typically contain supergiant donors, therefore their characteristic life times are shorter than for Be/X systems and are $\sim 10^4$ yrs.

Finally we note that in the estimates in sections 5.1 and 5.2 we intentionally used Salpeter mass function rather than a more realistic IMF. Indeed, the UV and IR SFR proxies used in this paper rely on the emission from massive, $M \gtrsim 5 M_\odot$, stars. The star-formation rates derived by these proxies are then converted to the full $0.1 - 100 M\odot$ range assuming Salpeter IMF (e.g. Kennicutt, 1998). Therefore, for the sake of consistency, same IMF should be used in the estimates of the numbers of compact objects in eq.(5.3) and (5.8). In the remaining part of this section a more correct approach is to use a realistic IMF, correctly predicting the frequencies of low mass stars, e.g. the one suggested by (Kroupa, 2002).

5.3 Specific frequency of X-ray bright compact objects in LMXBs

For comparison, we obtain a similar estimate for the fraction of compact objects that become X-ray sources powered by accretion from a low-mass donor star in an LMXB. According to Gilfanov (2004), the number of LMXBs with luminosity higher than 10^{35} erg/s is:

$$N_{\rm LMXB}(> 10^{35} {\rm erg\,s^{-1}}) \approx 50 \times M_*/(10^{10} M_\odot) \tag{5.9}$$

Assuming stationarity:

$$N_{\rm LMXB} \sim N_{co}\, f_{\rm X} \tag{5.10}$$

Strictly speaking, stationarity assumption does not apply to bright LMXBs. Indeed, the life time of a source with $L_{\rm X} = 10^{38}$ erg/s ($\dot{M} \sim 10^{-8}$ $\rm M_\odot$/yr) powered by accretion from a ~ 1 $\rm M_\odot$ star can not exceed $\sim 10^8$ yrs. However, as in the case of HMXBs, the $N_{\rm LMXB}$ in eq.(5.9) is dominated by faint sources, for which the stationarity assumption may apply. Assuming a Kroupa IMF (slope of $\gamma = 1.3$ for $M < 0.5 M_\odot$, $\gamma = 2.3$ for $0.5 < M < 1 M_\odot$ and $\gamma = 2.7$ for $M > 1 M_\odot$ (Kroupa, 2002)), the number of neutron stars and black holes in such a galaxy would be:

$$N_{co} \approx N_*(M > 8\, M_\odot) \approx 5 \cdot 10^{-3} \times M_* \tag{5.11}$$

Combining eqs. (5.9)-(5.11) we obtain:

$$f_{\rm X} \sim 10^{-6} \tag{5.12}$$

According to the derivation, this number takes into account only LMXBs in bright state and ignores compact objects in transient systems which are in the quiescent state.

It is interesting to note that the $f_{\rm X}$ for LMXBs is by ~ 5 orders of magnitude smaller than for HMXBs. This is another manifestation of the fact that LMXBs are extremely rare objects and may be explained by the high probability of disruption of the binary system with a low mass companion in the course of the supernova explosion (Lewin, van Paradijs, & van den Heuvel, 1997).

5.4 Constrains on the mass-ratio distribution in binaries

As not every compact object is in a binary and not every compact object in a binary has a suitable combination of binary parameters to become an HMXB, f_X derived in section 5.1 obeys the condition:

$$f_{\rm X} \leq f_{bin}(m_2 \gtrsim 5M_\odot) \tag{5.13}$$

where $f_{bin}(m_2 \gtrsim 5M_\odot)$ is the fraction of binaries with compact object, having a massive companion. This inequality can be used obtain interesting constrains on the mass distribution of the secondary in massive binaries.

Firstly, we can exclude the possibility that the mass of the secondary in a binary system obeys a Kroupa mass function. Indeed, for Kroupa MF, the fraction of stars more massive than $5M_\odot$ is $f(m > 5M_\odot) \approx 5.5 \cdot 10^{-3}$ by number, i.e. is by a factor of ~ 30 to ~ 100 smaller than $f_{\rm X}$, in a strong contradiction to eq.(5.13). Considering a more general power law mass distribution $\psi(m) \propto m^{-\gamma}$, and assuming $f_{\rm X} = 0.2$ we obtain from eq.(5.13) a constrain $\gamma < 0.3$, i.e. much flatter than the high mass end of Kroupa or Salpeter mass function.

If the mass transfer in the course of the binary evolution does not significantly change the mass of the secondary, the above result strongly excludes the possibility that the masses of stars in a massive binary are drawn independently from the IMF. Assuming further that number of binaries obeys the distribution in the form

$$dN \propto \psi(m_1)dm_1\, f(q)dq \tag{5.14}$$

where m_1 is the mass of the primary, with the mass distribution $\psi(m_1)$ and $f(q)$ is the distribution of the mass ratio $q = m_2/m_1$, we write for the fraction of system with the secondary mass $m_2 > 5M_\odot$ among all binaries with the primary mass $m_1 > 8M_\odot$ (i.e. those producing a compact object):

$$f_{bin}(m_2 \gtrsim 5M_\odot) = \frac{\int_8^{100} dm_1 \psi(m_1) \int_{5/m_1}^{1} f(q)dq}{\int_{0.1}^{100} \psi(m)dm} \tag{5.15}$$

For the Kroupa IMF and $f(q) = 1$ the above equation gives $f_{bin}(m_2 \gtrsim 5M_\odot) \approx 0.6$, i.e. consistent with $f_{\rm X} \sim 0.2$.

Chapter 6

The hot interstellar medium

6.1 Introduction

The diffuse X-ray emitting gas from late-type galaxies exhibit different morphologies. It is observed in the bulges as well as in the galactic discs where it is predominantly associated with the spiral structure. Large-scale outflows arising above the galactic plane are observed in the edge-on spiral galaxies and starbursts. They are thought to be driven by the collective energy from supernovae and winds from young massive stars (e.g. Chevalier & Clegg, 1985; Strickland et al., 2000, 2004; Grimes et al., 2005; Bogdán & Gilfanov, 2008). The X-ray spectra of diffuse hot gas is described by a thermal model with temperature of $kT \sim 0.2$ keV and, very often, by an additional thermal component with temperature of $0.6 - 0.7$ keV ($T \gtrsim 10^6$ K). As the supernovae provide newly synthesized heavy elements to the ISM, the outflows play a major role for understanding the metallicity evolution of galaxies and intergalactic medium (IGM) by propelling large amount of metals out of star-forming galaxies.

Tyler et al. (2004) showed that there is a strong correlation between location of soft diffuse X-ray emission and sites of recent star formation in spiral arms traced by mid-infrared and H_α emission. In particular, diffuse X-ray emission is not detected in the interarm regions. Similar results suggesting the strong link between tracers of star formation and diffuse X-ray emission have been reported in a number of studies of individual late-type galaxies. In this chapter we investigate the relation between luminosity of diffuse emission and star formation activity in late-type galaxies.

6.2 Selecting a sub-sample of galaxies

For the unresolved emission analysis we selected a sub-sample of galaxies requiring that their full extent lies within a single chip of the *Chandra* detector. As the background correction is normally performed on a chip-to-chip basis, the latter criterion allows a straightforward and accurate background level estimation and subtraction, addressing both the instrumental and cosmic X-ray background. We selected and analyzed only single observations having exposure-time longer than 20ks. The star formation rate (SFR) of the selected galaxies spans a similar range as for galaxies of the full sample (from ~ 0.1 to $\sim 20\ M_{\odot}$ yr^{-1}). This will allow to compare the relation of the latter with the collective luminosity of high-mass X-ray binaries and study the total X-ray luminosity relation with the SFR.

6.3 X-ray luminosity of the hot diffuse gas

We studied the unresolved X-ray emission in $0.5-2$ and $0.5-8$ keV bands. We measured the background-subtracted X-ray luminosity of unresolved emission using counts-to-ergs conversion for the best fit model (Sect. 3.5) of each galaxy. From this luminosity we subtracted the contribution of unresolved HMXBs in the same band, which was estimated as explained in Sect. 3.4.4 and obtained the quantity to which we refer as diffuse X-ray luminosity, $L_{\mathrm{X}}^{\mathrm{diff}}$. It consists of the contribution of hot gas and faint unresolved sources, such as young stellar objects and young stars, cataclismic variables and active binaries. Based to the X-ray luminosity function of Sazonov et al. (2006), we concluded that in the soft band the diffuse emission is dominated by the gas contribution, while in the hard band the main contribution is probably due to young faint stellar sources. The X-ray luminosities mentioned above, along with the errors (quoted at 1σ) are listed in Table 6.1.

The obtained $L_{\mathrm{X}}^{\mathrm{diff}}$ − SFR relations for soft and full bands are shown in Fig. 6.1, respectively in the left- and right-hand panel. For both relations, a least-squares fit to the data, using the model $\log L_{\mathrm{X}} = \log K + \beta \log \mathrm{SFR}$, yielded a value of slope different than unity: $\log L_{0.5-8\,\mathrm{keV}}^{\mathrm{diff}} = (38.83 \pm 0.09) + (1.19 \pm 0.11) \log \mathrm{SFR}$ and $\log L_{0.5-2\,\mathrm{keV}}^{\mathrm{diff}} = (38.70 \pm 0.09) + (1.24 \pm 0.11) \log \mathrm{SFR}$ (see Table 6.2 for a summary of the best-fitting parameters obtained). This values were confirmed by performing a χ^2 fit. If we fix the slope at the unity and repeat the least-squares fit to obtain the best-fitting linear relations:

$$L_{0.5-8\,\mathrm{keV}}^{\mathrm{diff}}(\mathrm{erg\,s^{-1}}) = 7.6 \times 10^{38}\,\mathrm{SFR}\,(M_{\odot}\,\mathrm{yr}^{-1}) \tag{6.1}$$

with a dispersion of $\sigma = 0.34$ dex, and:

$$L_{0.5-2\,\mathrm{keV}}^{\mathrm{diff}}(\mathrm{erg\,s^{-1}}) = 5.9 \times 10^{38}\,\mathrm{SFR}\,(M_{\odot}\,\mathrm{yr}^{-1}) \tag{6.2}$$

with a dispersion $\sigma = 0.36$ dex.

According to eqs. (6.1) and (6.2), $\sim 80\%$ of the unresolved X-ray luminosity generated per unit of SFR is emitted in the $0.5-2$ keV band by the hot gas. The $\sim 20\%$ of residual component emitted in the hard band is due to unresolved young stars and YSOs and corresponds to $\sim 3\%$ of the total X-ray luminosity associated with resolved HMXBs. This result is consistent with Bogdan & Gilfanov (2011) who found for a different sample of galaxies $L_{\mathrm{X}}/\mathrm{SFR} = 1.7 \times 18^{38}\,\mathrm{erg\,s^{-1}}(M_{\odot}\,\mathrm{yr}^{-1})^{-1}$ and confirms what is discussed in Sect. 3.5.

The luminosity of the diffuse X-ray emission in star-forming galaxies follow simple scaling relations over ranges of nearly 4 orders of magnitude in both X-ray luminosity and SFR. The best-fit slope of $L_{\mathrm{X}} - \mathrm{SFR}$ relation, $\beta \neq 1$, may suggest a possible non-linearity

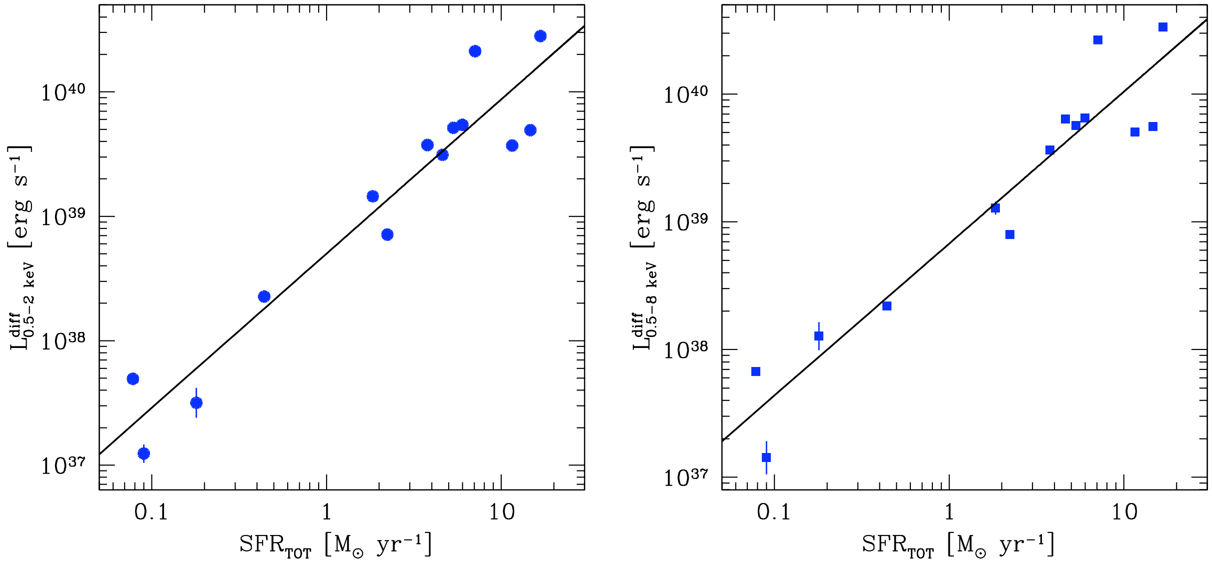

Figure 6.1: The $L_X^{diff} - \text{SFR}$ relation for $0.5 - 8$ keV (*left*) and $0.5 - 2$ keV (*right*) bands. In both panels the solid line shows the best-fitting scaling relation, obtained by setting the slope β free. A fit to the data in $0.5 - 8$ keV band provided $\beta = 1.19 \pm 0.11$, while in $0.5 - 2$ keV band $\beta = 1.24 \pm 0.11$. The error bars on the luminosities are quoted at 1σ.

	SOFT 0.5 − 2 keV		FULL 0.5 − 8 keV			
Galaxy	$\log L_{\rm X}^{\rm diff}$ (erg/s)	$\log L_{\rm HMXB}^{\rm unr}$ (erg/s)	$\log L_{\rm X}^{\rm diff}$ (erg/s)	$\log L_{\rm HMXB}^{\rm unr}$ (erg/s)	$\log L_{\rm HMXB}^{\rm res}$[a] (erg/s)	$\log L_{\rm X}^{\rm tot}$ (erg/s)
NGC 0520	39.57 ± 0.028	38.82	39.71 ± 0.033	39.37	40.40	40.51
NGC 1313	38.35 ± 0.023	37.28	38.34 ± 0.034	37.84	39.69	39.71
NGC 1569	37.69 ± 0.0072	36.28	37.83 ± 0.0074	36.83	37.93	38.20
NGC 2139	39.57 ± 0.024	38.92	39.56 ± 0.032	39.47	40.47	40.56
NGC 3079	39.73 ± 0.013	38.66	39.81 ± 0.013	39.21	39.69	40.12
NGC 3310	40.33 ± 0.0055	38.80	40.43 ± 0.0058	39.35	40.78	40.95
NGC 3556	38.85 ± 0.014	38.14	38.90 ± 0.018	38.69	39.60	39.72
NGC 3631	39.49 ± 0.026	38.98	39.81 ± 0.027	39.53	40.60	40.70
NGC 4194	40.45 ± 0.012	38.87	40.53 ± 0.013	39.43	40.45	40.81
NGC 4625	37.09 ± 0.074	37.18	37.15 ± 0.13	37.74	37.98	38.22
NGC 5474	37.50 ± 0.12	37.61	38.11 ± 0.11	38.17	38.90	39.03
NGC 5775	39.71 ± 0.015	39.01	39.76 ± 0.017	39.56	40.53	40.64
NGC 7541	39.69 ± 0.024	39.14	39.75 ± 0.027	39.69	40.25	40.45
UGC 05720	39.16 ± 0.043	38.57	39.11 ± 0.051	39.13	39.68	39.87

Table 6.1: X-ray luminosities of diffuse emission and contribution of unresolved HMXBs in the $0.5-2$ and $0.5-8$ keV bands.
Note. Errors are quoted at 1σ for one interesting parameter. For details see Sect. 3.5.

of the relations. However, considering the rather high dispersion of points around the best fit relations and the limited number of galaxies of the sub-sample used for the diffuse emission studies, this non-linearity may be caused by the particular sub-sample of galaxies investigated.

6.3.1 Comparison with previous studies

In order to compare our results to the derivations obtained by other authors, we converted the luminosities used in the earlier studies into 0.5–8 keV and 0.5–2 keV bands assuming an absorbed ($n_H = 3 \times 10^{21}$ cm^{-2}) thermal component with $kT = 0.24$ keV and a power law with $\Gamma = 2.0$. Based on XMM-*Newton* observations of a sample of nearby late-type galaxies, Owen & Warwick (2009) found a range of variation of 2.5×10^{38} to $\sim 10^{39}$ $\rm erg\,s^{-1}(M_\odot\,yr^{-1})^{-1}$ for the 0.3–1.0 keV luminosity to SFR ratio. The latter luminosity was defined after excluding the contribution of the most luminous point sources only, therefore it includes the contributions of both hot gas and unresolved HMXBs. Their SFR was measured based on FUV luminosities and corrected for dust attenuation effects. According to Fig. 4.9, for resolved galaxies there is a 1-to-1 relation between the corrected UV-based SFR and the total SFR estimator adopted in the present work. Therefore in order to com-

---

[a] this quantity is equal to $\log L_{\rm XRB}$ in Table 2.1. A different notation was used to distinguish it from $\log L_{\rm HMXB}^{\rm unr}$.

		FREE SLOPE			LINEAR FIT	
Calibrations	Band (keV)	$\log K$	β	σ (dex)	$\log K$	σ (dex)
$L_{\rm XRB}-$ SFR	$0.5-8$	39.41 ± 0.09	1.01 ± 0.11	0.44	39.41 ± 0.02	0.44
$L_{\rm X,diff}-$ SFR	$0.5-8$	38.83 ± 0.09	1.19 ± 0.11	0.32	38.88 ± 0.02	0.34
$L_{\rm X,diff}-$ SFR	$0.5-2$	38.70 ± 0.09	1.24 ± 0.11	0.32	38.77 ± 0.03	0.36
$L_{\rm X,tot}-$ SFR	$0.5-8$	39.63 ± 0.09	1.06 ± 0.11	0.33	39.65 ± 0.02	0.32

Table 6.2: Summary of the parameters for $L_{\rm X}-$SFR relations obtained from least-squares fit.
Note. The parameters are determined from the least-squares fit to the data with the relation $\log L_{\rm X} = \log K + \beta \log {\rm SFR}$, respectively setting the slope β free and fixing it to unity. σ is the standard deviation. Errors are quoted at 1σ. See Sect. 6.3 and 6.4 for the definition of the X-ray luminosities. The contribute of unresolved HMXBs was subtracted from $L_{\rm X,diff}$ in both $0.5-2$ and $0.5-8$ keV bands.

pare our results with the derivations of Owen & Warwick (2009), we only converted the X-ray luminosities from 0.3–1.0 to 0.5–2.0 keV band (a factor of 0.43). To be consistent with their derivation, we measured the 0.5–2 keV luminosity of unresolved emission in our sample galaxies including the contribution of both gas and unresolved HMXBs and obtained a linear relation with the SFR. The scaling factor of 7.5×10^{38} erg s^{-1}($M_\odot$ yr^{-1})$^{-1}$ is within the range of X-ray/SFR ratio presented in Owen & Warwick (2009). As it is pointed out by these authors, their upper-bound estimate corresponds to the X-ray/SFR ratio predicted by Mas-Hesse, Otí-Floranes, & Cerviño (2008) for ~ 10 Myr after an extended burst of star formation, assuming 1% efficiency in the conversion of mechanical energy into X-ray emission.

6.4 Total X-ray luminosity of star-forming galaxies

Using the results of the previous sections, we can compute the total X-ray luminosity of star-forming galaxies, whose relation with the SFR is shown in Fig.6.2. Considering only galaxies from the resolved sub-sample used to study the diffuse X-ray emission, from a least-squares fit to the data with the model $\log L_{\rm X}^{\rm tot} = \log K + \beta \log {\rm SFR}$, it results a linear relation with $\beta = 1.06 \pm 0.11$ and normalization $\log K = 39.63 \pm 0.09$. The linear scaling relation obtained by fixing the slope to unity is given by the following equation:

$$L^{\rm tot}_{0.5-8\,{\rm keV}}({\rm erg\,s^{-1}}) = 4.5 \times 10^{39}\,{\rm SFR}\,(M_\odot\,{\rm yr^{-1}}) \qquad (6.3)$$

with a dispersion $\sigma = 0.32$ dex. A linear fit to the $L_{\rm X}-$ SFR relation using only galaxies from the unresolved high-SFR samples (Sect 2, Table 2.2 and 2.3), yielded the scale factor of $L_{\rm X}/{\rm SFR} \approx 3.7 \times 10^{39}$ erg/s/(M$_\odot$/yr), consistent with eq.6.3. Considering that half of the objects from the unresolved high-SFR sample are *Chandra Deep Field* North galaxies,

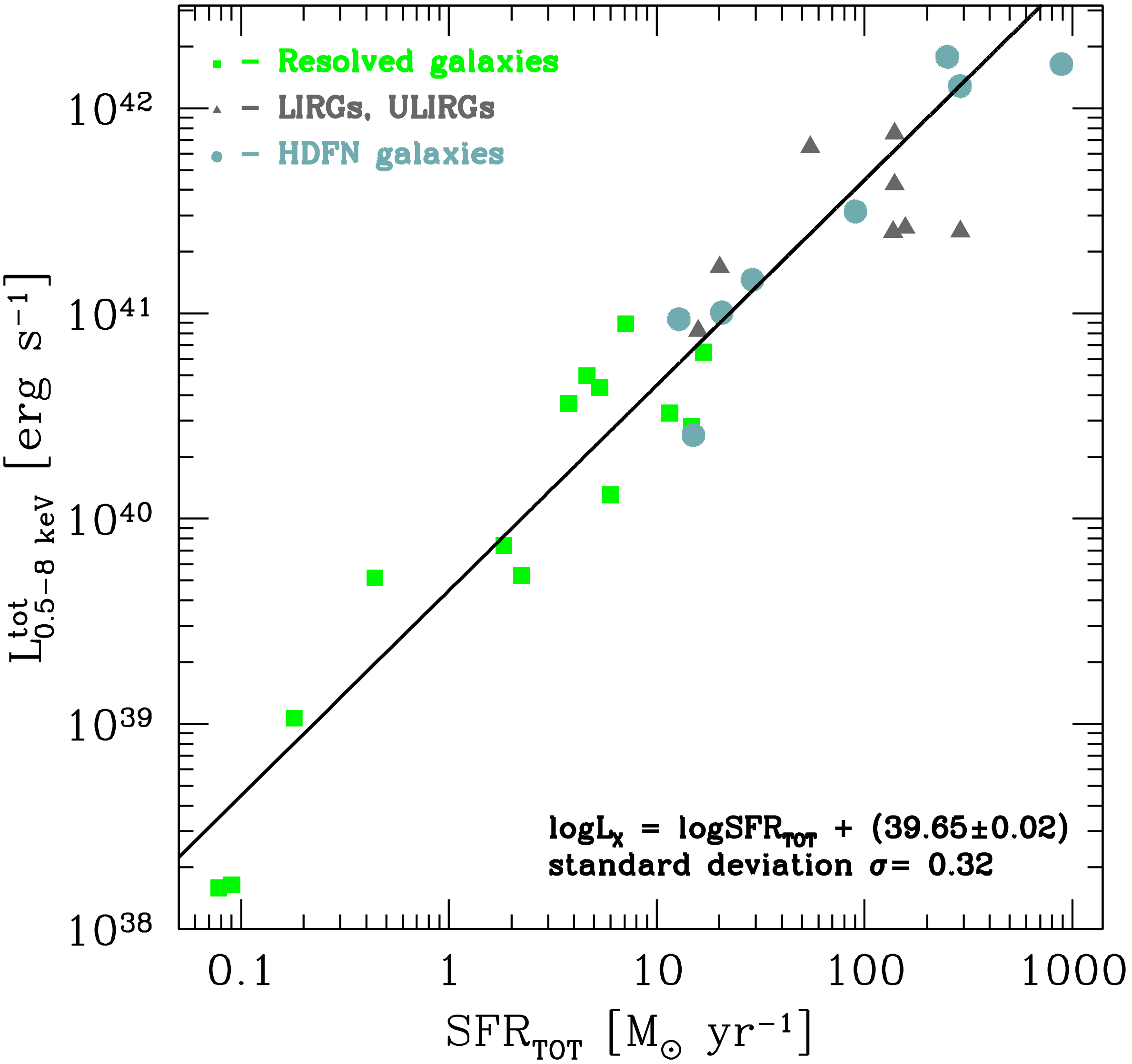

Figure 6.2: The L_X^{tot} – SFR relation. The squares are galaxies from the resolved sub-sample, for which we studied the diffuse X-ray emission, the triangles and filled circles are galaxies from the unresolved high-SFR sample, respectively unresolved luminous IR galaxies (Table 2.2) and galaxies from the *Hubble Deep Field* North and Lynx Field (Table 2.3). The solid line show the linear scaling relation, obtained using only resolved galaxies and given by eq. (6.3).

located at the red-shifts of $z \approx 0.2 - 1.3$, this makes the total X-ray luminosity of a galaxy a powerful tool to measure the star formation rate in distant galaxies.

A fit to the data from all the samples, provides $L^{\rm tot}_{0.5-8\,{\rm keV}}({\rm erg\,s^{-1}}) = 4.1{\times}10^{39}\,{\rm SFR}\,(M_{\odot}\,{\rm yr^{-1}})$, $\sigma = 0.31$. This appear to be fully in agreement with eq. (6.3), if we consider that there is a significant scatter in both the relations, therefore due to the number of galaxies investigated, the scale factor depends on the particular selection of the sub-sample.

We note that, by comparing eqs. (6.1) and (6.3): the emission from hot diffuse gas per unit of SFR, provides $\sim 17\%$ of the value total X-ray luminosity generated per unit of SFR.

We also studied the $L^{\rm tot}_{\rm X} - L_{\rm IR}$ relation. The linear fit of this relation gives the following result:

$$L^{\rm tot}_{0.5-8\,{\rm keV}}({\rm erg\,s^{-1}}) = 2.6 \times 10^{-4}\,L_{\rm IR}\,({\rm erg\,s^{-1}}) \tag{6.4}$$

where $L_{\rm IR}$ is the total $(8-1000\,\mu{\rm m})$ infrared luminosity. The dispersion around the best-fit is $\sigma = 0.4$ dex, i.e. worse than for eq.(6.3).

Chapter 7

Conclusions

In this dissertation we studied the properties of populations of high-mass X-ray binaries (HMXBs) and hot inter-stellar medium in star-forming galaxies and their relation with the star formation rate (SFR), based on the data from *Chandra*, Spitzer, GALEX and 2MASS public archives. We constructed a large sample of galaxies for which we collected homogeneous sets of multiwavelength measurements in X-ray, ultraviolet (UV), far-infrared (FIR) and near-infrared (NIR) bands. The sample include 45 star-forming galaxies in total, divided in two sub-samples: the *primary sample*, consisting of 29 nearby galaxies, having distance < 40 Mpc, so that *Chandra* can resolve their X-ray point-like source population; the *high-SFR sample*, including 16 more distant galaxies that allowed us to extend the dynamical range of SFRs by $\sim$ two orders of magnitude.

We have detected 1057 compact X-ray sources, of which ~ 300 are expected to be background active galactic nuclei (AGN). The majority of remaining ~ 700 sources are young systems associated with star-formation in the host galaxy. Based on their high X-ray luminosities and analogy with the X-ray populations in the Milky Way and few other very nearby galaxies, we conclude that they are high-mass X-ray binaries, powered by accretion of matter from a massive donor star into a compact object - a black hole or a neutron star.

In constructing and analyzing the X-ray luminosity function (XLF) of high-mass X-ray binaries, we took a special care to minimize the contamination by LMXBs, background AGN and to control the incompleteness of the *Chandra* source lists. The shape of the HMXB luminosity function is similar in different galaxies with the power law indexes having $rms = 0.25$ with respect to the average value of ≈ 1.6. The XLF normalizations, on the contrary, show significantly larger dispersion with the $rms = 0.34$ dex around the $A \propto \mathrm{SFR}$ law. Combining the data of all galaxies we produced the average XLF. Despite its by far better statistical accuracy the obtained XLF is entirely consistent with the one produced by Grimm, Gilfanov, & Sunyaev (2003) based on a much smaller sample of galaxies and much fewer sources. The HMXB XLF has a broad luminosity range $\log L_{\mathrm{X}} \sim 35 - 40$, the slope of a single slope power law and shows a moderately significant evidence for the high luminosity break or cut-off at $\log L_{\mathrm{X}} \approx 40$. Similar to Grimm, Gilfanov, & Sunyaev (2003), we did not find any statistically significant features at the Eddington luminosity limits of neutron stars or a $10\,M_\odot$ black hole.

High-mass X-ray binaries are a good tracer of the recent star formation activity in the host galaxy. Their collective luminosity is proportional to the SFR:

$$L^{\rm XRB}_{0.5-8\,\rm keV}({\rm erg\,s^{-1}}) = 2.5\times10^{39}\,{\rm SFR}\,(M_\odot\,{\rm yr^{-1}}) \tag{7.1}$$

The *rms* of points around this relation is 0.4 dex. The observed dispersion is unlikely to be caused by any of the obvious contaminating factors such as CXB or LMXB sources and is likely to have a physical origin. The collective luminosity of X-ray binaries is well correlated with the infrared luminosity of the host galaxy:

$$L^{\rm XRB}_{0.5-8\,\rm keV}({\rm erg\,s^{-1}}) = 1.75\times10^{-4}\,L_{\rm IR}\,({\rm erg\,s^{-1}}) \tag{7.2}$$

where $L_{\rm IR}$ is the total $(8-1000\,\mu{\rm m})$ infrared luminosity. The dispersion around the best-fitting relation is $\sigma = 0.5$ dex. The number of bright HMXBs scales with the SFR of the host galaxy:

$$N_{\rm XRB}(>10^{38}{\rm erg\,s^{-1}}) = 3.1\times{\rm SFR}\,(M_\odot\,{\rm yr^{-1}}) \tag{7.3}$$

with the dispersion of $rms = 0.34$ dex.

With the knowledge of the relation between the number of high-mass X-ray binaries and star formation rate of the host galaxy, we estimated that the fraction of compact objects that went through an X-ray active phase at least once in their lifetime, powered by accretion of matter from a massive donor star in a binary system is $f_X \sim 0.2$. This constrains the mass distribution of the secondary in massive binaries. For an independent mass distribution of the secondary, the power law index must be flatter than 0.3. In particular, an independent mass distribution of a Kroupa or Salpeter type is strongly excluded. Assuming that the masses of components in a binary are not independent, our results are consistent with the flat mass ratio distribution. For comparison, we obtained a similar estimate for the fraction of compact objects that become X-ray sources powered by accretion from a low-mass donor star in an LMXB. Based on the scaling-laws by Gilfanov (2004), the fraction of compact objects, X-ray active in LMXBs, is small, $f_X \sim 10^{-6}$, demonstrating that LMXBs are extremely rare objects. This result is in line with the conclusions of the binary population studies (Lewin, van Paradijs, & van den Heuvel, 1997).

We studied the unresolved X-ray emission from star-forming galaxies. The X-ray luminosity of the hot ISM component in the $0.5-2$ keV band is correlated with the SFR of the host galaxy:

$$L^{\rm diff}_{0.5-2\,\rm keV}({\rm erg\,s^{-1}}) = 5.9\times10^{38}\,{\rm SFR}\,(M_\odot\,{\rm yr^{-1}}) \tag{7.4}$$

with the dispersion $\sigma = 0.36$ dex.

The total X-ray luminosity from star-forming galaxies scales linearly with the recent star-formation processes, by a linear scaling relation with the SFR of the host galaxy:

$$L^{\rm tot}_{0.5-8\,\rm keV}({\rm erg\,s^{-1}}) = 4.5\times10^{39}\,{\rm SFR}\,(M_\odot\,{\rm yr^{-1}}) \tag{7.5}$$

with a dispersion $\sigma = 0.32$ dex. We obtained consistent scale factors for nearby galaxies from the resolved sample and galaxies from the high-SFR sample. Among the latter (eight out of 16) are *Chandra Deep Field* North galaxies, located at the red-shifts of $z \approx 0.2 - 1.3$. This proves that the total X-ray luminosity of a galaxy is a powerful tool to measure the star formation rate in distant galaxies.

Appendix A

Catalogue of HMXB in nearby star-forming galaxies

We present a catalogue of compact X-ray sources detected within the $D25$ ellipse for galaxies from our primary sample. The full catalogue data includes 1057 sources and is currently available at the link shown in the note to the Table A.1. This table is presented in its entirety in the electronic version (http://www.mpa-garching.mpg.de/∼mineo). An abbreviated version of the table is shown here for guidance as to its form and content and includes only a small fraction of the catalogue. Table A.1 lists the following information for each compact sources: sequence number (col. 2), *Chandra* X-ray Observatory (CXO) source name (JHHMMSS.s-DDMMSS) (col. 3), right ascension and declination (J2000.0) in degrees (cols. 4 and 5), distance from the galaxy center in arcsec (col. 6), number of source counts after background subtraction and its statistical error computed as described in Sec. 3.2 (cols. 7 and 8), decimal logarithm of X-ray flux and luminosity, measured in the $0.5-8$ keV band as described in Sec. 3.2 (cols. 9 and 10), location of the source within the $D25$ (col. 11). The latter indicates whether the point source has been detected in the inner galactic region dominated by HMXB population and selected as described in Sect. 3.3 (flag 1), in the outer region dominated by CXB sources (flag 2) or in the bulge region dominated by LMXB population (flag 3).

Table A.1: List of compact sources detected within the *D*25 ellipse in all galaxies of the resolved sample.

Galaxy (1)	ID (2)	CXO name (3)	$\alpha_{\rm J2000}$ (deg) (4)	$\delta_{\rm J2000}$ (deg) (5)	d (arcsec) (6)	S (cts) (7)	σ_S (cts) (8)	$\log F_{\rm X}$ $({\rm erg\,cm^{-2}\,s^{-1}})$ (9)	$\log L_{\rm X}$ $({\rm erg\,s^{-1}})$ (10)	location flag (11)
NGC 0278	1	CXOU J005204.3+473304	13.01831	47.55115	2.5	41.7	9.6	-14.42	37.80	3
	2	CXOU J005204.3+473258	13.01823	47.54965	3.1	28.7	8.4	-14.58	37.64	3
	3	CXOU J005204.6+473305	13.01957	47.55146	5.2	50.1	10.0	-14.34	37.88	3
	4	CXOU J005203.8+473309	13.01596	47.55265	9.1	62.5	10.3	-14.20	38.02	1
	5	CXOU J005203.4+473254	13.01429	47.54855	11.4	74.9	11.0	-14.15	38.07	1
	6	CXOU J005204.4+473314	13.01835	47.55404	12.8	30.5	8.0	-14.54	37.68	1
	7	CXOU J005203.3+473312	13.01410	47.55333	13.9	25.1	7.4	-14.62	37.60	1
	8	CXOU J005205.8+473302	13.02457	47.55056	16.1	31.5	7.8	-14.54	37.68	1
	9	CXOU J005202.7+473307	13.01137	47.55217	17.1	1035.4	39.1	-13.00	39.22	1
	10	CXOU J005205.5+473249	13.02299	47.54716	17.2	11.5	6.7	-14.98	37.25	1
	11	CXOU J005202.1+473316	13.00896	47.55446	26.1	16.3	6.3	-14.79	37.43	1
	12	CXOU J005205.9+473321	13.02485	47.55610	26.2	17.9	6.5	-14.78	37.44	1
	13	CXOU J005206.0+473347	13.02540	47.56320	49.2	114.7	13.5	-13.98	38.24	1
NGC 0520	1	CXO J012435.1+034731	21.14660	3.79199	2.3	1100.1	37.2	-12.79	40.17	1
	2	CXO J012434.8+034729	21.14552	3.79162	3.6	50.6	11.6	-14.13	38.84	1
	3	CXO J012435.6+034729	21.14865	3.79150	9.7	58.1	10.0	-14.07	38.90	1
	4	CXO J012434.1+034740	21.14237	3.79447	15.4	28.0	7.3	-14.34	38.62	1
	5	CXO J012433.5+034733	21.13973	3.79259	23.0	15.0	5.7	-14.63	38.34	1
	6	CXO J012433.5+034748	21.13958	3.79681	28.3	465.8	24.5	-13.14	39.82	1
	7	CXOU J012436.5+034659	21.15243	3.78320	40.2	9.1	4.7	-14.88	38.09	1
	8	CXO J012437.6+034715	21.15702	3.78772	42.6	58.8	9.8	-14.07	38.90	1
	9	CXO J012432.7+034806	21.13660	3.80198	48.5	24.1	6.8	-14.45	38.52	1
	10	CXO J012431.9+034703	21.13308	3.78437	55.1	13.5	5.4	-14.70	38.26	1
	11	CXO J012438.7+034742	21.16147	3.79512	56.0	16.4	5.8	-14.62	38.35	1
	12	CXO J012438.4+034812	21.16015	3.80340	64.0	13.0	5.5	-14.70	38.27	2
	13	CXO J012437.8+034625	21.15756	3.77382	78.6	45.9	9.1	-14.18	38.79	1
	14	CXO J012435.5+034604	21.14791	3.76794	88.3	20.4	6.5	-14.53	38.44	2
	15	CXOU J012441.5+034607	21.17299	3.76872	128.8	12.9	5.7	-14.70	38.27	2
NGC 1313	1	CXO J031818.2-663004	49.57604	-66.50116	16.8	385.1	22.5	-12.86	38.45	1
	2	CXO J031818.8-663001	49.57878	-66.50042	18.8	304.0	20.8	-12.96	38.35	1
	3	CXO J031820.0-662910	49.58346	-66.48642	48.8	5137.4	79.6	-11.68	39.62	1
	4	CXOU J031821.2-662858	49.58867	-66.48286	63.6	15.0	5.7	-14.26	37.05	1
	5	CXO J031805.4-663014	49.52287	-66.50414	66.6	161.2	14.9	-13.22	38.08	1
	6	CXO J031806.3-663038	49.52662	-66.51073	73.2	64.2	10.4	-13.63	37.68	1
	7	CXO J031823.7-662834	49.59902	-66.47625	91.7	19.6	6.4	-14.14	37.17	1
	8	CXOU J031829.5-662841	49.62308	-66.47809	108.6	13.0	5.2	-14.32	36.99	1
	9	CXO J031830.5-663135	49.62741	-66.52659	134.0	25.6	6.6	-14.04	37.27	2
	10	CXO J031839.5-662920	49.66462	-66.48898	144.3	14.2	5.6	-14.29	37.02	2
	11	CXO J031818.8-663230	49.57863	-66.54172	157.4	85.7	11.1	-13.51	37.80	2
	12	CXO J031748.7-663043	49.45354	-66.51204	170.1	32.1	7.6	-13.91	37.39	2
	13	CXO J031757.7-663224	49.49069	-66.54032	186.8	33.1	7.6	-13.91	37.40	2
	14	CXO J031747.3-663121	49.44733	-66.52265	192.7	320.1	21.3	-12.92	38.39	2
	15	CXO J031742.5-663123	49.42745	-66.52330	219.4	132.2	14.0	-13.28	38.03	2
	16	CXOU J031735.6-663059	49.39851	-66.51654	250.4	13.1	5.4	-14.28	37.03	2

Note. This table is presented in its entirety in the electronic version (http://www.mpa-garching.mpg.de/∼mineo). An abbreviated version of the table is shown here for guidance as to its form and content. Full catalogue data includes 11 columns of information for 1057 sources. Meanings and units for all columns have been summarized in detail in Appendix A.

Acknowledgements

I am grateful to Rashid Sunyaev, I am honored of having been a member of his prestigious group at the Max Planck Institut für Astrophysik. I thank him for having always motivated me and generously supported.

I am very thankful to Marat Gilfanov, a great mentor during these four years, not only for my first steps in research. I thank him for the inspiration and motivation, for the extensive scientific and non-scientific discussions, and in general for these fantastic years of training that have been a real school of life to me.

I wish to thank my colleagues, Akos, Pavel and Zhongli for the time we shared at the institute, at conferences and in the biergartens visited together with Marat. A special thank goes to Lodo and Stefano Berta for the tons of pasta cooked together at the MPE kitchen and the waiting time usually spent in strictly non-scientific discussions, annoying the hard working people around.

Many thanks to my former advisor, Stefano Ciroi, who never stopped supporting me and to Martin Henze, for helping me in writing the Zusammenfassung in an acceptable way.

Super-thanks to the whole crew of friends here in Munich, for the company, the food, the music and the time spent in front of numerous beer mugs.

A particular regard goes to Ira, who has been always there for me.

My deepest gratitude goes to my parents, two very special persons who have been close to me every day of this Ph.D. adventure. They have never stopped believing in me, supporting me during the most difficult moments and sharing with me the joy and satisfaction of the brightest moments.

Bibliography

Bavouzet N., Dole H., Le Floc'h E., Caputi K. I., Lagache G., Kochanek C. S., 2008, A&A, 479, 83

Begelman M. C., 2002, ApJ, 568, L97

Bell E. F., 2003, ApJ, 586, 794

Bogdán Á., Gilfanov M., 2008, MNRAS, 388, 56

Bogdán Á., Gilfanov M., 2010, A&A, 512, A16

Bogdan A., Gilfanov M., 2011, arXiv, arXiv:1106.3435

Brandl B. R., et al., 2009, ApJ, 699, 1982

Brandt W. N., et al., 2001, AJ, 122, 2810

Buat V., et al., 2005, ApJ, 619, L51

Canizares C. R., et al., 2000, ApJ, 539, L41

Chevalier R. A., Clegg A. W., 1985, Natur, 317, 44

Cohen J. G., Hogg D. W., Blandford R., Cowie L. L., Hu E., Songaila A., Shopbell P., Richberg K., 2000, ApJ, 538, 29

Colbert E. J. M., Mushotzky R. F., 1999, ApJ, 519, 89

David L. P., Jones C., Forman W., 1992, ApJ, 388, 82

Desroches L.-B., Ho L. C., 2009, ApJ, 690, 267

Fabbiano G., 2006, ARA&A, 44, 323

Farrah D., Afonso J., Efstathiou A., Rowan-Robinson M., Fox M., Clements D., 2003, MNRAS, 343, 585

Farrell S. A., Webb N. A., Barret D., Godet O., Rodrigues J. M., 2009, Natur, 460, 73

Franceschini A., et al., 2003, MNRAS, 343, 1181

Garmire G. P., Bautz M. W., Ford P. G., Nousek J. A., Ricker G. R., Jr., 2003, SPIE, 4851, 28

Georgakakis A., Nandra K., Laird E. S., Aird J., Trichas M., 2008, MNRAS, 388, 1205

Giacconi R., et al., 1979, ApJ, 230, 540

Gilfanov M., Grimm H.-J., Sunyaev R., 2004, MNRAS, 347, L57

Gilfanov M., 2004, MNRAS, 349, 146

Gilfanov M., Grimm H.-J., Sunyaev R., 2004, MNRAS, 351, 136

Grimes J. P., Heckman T., Strickland D., Ptak A., 2005, ApJ, 628, 187

Grimm H.-J., Gilfanov M., Sunyaev R., 2002, A&A, 391, 923

Grimm H.-J., Gilfanov M., Sunyaev R., 2003, MNRAS, 339, 793

Helou G., Soifer B. T., Rowan-Robinson M., 1985, ApJ, 298, L7

Hirashita H., Buat V., Inoue A. K., 2003, A&A, 410, 83

Iglesias-Páramo J., Buat V., Donas J., Boselli A., Milliard B., 2004, A&A, 419, 109

Iglesias-Páramo J., et al., 2006, ApJS, 164, 38

Jacoby G. H., et al., 1992, PASP, 104, 599

Jenkins L. P., et al., 2011, ApJ, 734, 33

Kennicutt R. C., Jr., 1998, ApJ, 498, 541

Kennicutt R. C., Jr., 1998, ARA&A, 36, 189

Kim D.-W., Fabbiano G., 2004, ApJ, 611, 846

King A. R., Davies M. B., Ward M. J., Fabbiano G., Elvis M., 2001, ApJ, 552, L109

Kinney A. L., Bohlin R. C., Calzetti D., Panagia N., Wyse R. F. G., 1993, ApJS, 86, 5

Kroupa P., 2002, Sci, 295, 82

Lewin W. H. G., van Paradijs J., van den Heuvel E. P. J., 1997, xrb..book

Liu Q. Z., van Paradijs J., van den Heuvel E. P. J., 2006, A&A, 455, 1165

Mapelli M., Colpi M., Zampieri L., 2009, MNRAS, 395, L71

Mapelli M., Ripamonti E., Zampieri L., Colpi M., Bressan A., 2010, MNRAS, 408, 234

Mas-Hesse J. M., Otí-Floranes H., Cerviño M., 2008, A&A, 483, 71

Mineo S., Gilfanov M., Sunyaev R., 2011, AN, 332, 349

Mineo S., Gilfanov M., Sunyaev R., 2011, arXiv, arXiv:1105.4610

Murray S. S., et al., 2000, SPIE, 4140, 144

Nardini E., Risaliti G., Salvati M., Sani E., Watabe Y., Marconi A., Maiolino R., 2009, MNRAS, 399, 1373

Owen R. A., Warwick R. S., 2009, MNRAS, 394, 1741

Persic M., Rephaeli Y., 2007, A&A, 463, 481

Postnov K. A., 2003, AstL, 29, 372

Predehl P., et al., 2000, adnx.conf, 11

Ranalli P., Comastri A., Setti G., 2003, A&A, 399, 39

Richards E. A., Kellermann K. I., Fomalont E. B., Windhorst R. A., Partridge R. B., 1998, AJ, 116, 1039

Sanders D. B., Mazzarella J. M., Kim D.-C., Surace J. A., Soifer B. T., 2003, AJ, 126, 1607

Sazonov S., Revnivtsev M., Gilfanov M., Churazov E., Sunyaev R., 2006, A&A, 450, 117

Shtykovskiy P., Gilfanov M., 2005, MNRAS, 362, 879

Shtykovskiy P., Gilfanov M., 2005, A&A, 431, 597

Shtykovskiy P. E., Gilfanov M. R., 2007, AstL, 33, 437

Strickland D. K., Heckman T. M., Weaver K. A., Dahlem M., 2000, AJ, 120, 2965

Strickland D. K., Heckman T. M., Colbert E. J. M., Hoopes C. G., Weaver K. A., 2004, ApJS, 151, 193

Strickland D. K., Heckman T. M., Colbert E. J. M., Hoopes C. G., Weaver K. A., 2004, ApJ, 606, 829

Swartz D. A., Ghosh K. K., Tennant A. F., Wu K., 2004, ApJS, 154, 519

Tyler K., Quillen A. C., LaPage A., Rieke G. H., 2004, ApJ, 610, 213

Truemper J., 1982, AdSpR, 2, 241

Sunyaev R. A., Tinsley B. M., Meier D. L., 1978, ComAp, 7, 183

Tanaka Y., Inoue H., Holt S. S., 1994, PASJ, 46, L37

Tully R. B., 1988, Sci, 242, 310

de Vaucouleurs G., de Vaucouleurs A., Corwin H. G., Jr., Buta R. J., Paturel G., Fouque P., 1991, trcb.book,

Véron-Cetty M.-P., Véron P., 2006, A&A, 455, 773

Voss R., Gilfanov M., 2006, A&A, 447, 71

Voss R., Gilfanov M., 2007, A&A, 468, 49

Weisskopf M. C., Tananbaum H. D., Van Speybroeck L. P., O'Dell S. L., 2000, SPIE, 4012, 2

Yokogawa J., Imanishi K., Tsujimoto M., Koyama K., Nishiuchi M., 2003, PASJ, 55, 161

Yuan T.-T., Kewley L. J., Sanders D. B., 2010, ApJ, 709, 884

Zampieri L., Roberts T. P., 2009, MNRAS, 400, 677

Curriculum vitae et studiorum
Stefano Mineo

Personal Data

Name:	Stefano Mineo
Nationality:	Italian
Place of birth:	Ragusa

Education and Career Path

2007-2011	**IMPRS Ph.D. student** at Max Planck Institut für Astrophysik Garching, Germany Dissertation Title: “X-ray emission from star forming galaxies” Supervisors: Marat Gilfanov, Rashid Sunyaev
June 2007	**”Laurea” degree in Astronomy** at *University of Padova* (Italy) Title of Laurea Thesis: ”X-ray and Optical Spectroscopic Properties of a Sample of Seyfert Galaxies” Supervisors: Stefano Ciroi, Piero Rafanelli
July 1999	**High School Diploma** at *Liceo Scientifico E. Fermi*, Ragusa (Italy)

Publications

1. **S.Mineo**, M.Gilfanov, R.Sunyaev
   X-ray emission from star-forming galaxies - I. High-mass X-ray binaries
   MNRAS 2011 (submitted)
   preprint at http://adsabs.harvard.edu/abs/2011arXiv1105.4610M
2. **S.Mineo**, M.Gilfanov, R.Sunyaev
   The collective X-ray luminosity of HMXB as a SFR indicator
   Astron. Nachr. 332, 349 (2011)
3. **S.Mineo**, M.Gilfanov, R.Sunyaev
   X-ray emission from star-forming galaxies - II. The hot inter-stellar medium
   MNRAS 2011 (in preparation)

Observational experience (as part of university courses)

2003-2004	observations at 1.22m-Galileo Telescope (Asiago, Italy) Optical spectroscopy of active galaxies

Computer skills

Systems: UNIX, Linux, Mac OS X, Windows
Programming: C, Perl, Bash, Mathematica
Graphics: Supermongo, Photoshop
Office: LaTex, Open Office, MS Office
Image analysis: SAOImage DS9
Astronomical data reduction packages: CIAO, SAS, IRAF, XSpec, Sherpa

Languages

Italian	mother tongue
English	good - proof of English Language ability: IELTS test - overall level 6
French	basic/good - High school studied language
German	basic - proof of German Language ability: Göthe Institut - level A1

Schools and conferences

July 2010	**The Infrared/X-ray Connection in Galaxy Evolution** MSSL, University College - London, UK *Oral presentation*
May 2010	**XMM Workshop 2010: Ultra-Luminous X-ray sources and Middle Weight Black Holes** European Space Agency Center - Madrid, Spain *Oral presentation*
September 2009	**X-ray Astronomy 2009** Bologna, Italy *Poster presentation*
September 2009	**Astrophysics of Neutron Stars (ASTRONS)** Istanbul, Turkey *Poster presentation*
October 2008	**The 6th Chandra/CIAO Workshop** Chandra X-ray Center - Cambridge (MA), USA

Additional talks and seminars

February 2011	**MPA institute seminar**
December 2010	**Invited seminar** at SRON - Utrecht, NL
July 2010	**Invited seminar** at the University of Leicester, UK
May 2010	**MPA high-energy group seminar**
March 2010	**Talk at the MPA meeting of the Fachbeirat**

Accepted proposals and grants

2011	**Telescopio Nazionale Galileo (TNG)** *Metal abundance in spiral and ring galaxies: tests for the origin of ultraluminous Xray sources.* Co-I
2010	**Chandra Cycle 12 Research Program** Archive proposal: *X-ray populations of different ages in spiral galaxies* Co-I